

5-1-2019

## Specific Heat, Magnetic Susceptibility, and the Effect of Pressure on Structural Properties and Valence Of $\text{EuMn}_2\text{Si}_2$ , $\text{EuCo}_2\text{Si}_2$ , and $\text{Eu}_5\text{In}_2\text{Sb}_6$

Brian Edward Light  
blight@physics.unlv.edu

Follow this and additional works at: <https://digitalscholarship.unlv.edu/thesesdissertations>



Part of the [Condensed Matter Physics Commons](#)

---

### Repository Citation

Light, Brian Edward, "Specific Heat, Magnetic Susceptibility, and the Effect of Pressure on Structural Properties and Valence Of  $\text{EuMn}_2\text{Si}_2$ ,  $\text{EuCo}_2\text{Si}_2$ , and  $\text{Eu}_5\text{In}_2\text{Sb}_6$ " (2019). *UNLV Theses, Dissertations, Professional Papers, and Capstones*. 3643.

<https://digitalscholarship.unlv.edu/thesesdissertations/3643>

This Dissertation is protected by copyright and/or related rights. It has been brought to you by Digital Scholarship@UNLV with permission from the rights-holder(s). You are free to use this Dissertation in any way that is permitted by the copyright and related rights legislation that applies to your use. For other uses you need to obtain permission from the rights-holder(s) directly, unless additional rights are indicated by a Creative Commons license in the record and/or on the work itself.

This Dissertation has been accepted for inclusion in UNLV Theses, Dissertations, Professional Papers, and Capstones by an authorized administrator of Digital Scholarship@UNLV. For more information, please contact [digitalscholarship@unlv.edu](mailto:digitalscholarship@unlv.edu).

SPECIFIC HEAT, MAGNETIC SUSCEPTIBILITY, AND THE EFFECT OF  
PRESSURE ON STRUCTURAL PROPERTIES AND VALENCE

OF  $\text{EuMn}_2\text{Si}_2$ ,  $\text{EuCo}_2\text{Si}_2$ , AND  $\text{Eu}_5\text{In}_2\text{Sb}_6$

By

Brian Edward Light

Bachelor of Science – Mathematics  
University of Nevada, Las Vegas  
1999

Master of Science – Physics  
University of Nevada, Las Vegas  
2002

A dissertation submitted in partial fulfillment  
of the requirements for the

Doctor of Philosophy – Physics

Department of Physics and Astronomy  
College of Sciences  
The Graduate College

University of Nevada, Las Vegas  
May 2019



## Dissertation Approval

The Graduate College  
The University of Nevada, Las Vegas

April 12, 2019

This dissertation prepared by

Brian Edward Light

entitled

Specific Heat, Magnetic Susceptibility, and the Effect of Pressure on Structural Properties AND Valence of  $\text{EuMn}_2\text{Si}_2$ ,  $\text{EuCo}_2\text{Si}_2$ , and  $\text{Eu}_5\text{In}_2\text{Sb}_6$

is approved in partial fulfillment of the requirements for the degree of

Doctor of Philosophy – Physics  
Department of Physics and Astronomy

Andrew Cornelius, Ph.D.  
*Examination Committee Chair*

Kathryn Hausbeck Korgan, Ph.D.  
*Graduate College Dean*

Ashkan Salamat, Ph.D.  
*Examination Committee Member*

Oliver Tschauner, Ph.D.  
*Examination Committee Member*

Paul Forster, Ph.D.  
*Graduate College Faculty Representative*

## Abstract

Many intermetallic solids containing elements from the rare earth series show interesting and unusual behavior associated with 4f electrons. This behavior includes unusual magnetic order, strongly correlated electrons, intermediate valence, heavy fermions, the Kondo effect, superconductivity, and non-Fermi liquid (NFL) to name a few. When long range magnetic order is suppressed to  $T = 0$  K by the application of an external tuning parameter such as pressure, magnetic field, or chemical doping, a quantum critical point (QCP) appears in which strong quantum fluctuations give rise to many of the mentioned unusual properties.

Most of the past studies on unusual 4f materials focus on those containing Ce and Yb with less work on Eu. However, europium intermetallic compounds also show a wide range of physical and magnetic properties as well as intermediate valences between the  $\text{Eu}^{2+}$  and  $\text{Eu}^{3+}$  configurations. A europium ion can be either divalent ( $\text{Eu}^{2+}:S = 7/2, L = 0, J = 7/2$ ) or trivalent ( $\text{Eu}^{3+}:S = L = 3, J = 0$ ). Divalent europium has a larger volume and magnetic moment ( $7 \mu_B/\text{Eu}$ ), while trivalent europium has a smaller volume and no magnetic moment. This has profound consequences on both the physical and magnetic properties of europium materials, especially under pressure. This dissertation studies three europium compounds,  $\text{EuMn}_2\text{Si}_2$ ,  $\text{EuCo}_2\text{Si}_2$ , and  $\text{Eu}_5\text{In}_2\text{Sb}_6$ , in which europium exhibits mixed valence states. Samples were obtained through collaboration with Los Alamos National Laboratory. Specific heat and magnetic susceptibility measurements were performed at UNLV. High pressure powder X-ray diffraction (HPXRD) and high pressure X-ray resonant emission spectroscopy (HPRXES) were performed at Argonne National Laboratory at the High Pressure Collaborative Access Team (HPCAT).

Analysis of the data from these experiments furthers the understanding of the valence behavior of europium in these materials and gives insight to future theoretical predictions of critical behavior of mixed valence systems.

## Acknowledgements

I would like to acknowledge the aid and support of the following people:

1. My advisor Dr. Andrew Cornelius for allowing me to return after a long break from raising my children after earning a Master's degree to complete my PhD. He has been my mentor in condensed matter physics.
2. Dr. Ravhi Kumar for helping me choose a topic and mentoring me in the experimental aspects of high pressure physics.
3. Curtis Kenney-Benson and Rich Ferry for the technical advice and aid with experiments and equipment set-up at HPCAT.
4. Melanie White for all of her hard work loading diamond anvil cells and her time spent at Argonne National Laboratory. Her steady hands worked when mine did not.
5. My committee members Dr. Ashkan Salamat and Dr. Oliver Tschauner for their time taken out of their busy schedules to attend committee meetings and providing advice.
6. For my children Edward, Orion, Brianna, Maddie, Drew, and Aurora. They are the source of my energy and motivation.
7. Martha Messina, my muse, my love, and my inspiration to finish writing. It has been a long road and she is there waiting for me at the finish line.
8. All faculty/staff of the Department of Physics and Astronomy at UNLV and HiPSEC faculty/staff, graduate and undergraduate students both new and old.

## Table of Contents

<b><u>Abstract</u></b> .....	iii
<b><u>Acknowledgements</u></b> .....	v
<b><u>Table of Contents</u></b> .....	vi
<b><u>List of Figures</u></b> .....	ix
<b><u>Chapter I – Introduction and Background</u></b> .....	1
<b><u>Overview</u></b> .....	1
<b><u>Specific Heat</u></b> .....	3
<b><u>Heat capacity of phonon modes in a crystal</u></b> .....	4
<b><u>Heat capacity of electrons in a metal</u></b> .....	7
<b><u>Heat capacity of a two-state system</u></b> .....	9
<b><u>Heat capacity of a three level system</u></b> .....	10
<b><u>Total heat capacity</u></b> .....	12
<b><u>Magnetic Density and Susceptibility</u></b> .....	13
<b><u>Filled Electronic Shells: Larmor Diamagnetism</u></b> .....	15
<b><u>Partially Filled Electronic Shells: Paramagnetism and Curie's Law</u></b> .....	15
<b><u>Susceptibility of Metals: Pauli Paramagnetism</u></b> .....	18
<b><u>Magnetic Ordering</u></b> .....	18
<b><u>Thermodynamic Properties of Magnetic Ordering</u></b> .....	19
<b><u>Mean Field Theory and Susceptibility Above <math>T_c</math></u></b> .....	19

<b><u>Critical Point Phase Transition</u></b> .....	20
<b><u>Heavy Fermions and Quantum Critical Points</u></b> .....	21
<b><u>Chapter II – Experimental Details and Techniques</u></b> .....	25
<b><u>Specific Heat</u></b> .....	25
<b><u>Magnetic Measurements</u></b> .....	26
<b><u>Diamond Anvil Cell</u></b> .....	26
<b><u>Angle Dispersive Powder X-ray Diffraction</u></b> .....	28
<b><u>X-Ray Absorption and X-Ray Fluorescence</u></b> .....	31
<b><u>Resonant X-ray Emission Spectroscopy</u></b> .....	32
<b><u>Understanding RIXS Data Beyond Valence</u></b> .....	34
<b><u>Fitting RXES data to find Valence</u></b> .....	36
<b><u>Chapter III – Materials and Data</u></b> .....	40
<b><u>Crystal Growth</u></b> .....	40
<b><u>EuT<sub>2</sub>M<sub>2</sub> systems</u></b> .....	41
<b><u>Valence Changes measured by RIXS</u></b> .....	42
<b><u>EuCo<sub>2</sub>Si<sub>2</sub></u></b> .....	43
<b><u>EuMn<sub>2</sub>Si<sub>2</sub></u></b> .....	43
<b><u>Eu<sub>5</sub>In<sub>2</sub>Sb<sub>6</sub></u></b> .....	44
<b><u>High Pressure X-ray Diffraction Experiments</u></b> .....	47
<b><u>EuMn<sub>2</sub>Si<sub>2</sub> Magnetic Susceptibility and Specific Heat</u></b> .....	49



<b><u>Eu<sub>5</sub>In<sub>2</sub>Sb<sub>6</sub> Specific Heat and Magnetic Susceptibility</u></b> .....	51
<b><u>Conclusions</u></b> .....	53
<b><u>EuMn<sub>2</sub>Si<sub>2</sub> and EuCo<sub>2</sub>Si<sub>2</sub></u></b> .....	53
<b><u>Eu<sub>5</sub>In<sub>2</sub>Sb<sub>6</sub></u></b> .....	54
<b><u>Appendix</u></b> .....	56
<b><u>References</u></b> .....	113
<b><u>Curriculum Vitae</u></b> .....	119

## List of Figures

<b>Figure 1. Heat capacity of the lambda transition in <math>^4\text{He}</math></b> .....	57
<b>Figure 2. RKKY Interaction</b> .....	58
<b>Figure 3. Quantum critical point diagram</b> .....	59
<b>Figure 4. Doniach diagram</b> .....	60
<b>Figure 5. Physical Properties Measurement System (PPMS) probe chamber.</b> ....	61
<b>Figure 6. Physical Properties Measurement System (PPMS) He-3 and calorimeter puck</b> .....	62
<b>Figure 7. Physical Properties Measurement System (PPMS) magnetometry</b> .....	63
<b>Figure 8. Princeton symmetric type diamond anvil cell (DAC)</b> .....	64
<b>Figure 9. Diamond anvil cell schematic</b> .....	65
<b>Figure 10. X-ray diffraction geometry</b> .....	66
<b>Figure 11. X-Ray diffraction image</b> .....	67
<b>Figure 12. X-ray absorption spectroscopy (XAS) edges</b> .....	68
<b>Figure 13. X-ray absorption spectroscopy (XAS) edges by atomic number</b> .....	69
<b>Figure 14. Resonant X-ray emission spectroscopy (RXES) apparatus.</b> ....	71
<b>Figure 15. Direct resonant inelastic X-ray spectroscopy (RIXS)</b> .....	72
<b>Figure 16. Indirect resonant inelastic X-ray spectroscopy (RIXS)</b> .....	73
<b>Figure 17. Ambient RIXS data for <math>\text{EuCo}_2\text{Si}_2</math></b> .....	74
<b>Figure 18. RIXS data for <math>\text{EuCo}_2\text{Si}_2</math> at 10.5 GPa and ambient temperatures</b> .....	75

<b>Figure 19. Ambient RIXS data for <math>\text{EuMn}_2\text{Si}_2</math>.....</b>	<b>76</b>
<b>Figure 20. RIXS data for <math>\text{EuMn}_2\text{Si}_2</math> at 13.1GPa at ambient temperature. ....</b>	<b>77</b>
<b>Figure 21. Partial fluorescence yield (PFY) data for <math>\text{EuMn}_2\text{Si}_2</math> at multiple pressures at ambient temperature. ....</b>	<b>78</b>
<b>Figure 22. Europium valence as a function of pressure in <math>\text{EuMn}_2\text{Si}_2</math>.....</b>	<b>79</b>
<b>Figure 23. RIXS data for <math>\text{Eu}_5\text{In}_2\text{Sb}_6</math> at ambient temperatures and pressures.....</b>	<b>80</b>
<b>Figure 24. fit of RXES data for <math>\text{Eu}_5\text{In}_2\text{Sb}_6</math> at ambient temperatures and pressures.</b>	<b>81</b>
<b>Figure 25. RIXS data for <math>\text{Eu}_5\text{In}_2\text{Sb}_6</math> at ambient temperatures and pressures showing three possible peaks. ....</b>	<b>82</b>
<b>Figure 26. RIXS data for <math>\text{Eu}_5\text{In}_2\text{Sb}_6</math> at ambient temperatures and 5.86 GPa. ....</b>	<b>83</b>
<b>Figure 27. fit of RXES data for <math>\text{Eu}_5\text{In}_2\text{Sb}_6</math> at ambient temperatures and 5.86 GPa.</b>	<b>84</b>
<b>Figure 28. RIXS data for <math>\text{Eu}_5\text{In}_2\text{Sb}_6</math> at ambient temperatures and 9.5 GPa. ....</b>	<b>85</b>
<b>Figure 29. RIXS data for <math>\text{Eu}_5\text{In}_2\text{Sb}_6</math> at ambient temperatures and 16 GPa. ....</b>	<b>86</b>
<b>Figure 30. fit of RIXS data for <math>\text{Eu}_5\text{In}_2\text{Sb}_6</math> at ambient temperatures and 16 GPa. ....</b>	<b>87</b>
<b>Figure 31. RIXS data for <math>\text{Eu}_5\text{In}_2\text{Sb}_6</math> at ambient temperatures and 35 GPa. ....</b>	<b>88</b>
<b>Figure 32. RIXS data for <math>\text{Eu}_5\text{In}_2\text{Sb}_6</math> at 15.25 K and 1.0 GPa. ....</b>	<b>89</b>
<b>Figure 33. RIXS data for <math>\text{Eu}_5\text{In}_2\text{Sb}_6</math> at 15.25 K and 19 GPa. ....</b>	<b>90</b>
<b>Figure 34. Partial fluorescence yield (PFY) data for <math>\text{Eu}_5\text{In}_2\text{Sb}_6</math> at multiple pressures at ambient temperature. ....</b>	<b>91</b>
<b>Figure 35. <math>\text{Eu}_5\text{In}_2\text{Sb}_6</math> valence versus pressure. ....</b>	<b>92</b>

<b>Figure 36. <math>\text{EuMn}_2\text{Si}_2</math> crystal structure .....</b>	<b>93</b>
<b>Figure 37. High pressure X-ray diffraction for <math>\text{EuMn}_2\text{Si}_2</math> at ambient temperature.</b>	<b>94</b>
<b>Figure 38. High pressure X-ray diffraction for <math>\text{EuMn}_2\text{Si}_2</math> at 7 Kelvin.....</b>	<b>95</b>
<b>Figure 39. High pressure X-ray diffraction for <math>\text{EuCo}_2\text{Si}_2</math> at ambient temperature. .</b>	<b>96</b>
<b>Figure 40. Equation of state for <math>\text{EuCo}_2\text{Si}_2</math>.....</b>	<b>97</b>
<b>Figure 41. Equations of state for <math>\text{EuMn}_2\text{Si}_2</math> at ambient temperature and 7K.....</b>	<b>98</b>
<b>Figure 42. <math>\text{Eu}_5\text{In}_2\text{Sb}_6</math> crystal structure .....</b>	<b>99</b>
<b>Figure 43. High pressure XRD for <math>\text{Eu}_5\text{In}_2\text{Sb}_6</math> at ambient temperatures.....</b>	<b>100</b>
<b>Figure 44. High pressure X-ray diffraction data for <math>\text{Eu}_5\text{In}_2\text{Sb}_6</math> at 7 Kelvin. ....</b>	<b>101</b>
<b>Figure 45. Specific heat over temperature of <math>\text{EuMn}_2\text{Si}_2</math> .....</b>	<b>102</b>
<b>Figure 46. <math>\text{EuMn}_2\text{Si}_2</math> specific heat over T fitted to a polynomial approximation ....</b>	<b>103</b>
<b>Figure 47. Approximate non-lattice specific heat <math>\text{EuMn}_2\text{Si}_2</math> .....</b>	<b>104</b>
<b>Figure 48. Approximate non-lattice entropy of <math>\text{EuMn}_2\text{Si}_2</math> .....</b>	<b>105</b>
<b>Figure 49. Specific heat over temperature of <math>\text{Eu}_2\text{In}_2\text{Sb}_6</math>.....</b>	<b>106</b>
<b>Figure 50. Non-lattice specific heat over temperature of <math>\text{Eu}_2\text{In}_2\text{Sb}_6</math>.....</b>	<b>107</b>
<b>Figure 51. Non-lattice entropy of <math>\text{Eu}_5\text{In}_2\text{Sb}_6</math> .....</b>	<b>108</b>
<b>Figure 52. Fits to magnetic susceptibility of <math>\text{EuMn}_2\text{Si}_2</math>.....</b>	<b>109</b>
<b>Figure 53. Comparison of non-lattice specific heat and susceptibility <math>\text{EuMn}_2\text{Si}_2</math>. .</b>	<b>110</b>
<b>Figure 54. Magnetic susceptibility of <math>\text{Eu}_5\text{In}_2\text{Sb}_6</math>.....</b>	<b>111</b>
<b>Figure 55. Comparison of specific heat and susceptibility <math>\text{Eu}_5\text{In}_2\text{Sb}_6</math> .....</b>	<b>112</b>

## Chapter I – Introduction and Background

### Overview

Intermetallic solids containing elements from the rare earth series show interesting and unusual behavior associated with 4f electrons. This includes Kondo screening, heavy fermion behavior, and intermediate valence behavior, sometimes accompanied by competing magnetism and superconductivity. In heavy fermion materials, the strong electronic correlations lead to a Fermi liquid where the electron becomes a quasi-particle with a renormalized mass. When magnetism is suppressed to  $T = 0$  K by the application of an external tuning parameter such as pressure, magnetic field, or chemical doping, a quantum critical point (QCP) appears in which strong quantum fluctuations give rise to unusual or non-Fermi liquid temperature dependencies of the physical properties. Competing low-energy scales set by the rare earth valence fluctuations, the f to conduction electron hybridization, the crystal fields, the exchange interactions, and the spin fluctuations contribute to interesting and varied phase diagrams. For this reason, mixed valence 4f electron systems have been of great interest recently.

One of the new areas of focus has been on the rare-earth intermetallic compounds containing europium. These europium intermetallic compounds show a wide range of physical and magnetic properties as well as intermediate valences between the  $\text{Eu}^{2+}$  and  $\text{Eu}^{3+}$  configurations. A europium ion can be either divalent ( $\text{Eu}^{2+}: 4f^7$ ,  $S = 7/2$ ,  $L = 0$ ,  $J = 7/2$ ) or trivalent ( $\text{Eu}^{3+}: 4f^6$ ,  $S = L = 3$ ,  $J = 0$ ). Divalent europium has a larger volume and magnetic moment ( $7 \mu_B/\text{Eu}$ ), while trivalent europium has a smaller volume and no

magnetic moment. This has profound consequences on both the physical and magnetic properties of europium materials, especially under pressure.

This valence transition is similar to the Kondo effect, where the magnetic moment from localized f electrons is quenched due to strong electron-electron correlations (leading to the common phrase correlated-electron system).[11] For rare-earth and actinide compounds, the competition between the Kondo effect and Ruderman–Kittel–Kasuya–Yosida (RKKY) interaction induces phenomena such as heavy fermion, unconventional superconductivity, and non-Fermi liquid behavior. In many correlated-electron systems, the low temperature state is that of a Fermi liquid where the electronic correlations lead to the electrons behaving as a quasiparticle with an enhanced mass in thermodynamic measurements. Many Ce- and Yb-based heavy fermion compounds have been extensively examined. Unlike Ce or Yb, Eu has a multiple electron or hole occupancy of its 4f shell, and the magnetic Eu 2+ state has no orbital component in the usual LS coupling.

This dissertation studies three europium metallic compounds in which europium exhibits mixed valence states. These materials are  $\text{EuMn}_2\text{Si}_2$ ,  $\text{EuCo}_2\text{Si}_2$ , and  $\text{Eu}_5\text{In}_2\text{Sb}_6$ . Samples were obtained through collaboration with Los Alamos National Laboratory. Specific heat and magnetic susceptibility measurements have been performed at UNLV. High pressure powder X-ray diffraction (HPXRD) and High pressure X-ray resonant emission spectroscopy (HPRXES) have been performed at Argonne National Laboratory at the High Pressure Collaborative Access Team (HPCAT). The data and from the measurements and its analysis provide an understanding of the valence behavior of

europium in these materials and allows for theoretical predictions of critical behavior of mixed valence systems.

This dissertation focuses on examining the Eu-based compounds to determine if the valence instabilities result in interesting electronic and magnetic states that have been seen in other heavy fermion compounds. In order to fully understand the mixed valence europium compounds studied here and to be able to make predictions about other mixed valence systems, a complete thermodynamic model of the magnetic and valence transitions must be established. We need to know how the valence changes with temperature as well as the energy associated with the change and how the magnetic properties are affected. Presented here is the necessary background in order to model the system and understand the data collected. Specific heat and magnetic susceptibility can be measured directly. Valence can be inferred from resonant HPRXES. The equation of state can be determined using HPXRD. These measurements together are used to form a coherent understanding that will allow us to determine possible critical behavior under certain conditions.

### **Specific Heat**

Specific heat measurements are a pivotal experimental technique for characterizing the fundamental excitations involved in a phase transition. Phase transitions involving spin, charge, phonons, orbital degrees of freedom, the interplay between ferromagnetism and superconductivity, Schottky-like anomalies in doped compounds, electronic levels in correlated systems, among other features, can be captured by means of high-resolution calorimetry. The entropy change associated with

temperature, including large changes due to a phase transition, no matter its nature, can be directly obtained upon integrating the specific heat over temperature, i.e.  $C(T)/T$  as a function of temperature.

### **Heat capacity of phonon modes in a crystal**

The Debye model is a method developed in 1912 by Peter Debye for estimating the phonon contribution to the heat capacity of a solid. Consider the regular lattice of atoms in a uniform solid material. Atoms in this solid oscillate about their equilibrium positions. Since they are bound together, they usually do not vibrate independently. The vibrations take the form of collective modes, which propagate through the crystal. The propagation speed is the speed of sound in the propagation direction for the material. These vibrational energies are quantized and treated as quantum harmonic oscillators.

The evidence of the behavior of vibrational energy in periodic solids is that the collective vibrational modes can accept energy in only discrete amounts. These quanta of energy are called phonons. Similar to photons, they obey Bose-Einstein statistics. The energy of a phonon in an isotropic material can be written in terms of the vibrational modes in a solid

$$E = hv = \frac{hv_s}{\lambda} = \frac{hv_s n}{2L}, \quad \text{Equation 1}$$

where  $v_s$  is the speed of sound in the solid. Using Bose-Einstein statistics, the total energy of the lattice vibrations takes the form

$$U = 3 \int_0^{E_{max}} \frac{E}{e^{E/kT} - 1} dE. \quad \text{Equation 2}$$



In terms of the phonon modes

$$U = \frac{3\pi}{2} \int_0^{n_{max}} \frac{hv_s n}{2L} \frac{n^2}{e^{hv_s n/2LkT} - 1} dn. \quad \text{Equation 3}$$

The integral can be simplified into its standard form by substituting

$$x = \frac{hv_s n}{2LkT} \quad \text{Equation 4}$$

$$x_{max} = \frac{hv_s n_{max}}{2LkT} = \frac{hv_s}{2kT} \left( \frac{6N}{\pi V} \right)^{1/3} = \frac{T_D}{T}, \quad \text{Equation 5}$$

where  $T_D$  is the Debye temperature associated with the highest allowed mode of vibration.

This gives us

$$U = \frac{9NkT^4}{T_D^3} \int_0^{T_D/T} \frac{x^3}{e^x - 1} dx. \quad \text{Equation 6}$$

To find the specific heat for a constant volume,

$$C_V = \frac{\delta U}{\delta T} = 9Nk \left( \frac{T}{T_D} \right)^3 \int_0^{T_D/T} \frac{x^4 e^x}{(e^x - 1)^2} dx. \quad \text{Equation 7}$$

This expression is the Debye model and can be evaluated numerically for a given temperature.

Usually it is much easier to measure the specific heat of a material at a constant pressure.

$$C_p = \frac{\delta H}{\delta T} = \frac{\delta U}{\delta T} + p \frac{\delta V}{\delta T} \quad \text{Equation 8}$$

The change in volume with temperature is usually small in solids, however it can be measured directly or estimated by using the thermal expansion coefficient  $\alpha_V$  where

$$\alpha_V = \frac{1}{V} \frac{dV}{dT} \quad \text{Equation 9}$$

The differences usually are negligible and can be safely ignored for incompressible materials. However, if there is a significant volume collapse due to thermal changes, it may be worthwhile noting the difference. If the pressure is effectively zero for the solid in question, then there is no difference. Atmospheric pressure is effectively zero pressure for most solids as well all the materials that are studied here.

When looking at the specific heat of a real material, it is often difficult to separate the various contributions. If there is a way to theoretically calculate the specific heat from data from different measurements, then it should be possible to isolate the various contributions. Several relations have been derived which correlate the Debye temperature and elastic constants. Madelung and Einstein derived separate relations for cubic systems that can be written in the form

$$T_D = C_b \left( \frac{h}{k} \right) \left( \frac{aB}{M} \right)^{1/2} \quad \text{Equation 10}$$

where  $C_b$  is a constant,  $h$  is Planck's constant and  $k$  is Boltzmann's constant,  $a$  is the lattice parameter of the unit cell,  $B$  is the bulk modulus and  $M$  is the molecular weight of the material.

With the advent of computers, more accurate methods of calculating the Debye temperature are possible. The basic procedure is to average the contributions of the characteristic phonon modes over the Brillouin zone using symmetry arguments. [29] These methods involved some approximations, but comparison of such  $T_D$  values with

those obtained from specific heat measurements showed a satisfactory agreement in most cases. [29]

The other standard way to isolate the Debye temperature is to measure it in the low temperature limit. If  $T \ll T_D$  then equation 7 can be evaluated as

$$C_V \sim \frac{12\pi^4}{5} \left(\frac{T}{T_D}\right)^3. \quad \text{Equation 11}$$

### Heat capacity of electrons in a metal

The electronic specific heat only becomes significant at low temperatures. The Fermi energy is much greater than  $kT$  such that the overwhelming majority of the electrons cannot receive thermal energy since there are no available energy levels within  $kT$  of their energy. Because of this, ALL of the presented electronic specific heat measurements are in the low temperature limit. The small fraction of electrons that are within  $kT$  of the Fermi level does however contribute a small specific heat, which is derived here.

The internal energy  $U$  of a system within the free electron model is the sum over one-electron levels times the mean number of electrons in that level.

$$U = 2 \sum_k \varepsilon(\mathbf{k}) f(\varepsilon(\mathbf{k})), \quad \text{Equation 12}$$

where  $f(\varepsilon)$  is the Fermi function

$$f(\varepsilon) = \frac{1}{e^{(\varepsilon-\mu)/k_B T} + 1}. \quad \text{Equation 13}$$

For a large but finite system, we can approximate this by the integral

$$U = V \int d\mathbf{k} \varepsilon(\mathbf{k}) f(\varepsilon(\mathbf{k})). \quad \text{Equation 14}$$

Dividing by the volume  $V$  gives us the energy density  $u$ .

$$u = \int \frac{d\mathbf{k}}{4\pi^3} \varepsilon(\mathbf{k}) f(\varepsilon(\mathbf{k})). \quad \text{Equation 15}$$

This integral depends only on  $\mathbf{k}$  through the electronic energy  $\varepsilon$ . This gives us

$$u = \int_{-\infty}^{\infty} d\varepsilon g(\varepsilon) \varepsilon f(\varepsilon), \quad \text{Equation 16}$$

where  $g(\varepsilon)$  is the density of energy levels per volume

$$g(\varepsilon) = \frac{3n}{2\varepsilon_F} \left( \frac{\varepsilon}{\varepsilon_F} \right)^{1/2}, \quad \varepsilon > 0; 0, \varepsilon < 0. \quad \text{Equation 17}$$

The integral can be approximated using a Sommerfield expansion for small  $T$  since for the temperatures of interest the Fermi temperature is much larger than  $T$ . This give us

$$u = u_0 + \frac{\pi^2}{6} (k_B T)^2 g(\varepsilon_F), \quad \text{Equation 18}$$

and

$$C_v = \frac{\partial u}{\partial T} = \frac{\pi^2}{3} k_B^2 T g(\varepsilon_F). \quad \text{Equation 19}$$

In terms of the Fermi temperature,  $T_F$ ,

$$C_V = C_v/n = \frac{\pi^2}{2} \frac{k_B^2 T}{\varepsilon_F} = \frac{\pi^2}{2} \frac{T}{T_F} \quad \text{Equation 20}$$

Heavy fermion materials have a low-temperature specific heat whose linear term is up to 1000 times larger than the value expected. In correlated electron systems,

electron interactions are strong enough that electrons cannot be treated as independent entities but have to consider their correlated behavior. Landau–Fermi liquid theory is a theoretical model that describes interacting electrons at low temperatures. Electrons are described as quasi-particles with the same quantum numbers and charge but an effective mass that differs from a free electron. The density of energy levels per volume,  $g(\epsilon_F)$ , can be greatly enhanced leading to an effective mass much larger than an electron.

The Fermi energy is inversely related to the electrons mass.

$$\epsilon_F = \frac{\hbar k_F^2}{2m} \quad \text{Equation 20a}$$

This into equation 20 explains the large increase in the linear component of the specific heat.

### Heat capacity of a two-state system

At low enough temperatures, there are circumstances within solids where only the lowest two energy levels are involved. These two energy levels can be associated with spins, lattice instabilities, impurity states and others. Especially important are solids where each atom has two levels with different energies depending on whether the electron of the atom has spin up or down. Consider a set of  $N$  distinguishable atoms each with two energy levels. The atoms are identical but are distinguishable by their fixed location within a crystal lattice. The energy of the two levels are  $\epsilon_0$  and  $\epsilon_1$ . The partition function for an atom with two states can be written as

$$Z = e^{-\epsilon_0/k_B T} + e^{-\epsilon_1/k_B T} = e^{-\epsilon_0/k_B T} (1 + e^{-\epsilon/k_B T}) \quad \text{Equation 21}$$

where  $\varepsilon$  is the energy difference between the two levels. At thermal equilibrium, the occupation numbers in the two levels is

$$n_0 = \frac{N}{Z} e^{-\varepsilon_0/k_B T} = \frac{N}{1+e^{-\varepsilon/k_B T}} \quad \text{Equation 22}$$

$$n_1 = \frac{N}{Z} e^{-\varepsilon_1/k_B T} = \frac{N e^{-\varepsilon/k_B T}}{1+e^{-\varepsilon/k_B T}} \quad \text{Equation 23}$$

At low temperatures almost all of the particles are in the ground state while at high temperatures there is same number of particles in the two levels. The transition between these two extremes occurs roughly when  $k_B T \approx \varepsilon$  or  $T \approx \theta = \varepsilon/k_B$ , where  $\theta$  is the scale temperature. The internal energy can be expressed as

$$E = n_0 \varepsilon_0 + n_1 \varepsilon_1 = N \frac{\varepsilon_0 e^{-\varepsilon_0/k_B T} + \varepsilon_1 e^{-\varepsilon_1/k_B T}}{e^{-\varepsilon_0/k_B T} + e^{-\varepsilon_1/k_B T}} = N \varepsilon_0 + \frac{N \varepsilon e^{-\theta/T}}{1+e^{-\theta/T}} \quad \text{Equation 24}$$

The internal energy is a monotonous increasing function of temperature that starts at  $N\varepsilon_0$  and approaches  $N(\varepsilon_0 + \varepsilon/2)$  at high temperatures.

Given the internal energy of a system, calculating heat capacity is straightforward

$$C = \frac{dE}{dT} = N k_B \frac{(\theta/T)^2 e^{-\theta/T}}{(1+e^{-\theta/T})^2} \quad \text{Equation 25}$$

The heat capacity has a maximum of order  $Nk_B$  at a temperature  $T \approx 0.417 \theta$ . This behavior for a two-level system is called a Schottky anomaly.

### Heat capacity of a three level system

Consider a case where the each atom in a crystal has a localized electron that can be either in a spin up or spin down configuration. The heat capacity of such a system we

have discussed previously for a two state system. Now complicate the system such that each atom can either have this localized electron or it can be part of the valance and that the probability of this is dependent on the temperature. What is the heat capacity of such a system? The first goal is to write down the partition function for the atom. It immediately becomes clear that there are three possible configurations the atom can be in: spin up, spin down, and no spin. This is nothing more complicated than a three state system.

In a canonical ensemble, the sum over the states is the partition function ( $Z$ ) of the system.

$$Z \equiv Tr(e^{-\beta\hat{H}}) = \sum_n e^{-E_n\beta} = \sum_n e^{-E_n/k_B T}, \quad \text{Equation 26}$$

where  $\epsilon_n$  is the  $n$ th energy level or  $n$ th eigenvalue of the system's Hamiltonian. The partition function encodes all information of the physical system from which all thermodynamic observables can be calculated. For a three-level model, the partition function is given by

$$Z = e^{-\beta E_0} + e^{-\beta E_1} + e^{-\beta E_2} = e^{-\beta E_0} + e^{-\beta(E_0+\epsilon_1)} + e^{-\beta(E_0+\epsilon_2)} \quad \text{Equation 27}$$

This assumes that the energies involved are independent of the temperature, which may or may not be valid depending on the system. For solids, this is a reasonable assumption given relatively small thermal expansions.

Calculating the specific heat we use the equations

$$E = \frac{\partial}{\partial \beta} (\ln Z), \quad \text{Equation 28}$$

and

$$C = -\beta^2 \left( \frac{\partial E}{\partial \beta} \right) \quad \text{Equation 29}$$

This gives us

$$C = \beta^2 \left( \frac{\varepsilon_1^2 e^{-\beta \varepsilon_2} + \varepsilon_2^2 e^{-\beta \varepsilon_1}}{(1 + e^{-\beta \varepsilon_1} + e^{-\beta \varepsilon_2})^2} + \frac{e^{-\beta(\varepsilon_1 + \varepsilon_2)} [\varepsilon_1(\varepsilon_1 - \varepsilon_2) + \varepsilon_2(\varepsilon_2 - \varepsilon_1)]}{(1 + e^{-\beta \varepsilon_1} + e^{-\beta \varepsilon_2})^2} \right) \quad \text{Equation 30}$$

For an ensemble of  $N$  particles in terms of two characteristic temperatures  $\theta_1$  and  $\theta_2$  we have

$$C = \frac{Nk}{T^2} \left( \frac{\theta_1^2 e^{-\theta_1/T} + \theta_2^2 e^{-\theta_2/T}}{(1 + e^{-\theta_1/T} + e^{-\theta_2/T})^2} + \frac{e^{-(\theta_1 + \theta_2)/T} [\theta_1(\theta_1 - \theta_2) + \theta_2(\theta_2 - \theta_1)]}{(1 + e^{-\theta_1/T} + e^{-\theta_2/T})^2} \right) \quad \text{Equation 31}$$

### Total heat capacity

The total heat capacity for a system is the sum of the heat capacity of all its parts.

$$C_V = C_{phonon} + C_{electronic} + C_{magnetic} \quad \text{Equation 32}$$

For example, a metallic solid with a two state magnetic component, we have

$$C_V = 9Nk \left( \frac{T}{T_D} \right)^3 \int_0^{T_D/T} \frac{x^4 e^x}{(e^x - 1)^2} dx + \frac{\pi^2}{2} \frac{T}{T_f} + Nk \frac{(\theta/T)^2 e^{-\theta/T}}{(1 + e^{-\theta/T})^2} \quad \text{Equation 33}$$

This looks rather complicated, however, there are only three independent variables, the Debye temperature  $T_D$ , the Fermi temperature  $T_f$  and the scale temperature  $\theta$ . This expression can be used to fit experimental specific heat data using relatively straightforward computational techniques.



For a metal with a three state magnetic component this gets slightly more complicated in appearance, but only adds one additional independent variable. The total heat capacity for a mixed valence europium metallic compound should be

$$C_V =$$

$$9Nk \left(\frac{T}{T_D}\right)^3 \int_0^{T_D/T} \frac{x^4 e^x}{(e^x - 1)^2} dx + \frac{\pi^2 T}{2 T_f} + \frac{Nk}{T^2} \left( \frac{\theta_1^2 e^{-\theta_1/T} + \theta_2^2 e^{-\theta_2/T}}{(1 + e^{-\theta_1/T} + e^{-\theta_2/T})^2} + \frac{e^{-(\theta_1 + \theta_2)/T} [\theta_1(\theta_1 - \theta_2) + \theta_2(\theta_2 - \theta_1)]}{(1 + e^{-\theta_1/T} + e^{-\theta_2/T})^2} \right) \quad \text{Equation 34}$$

This can be used to fit the experimental specific heat data measured for the materials presented to find the Fermi temperature  $T_f$ , the Debeye temperature  $T_D$  and the two magnetic ordering temperatures  $\theta_1$  and  $\theta_2$ . A good initial guess will necessary to properly fit data. If this information is available from other measurements, then it should be possible to calculate the heat capacity.

### Magnetic Density and Susceptibility

The magnetization density  $M(H)$  of a system with volume  $V$  in a uniform magnetic field  $H$ , where  $\mathbf{M}$  is parallel to  $\mathbf{H}$  and  $E_0(H)$  is in the ground state energy in the presence of a that field is defined to be

$$M(H) \equiv -\frac{1}{V} \frac{\partial E_0}{\partial H} \quad \text{Equation 35}$$

For a system that is in thermal equilibrium at some temperature  $T$ , the magnetization density is defined to be the thermal equilibrium average of the magnetization density of each excited state  $E_n(H)$ .<sup>19</sup>

$$M(H, T) \equiv \frac{\sum_n M_n(H) e^{-E_n/kT}}{\sum_n e^{-E_n/kT}} \quad \text{Equation 36}$$

where

$$M_n(H) \equiv -\frac{1}{V} \frac{\partial E_n(H)}{\partial H} \quad \text{Equation 37}$$

In terms of the Helmholtz free energy  $F$ , defined by the statistical mechanical relation

$$e^{-F/kT} = \sum_n e^{-E_n(H)/kT} \quad \text{Equation 38}$$

The magnetization can be written as

$$M = -\frac{1}{V} \frac{\partial F}{\partial H} \quad \text{Equation 39}$$

The susceptibility is defined as

$$\chi = \frac{\partial M}{\partial H} = -\frac{1}{V} \frac{\partial^2 F}{\partial H^2} \quad \text{Equation 40}$$

In the presence of a uniform magnetic field, the Hamiltonian of an atom is modified to include the interaction with the spin and angular momentum of the electrons. The interactions are small and perturbation theory can be used to calculate the changes in energy of the atomic states. The equation below is the result and it is the basis for the theories of magnetic susceptibility of individual atoms, ions, and molecules.<sup>19</sup>

$$\Delta E_n = \mu_B \mathbf{H} \cdot \langle n | \mathbf{L} + g_0 \mathbf{S} | n \rangle + \sum_{n' \neq n} \frac{|\langle n | \mu_B \mathbf{H} \cdot (\mathbf{L} + g_0 \mathbf{S}) | n' \rangle|^2}{E_n - E_{n'}} + \frac{e^2}{8mc^2} H^2 \langle n | \sum_i (x_i^2 + y_i^2) | n \rangle$$

$$\text{Equation 41}$$

This equation can be applied to solids in which the individual ions are assumed to be only slightly deformed in the material and the susceptibility is computed by summing over the ions in a lattice.

### **Filled Electronic Shells: Larmor Diamagnetism**

In the simplest case in which all electronic shells are filled, the ion has zero spin and the orbital angular momentum is in its ground state.

$$\mathbf{J}|0\rangle = \mathbf{L}|0\rangle = \mathbf{S}|0\rangle = 0 \quad \text{Equation 42}$$

Only the third term in the equation contributes to the field induced shift. At all but extremely high temperatures, there is only negligible probability of an atom not being in its ground state. This leads to the a susceptibility known as the Larmor diamagnetic susceptibility where

$$\chi = -\frac{N}{V} \frac{\partial^2 \Delta E_0}{\partial H^2} = -\frac{e^2}{6mc^2} \frac{N}{V} \langle 0 | \sum_i r_i^2 | 0 \rangle \quad \text{Equation 43}$$

### **Partially Filled Electronic Shells: Paramagnetism and Curie's Law**

For ions or atoms with unfilled shells with negligible magnetic interactions between ions, it is more complex. Single electron levels are characterized by the orbital angular momentum  $l$ . For a given  $l$ , there are  $2l+1$  values  $l_z$  can have and two possible spin directions for each  $l_z$ . In an atom or ion, if the electrons were non-interacting, the ground state would be degenerate, however, electron-electron Coulomb interactions and spin orbit interactions lift this degeneracy for the most part.<sup>19</sup> Forgoing the complex computations or the atomic spectra measurements, the f-electron results from the rules for

filling orbitals, known as Hund's rules, are presented in table 1. This is sufficient for our purposes as this is the only important part to consider for magnetic interactions.

There are two cases to consider for the susceptibility of an insulator with partially filled shells. First let us consider  $J = 0$  in the case where the shell is one electron short of being half filled. This is the case of the  $\text{Eu}^{3+}$  ion. The ground state is not degenerate and the linear term vanishes. Unlike the case of a filled shell, the second term does not necessarily vanish and the shift in the ground state energy is given by

$$\Delta E_0 = \sum_n \frac{|\langle 0 | \mu_B \mathbf{H} \cdot (\mathbf{L} + g_0 \mathbf{S}) | n \rangle|^2}{E_0 - E_n} + \frac{e^2}{8mc^2} H^2 \langle 0 | \sum_i (x_i^2 + y_i^2) | 0 \rangle \quad \text{Equation 44}$$

With  $N/V$  ions per unit volume and noting the  $E_n > E_0$ , the susceptibility can be written as

$$\chi = -\frac{N}{V} \frac{\partial^2 E_0}{\partial H^2} = -\frac{N}{V} \left[ \frac{e^2}{6mc^2} \langle 0 | \sum_i r_i^2 | 0 \rangle - 2\mu_B^2 \sum_n \frac{|\langle 0 | \mu_B \mathbf{H} \cdot (\mathbf{L} + g_0 \mathbf{S}) | n \rangle|^2}{E_n - E_0} \right] \quad \text{Equation 45}$$

The first term is the Larmor diamagnetic susceptibility again. The second term favors alignment of the moment parallel to the field. This is the paramagnetic correction to the Larmor diamagnetic susceptibility known as Van Vleck paramagnetism. This is only valid if the ground state at thermal equilibrium is the only appreciably occupied state.

If the shell does not have  $J=0$ , then the first term is the energy shift does not vanish and will be much higher than the other two terms that they can be ignored. The ground state is  $(2J+1)$ -fold degenerate in zero field. We can write

$$\mathbf{L} + g_0 \mathbf{S} = g(JLS)\mathbf{J} \quad \text{Equation 46}$$

where

$$g(JLS) = \frac{1}{2}(g_0 + 1) - \frac{1}{2}(g_0 - 1) \frac{S(S+1) - L(L+1)}{J(J+1)} \quad \text{Equation 47}$$

If only the lowest  $2J+1$  states are thermally excited with appreciable probability, the free energy is given by

$$e^{-F/kT} = \sum_{J_z=-J}^J e^{-g(JLS)\mu_B/kT} = \frac{e^{\beta\gamma H(J+\frac{1}{2})} - e^{-\beta\gamma H(J+\frac{1}{2})}}{e^{\beta\gamma H} - e^{-\beta\gamma H}} \quad \text{Equation 48}$$

where

$$\beta = \frac{1}{kT}, \text{ and } \gamma = g(JLS)\mu_B \quad \text{Equation 49}$$

The magnetization of  $N$  such ions in a volume  $V$  is

$$M = -\frac{N}{V} \frac{\partial F}{\partial H} = \frac{N}{V} \gamma J B_J(\beta\gamma JH), \quad \text{Equation 50}$$

where the Brillouin function  $B_J(x)$  is defined as

$$B_J(x) = \frac{2J+1}{2J} \coth \frac{2J+1}{2J} x - \frac{1}{2J} \coth \frac{1}{2J} x. \quad \text{Equation 51}$$

When  $\gamma H \ll kT$ , the small  $x$  expansion for the Brillouin function is valid resulting in

$$\chi = -\frac{N}{V} \frac{(g\mu_B)^2 J(J+1)}{3 kT}. \quad \text{Equation 52}$$

This is Curie's law and characterizes paramagnetic systems. It is commonly written in the form

$$\chi = -\frac{N}{3V} \frac{\mu_B^2 \rho^2}{k_B T} \quad \text{Equation 53}$$

where

$$\rho = g(JLS)[J(J + 1)]^{1/2} \quad \text{Equation 54}$$

For  $\text{Eu}^{2+}$ , we can calculate  $\rho$  to be  $\rho = \sqrt{63} \approx 7.94$ .

### Susceptibility of Metals: Pauli Paramagnetism

Lastly, for electrons in the conduction band of a metal it can be shown that the susceptibility is independent of temperature since the only interaction is the spin of each electron.

$$\chi = \mu_B^2 g(\epsilon_F) \quad \text{Equation 55}$$

where  $g(\epsilon_F)$  is the density of states at the Fermi energy. This is known as the Pauli paramagnetic susceptibility. Similar to what happens with the linear component of the specific heat, in correlated electron systems,  $g(\epsilon_F)$  can be greatly enhanced. This leads to a larger than normal susceptibility as temperature approaches zero for heavy fermion materials.

### Magnetic Ordering

If there were no magnetic interactions, individual magnetic moments would, in the absence of external magnetic field, be thermally disordered at any temperature and the previous discussion of Pauli paramagnetism applies. Solids in which individual magnetic moments have nonvanishing average moments below some critical temperature  $T_c$ , such as those studied here, will become magnetically ordered. The critical temperature  $T_c$  above which magnetic ordering vanishes is known as the Curie temperature in ferromagnets and the Neel temperature in antiferromagnets. In ferromagnets, there is a spontaneous magnetization due to the ordering of local moments in the same direction.

In antiferromagnets, there is no spontaneous magnetization since the sum of the spin vectors is zero. This differs in what we have presented so far in which the interactions between magnetic moments have not been considered at all.

### **Thermodynamic Properties of Magnetic Ordering**

The observed magnetization below a magnetic ordering temperature  $T_c$  can usually be well described by a power law.

$$M(T) \sim (T_c - T)^{-\beta} \quad \text{Equation 56}$$

where  $\beta$  is between 0.33 and 0.37 [19].

The onset of magnetic ordering can be seen as the temperature drops to  $T_c$  from above. In the absence of any interactions, the susceptibility should vary inversely with temperature at all temperatures. This was derived as Curie's law in the previous section. In a ferromagnet, the susceptibility is observed to diverge as the temperature approaches  $T_c$  from above. This can be described the following power law:

$$\chi(T) \sim (T - T_c)^{-\gamma} \quad \text{Equation 57}$$

where  $\gamma$  is typically between 1.3 and 1.4. [19]

### **Mean Field Theory and Susceptibility Above $T_c$**

Mean field theory is usually inadequate to describe almost any magnetic system well. It is the simplest and earliest attempt at quantitative analysis of a ferromagnetic transition done by P. Weiss. It fails to predict behavior near the critical temperature. The

theory averages the field of all other ions on individual ions as  $H_{\text{eff}}$ . Skipping the details, the result of this is the modification of Currie's law to the Currie-Weiss law.

$$\chi = \frac{c}{T-T_C} \quad \text{Equation 58}$$

This is only reliably useable when significantly higher than  $T_c$ . The next best approach without resorting to computational techniques is to simply use the critical behavior term already mentioned to fit magnetic susceptibility near  $T_c$ .

$$\chi = \frac{c}{(T-T_C)^\gamma} \quad \text{Equation 59}$$

The Curie constant  $C$  is given by

$$C = \frac{\mu_B^2 N}{3k_B V} g(JLS)^2 J(J+1) = \frac{\mu_B^2 N}{3k_B V} \rho^2 \quad \text{Equation 60}$$

In S.I. units this is,

$$C = \frac{\mu_0 \mu_B^2 N}{3k_B V} \rho^2 \quad \text{Equation 61}$$

For  $\text{EuMn}_2\text{Si}_2$ , assuming all europium ions are in the 2+ state,  $C$  is calculated to be 0.9966 K A/(T m). For  $\text{Eu}_5\text{In}_2\text{Sb}_6$ , assuming all europium ions are in the 2+ state,  $C$  is calculated to be 1.9474 K A/(T m)..

### Critical Point Phase Transition

Critical point phase transitions differ from first-order transitions in that there is no difference in the specific entropy of the two phases at the transition. [27] An example is



the normal fluid–superfluid transition in liquid He. The heat capacity of liquid  $^4\text{He}$  at the super-normal transition temperature, the lambda point, is shown in figure 1. As a critical point is approached, various properties, such as the heat capacity or the compressibility, go to infinity or zero as power laws in  $t$ , where

$$t = \frac{|T_c - T|}{T} \tag{Equation 62}$$

The heat capacity or other quantity near a lambda transition can be written in terms of the critical exponent  $\alpha$ , such as

$$C \sim t^{-\alpha} \tag{Equation 63}$$

### Heavy Fermions and Quantum Critical Points

The Kondo effect is a key part in understanding the behavior of metallic systems with strongly interacting electrons. It describes a scattering mechanism of conduction electrons in a metal due to magnetic impurities. It can be used in a more general way to describe a many-bodied scattering process from impurities or ions that have isolated magnetic moments. With this more general approach, the behavior of metallic systems with strongly interacting electrons can be understood.

The dominant contribution to the electrical resistivity in metals arises from the scattering of the conduction electrons by lattice vibrations (phonons). As lattice vibrations become more pronounced and more phonon modes become accessible with increasing temperature, the electron-phonon scattering increases. This results in a monotonically increasing resistivity with temperature in most metals. However, at very low temperatures, when most lattice vibrations should be energetically inaccessible, a

resistance minimum was observed in gold by de Haas, de Boer, and van den Berg in 1934 indicating that some other scattering process must exist [31]. Many other observations of a resistance minimum in metals have been observed since. It was much later that the resistance minimum was attributed to magnetic impurities. In 1964 Kondo showed scattering processes from magnetic impurities in which the internal spin state of the impurity and scattered electron are exchanged, gives rise to a resistivity contribution behaving as  $\log(T)$  [30].

The Kondo temperature is defined by

$$T_K \approx (D - \varepsilon_F)e^{1/|J|\rho} \quad \text{Equation 68}$$

where  $D$  is the highest energy an electron can accept,  $\rho$  is the electron density of states, and  $J$  is the electron-electron interaction strength. Below this temperature, the conduction electron spins begins to effectively screen the magnetic moments.

In the simplest case where the magnetic impurity has an unpaired spin  $S=1/2$ , the moment is gradually screened out by the conduction electrons as the temperature is lowered. As  $T$  approaches zero, it behaves effectively as a non-magnetic impurity. This results in a temperature independent contribution to the resistivity as opposed to logarithmic or linear. These impurity contributions to the magnetic susceptibility, specific heat, and other thermodynamic properties, could all be expressed as universal functions of  $T/T_K$ .

The aforementioned Kondo effect was calculated only to systems with dilute non-interacting magnetic impurities. As one moves away from the dilute limit, the magnetic impurities will interact through the RKKY interaction. This interaction tends to magnetic

order is in competition with the Kondo interaction. However, there are non-dilute alloys with magnetic ‘impurities’ at each lattice site referred to as a Kondo lattice.

The RKKY (Ruderman-Kittel-Kasuya-Yosida) interaction is a coupling mechanism in which localized magnetic moments such as nuclear magnetic moments, f-electron spins, or inner shell d-electrons interact through the conduction electrons. The theory uses perturbation theory to describe how a spin of a nucleus or localized electron interacts through the hyperfine interaction with a conduction electron. This conduction electron then interacts with a different localized electron or nuclear spin in the same way creating a correlation between the two nuclear or localized electron spins. A schematic of the RKKY exchange interaction can be seen in figure 2.

In many correlated-electron rare earth and actinide compounds that have ions with magnetic moments but do not magnetically order or order only at very low temperatures, the scattering of the conduction electrons with the magnetic ions results in a strongly enhanced effective mass. The effective mass can be of the order 1000 times that of the real mass of the electrons and are known as heavy fermions or heavy electron systems. The low temperature behavior of many of these compounds can be understood in terms of a Fermi liquid of heavy quasiparticles, with induced narrow band-like states in the region of the Fermi level. Heavy fermions are quasiparticles similar to how phonons are quasiparticles and are the effective charge carriers in these metals. The Fermi liquid is qualitatively similar to a Fermi gas in that the dynamics and thermodynamics at low temperatures and excitation energies, the non interacting fermions are replaced with quasiparticles with the same spin, charge, and momentum but possess a renormalized mass.

A quantum critical point in general is a point in the phase diagram of a material in which a continuous phase transition happens at zero temperature. These phase transitions are accomplished by tuning some non-temperature parameter such as pressure, chemical doping, or magnetic field. A schematic of this can be seen in figure 3. As mentioned earlier, the RKKY interaction leads to magnetic ordering. Kondo screening is a directly competing interaction and moves the antiferromagnetic ordering Neel temperature to lower temperatures. These interactions can be tuned with pressure or chemical doping and such that the Neel temperature goes to zero resulting in a quantum critical point shown in a Doniach diagram in figure 4.

## **Chapter II – Experimental Details and Techniques**

### **Specific Heat**

Specific heat was measured using a Quantum Design Physical Properties Measurement System (PPMS). The system uses a standard relaxation technique. A sample is placed upon a small alumina stage that is suspended by gold-palladium alloy wires attaching a heater and a thermometer in thermal contact with the stage. Good thermal contact between the sample and the stage is maintained by the use of thermal grease. A heat pulse is generated in the heater and the temperature response is measured. The target temperature rise in the sample is about 2% of the baseline temperature of the sample. This puts a fundamental resolution constraint on these measurements. Smaller heat pulses can be used, however, this increases relative measurement errors from the thermometer. The response to the heat pulse is fitted to a theoretical model, which yields the heat capacity [9]. Before this measurement can be made, the sample must first be kept at a stable baseline temperature.

Temperature is controlled in two main steps. Figures 5 and 6 show diagrams of the experimental arrangement. Several heaters and an impedance tube connected to the helium bath control temperature inside the sample space. When the impedance tube is open, He-4 from the reservoir is allowed into the cooling annulus. Warming the impedance tube above the boiling point of helium forms a gas bubble inside the tube which provides for a method of closing it. Temperatures between 400 K and 4.18 K are achieved by opening the impedance tube or activating the series of heaters and waiting for the desired temperature to stabilize. Temperatures below 4.18 K can be achieved by

lowering the pressure inside the sample space with a vacuum pump. This lowers the boiling point of helium. This is called evaporative cooling and is limited by the effectiveness of the pumps. In practice this allows for a temperature inside the sample space of about 2 K to be achieved. To further lower the temperature, a He-3 probe is used inside the sample space. He-3 has a boiling point of 3.20 K. Using a turbo pump for the next stage of evaporative cooling using He-3, a temperature of about 0.35 K can be reached.

### **Magnetic Measurements**

Magnetic susceptibility measurements were performed using a Quantum Design Physical Properties Measurement System (PPMS). A small AC drive magnetic field is superimposed on a DC field, causing a time-dependent moment in the sample. The field of the time-dependent moment induces a current in the pickup coils, allowing measurement without sample motion. The detection circuitry is configured to detect only in a narrow frequency band, normally at the fundamental frequency of the AC drive field. This arrangement is illustrated in figure 7.

### **Diamond Anvil Cell**

High-pressure angle-dispersive powder X-ray diffraction measurements were performed using a diamond anvil cell (DAC). The design of the cell is a Princeton symmetric type design depicted in figure 8 [20]. A DAC generates pressure to a sample through the use of two opposing diamond anvils where the force is supplied through the tightening of a series of screws or a membrane as shown in figure 9. [21]. The small area

of the culet compared to the area of the back of the diamond enables the creation of very large pressures with modest force.

The first step when preparing this type of DAC is to adhere the diamonds to the backing plates and then aligning the diamonds to be as perfectly parallel as possible and centered on each other. Any deviation from parallel of the culet of the diamonds will result in the fracturing of the diamonds at relatively low pressures. Adjusting the mounting screws and observing interference patterns while the diamonds are touching accomplishes alignment. This must be done with care to not damage the diamonds.

A metallic gasket with a small hole drilled out is placed between the opposing anvils. This provides a sample chamber filled with sample, pressure marker and pressure transmitting fluid that supports the pressure applied by the diamonds. The gasket is prepared by first pre-indenting it by placing it between the diamonds and compressing it from a starting thickness of about 250  $\mu\text{m}$  to 20 to 50  $\mu\text{m}$ . Using a laser-drilling system to drill a hole in the center of the pre-indent, the sample chamber is created. The diameter of the sample chamber is cut to be about a third of the diameter of the culet. After the hole has been drilled in the pre-indented gasket and has been cleaned, it is positioned on one of the two diamonds mounted in the DAC and held temporarily in place using clay.

The sample must be very finely ground in a mortar and pestle before being placed into the sample chamber. The grains should be small enough such that greater than roughly 10000 grains are in the X-Ray beam. This will enable a clean powder X-ray diffraction pattern. Failure to do this results in a spotty pattern. The finely ground sample and several ruby spheres are placed into the sample chamber. A pressure transmitting

media (PTM) of some kind is introduced to the sample chamber to completely fill the hole. It is important to make sure that the sample does not contact both diamonds to ensure the most hydrostatic measurements possible. Most of the measurements in this study used a gas-loading system located at GSECARS to load the DACs with neon. [22] Silicone fluid was used for the low temperature REXS measurements.

The ruby spheres placed into the sample chamber are used to make *in-situ* pressure measurements by measuring the shift in ruby fluorescence. Previous studies have been performed to determine the relationship between the spectral shift of the emission lines and pressure and temperature [23, 24].

### **Angle Dispersive Powder X-ray Diffraction**

In 1912 W. H and W. L Bragg found that substances that had macroscopic crystallinity scattered X-rays in characteristic patterns in sharp wavelengths unlike those of liquids or amorphous materials. These peaks are now known as Bragg peaks. Diffraction occurs when light is scattered by a periodic array with long-range order, producing constructive interference at specific angles. For constructive interference to occur from scattered light, the Bragg condition

$$n\lambda = 2d \sin \theta. \qquad \text{Equation 69}$$

must be met. The integer  $n$  is the order of the reflection,  $d$  is the spacing between periodic planes of points and  $\theta$  is the angle of incidence.

Atoms in a crystal are arranged in a periodic array and can therefore diffract light with a wavelength that is of the order of the atomic spacing. The scattering of X-rays



with wavelengths between about 0.02 Å and 100 Å from atoms produces a diffraction pattern with sharp peaks in a plot of scattered intensity versus angle of incidence, which contains information about the atomic arrangement within the crystal. Amorphous materials do not have a periodic array with long-range order and do not produce a diffraction pattern with sharp peaks but rather show broad features indicative of a distribution of atomic separations.

The unit cell of a crystal is the basic repeating unit that defines the crystal structure. This unit cell has the maximum symmetry that uniquely defines the structure and may contain more than one molecule or atom of the same type. The lattice parameters describe the size of the unit cell. Crystal structures have symmetry elements that define the atomic arrangement. Crystalline materials are separated into 7 crystal different system: triclinic, monoclinic, orthorhombic, tetragonal, trigonal, hexagonal, and cubic. There are 32 possible crystallographic point groups, a set of symmetry operations such as reflections or rotations. Any crystal is part of a particular group.

The distance between parallel planes of atoms determines the positions of the diffraction peaks. The angles at which constructive interference produces peaks is given by Bragg's law

$$\lambda = 2d_{hkl}\sin\theta \qquad \text{Equation 70}$$

The vector  $\mathbf{d}_{hkl}$  is drawn from the origin of the unit cell to intersect the crystallographic plane (hkl) at a 90° angle and its magnitude is the distance between parallel planes of atoms.

The intensity of the diffraction peaks is dependent upon the scattering atom as well as the arrangement of atoms in the crystal. The amplitude of scattered light from a crystal plane is determined by where the atoms are on the crystal plane and the scattering efficiency of the electrons in each atom. The intensity for a particular crystal plane  $I_{hkl}$  is proportional to the square of the structure factor  $F_{hkl}$ .

$$I_{hkl} \propto |F_{hkl}|^2 \quad \text{Equation 71}$$

The structure factor  $F_{hkl}$  is the sum of the scattering of all of the atoms in the unit cell a particular crystal plane.

$$F_{hkl} = \sum_{j=1}^m N_j f_j e^{2\pi i(hx_j + ky_j + lz_j)} \quad \text{Equation 72}$$

Where  $x_j$ ,  $y_j$ , and  $z_j$  are the fractional coordinates of the atoms,  $f_j$  is the scattering efficiency of the atom, and  $N_j$  is the fraction of equivalent positions of the atoms on the plane.

An ideal powder diffraction sample contains sufficient randomly orientated crystals such that a continuous ring of angles is created. This condition is met when roughly greater than 10000 grains are in the X-Ray beam. X-rays are thus diffracted in a sphere around the sample. An image plate or detector is placed such that the peaks can be recorded such that the angles can be measured. The geometry of such a device can be seen in figure 10 [33]. Example image data is shown in figure 11.

Each peak in the image corresponds to a particular spacing between crystal planes. Using software tools developed to simulate a pattern of a particular unit cell by

calculating all of the spacing between crystal planes and the corresponding magnitude of the peak, a measured diffraction pattern can be used to infer the actual lattice parameters.

### **X-Ray Absorption and X-Ray Fluorescence**

Materials exposed to X-rays or gamma rays may often experience ionization of those atoms. Ionization is when one or more electrons from the atom are ejected. This requires the photon to have a higher energy than the atom's ionization energy and results in the absorption of the photon. The exact energy to ionize the various electrons inside an atom are characteristics of the atom and the electron's quantum numbers. X-rays and gamma rays can be energetic enough to eject electrons from the inner orbitals of the atom. This leaves the electronic structure of the atom unstable and electrons in higher orbitals go into the lower orbitals to fill the hole left behind. The energy released is in the form of a photon with energy equal to the energy difference of the two orbitals involved. Thus emitted radiation from a material has energy characteristic of the atoms present. The term *fluorescence* refers when absorption of radiation of a specific energy results in the emission of radiation of a usually lower energy photon due to an electron dropping to a lower energy state to fill the hole left by the ionized electron.

X-ray absorption spectroscopy (XAS) data collection requires tuning X-ray photon energy using a crystalline monochromator to selectively choose X-ray energies from a synchrotron source that contains a range of photon energies. The energies are chosen that will excite core electrons in the various elements in studied compounds. This is in the range of 0.1–100 keV. Photo-diodes before and after the X-ray beam hits a sample are used to measure the incident and non-absorbed photon count respectively.

The spectrum seen from materials has sharp edges at places where the energy to excite a core electron exist. The edges are named according to the principal quantum number of the core electron excited where  $n = 1, 2,$  and  $3$  correspond to the K-, L- and M-edges. This is illustrated in figures 12 and 13. The specific edges for europium are shown in table 2.

Near the edges, the absorption spectrum are dependent on the atomic environment. This is known as X-ray Absorption Near Edge Spectroscopy (XANES). Slightly higher than the absorption edge is the extended X-ray absorption fine structure (XAFS) from about 150 eV to 2000 eV above the absorption edge that gives information regarding the local structure around the atom. There are many details to these measurements and what information can be gained that is the source of many books and papers. Since this measurement is not used in this study, it is only mentioned due to its similarity to Resonant X-ray Emission Spectroscopy (RXES) discussed later.

### **Resonant X-ray Emission Spectroscopy**

Resonant X-ray Emission Spectroscopy (RXES) is the broader term that encompasses resonant inelastic X-ray scattering (RIXS) which is a probe of electronic excitations. A core electron is excited by an incident X-ray near the absorption threshold. The excited state decays by emitting an X-ray photon. This is a second order optical process in contrast to X-ray absorption spectroscopy (XAS) and therefore the signals are much weaker. High brilliance X-ray sources, such as new synchrotron sources, and very sensitive, low noise detectors are required. In principle it is possible to measure the energy, momentum, and polarization change of the scattered photons [34]. This change

in energy, momentum, and polarization of the photon are due to the excitations of the material. This measurement can therefore give information about those excitations. It is referred to as resonant because the energy of the incident photon is tuned to that of one of the atomic X-ray transitions of the system. The resonance can greatly enhance the inelastic scattering cross-section by many orders of magnitude.[34] If the initial and final state are not the same, the process is called resonant inelastic x-ray scattering (RIXS)

RIXS is divided into two categories depending on the electronic levels participating in the transition of X-ray emission. In the first category, the transition occurs from a valence state to a core state. This leaves no core hole left in the final state. The difference of the incident and emitted X-ray energies correspond to the energy of electronic elementary excitations. [26] The energy of the emitted X-ray would be dependent upon the valence state of the atom due to the difference in screening between different valence states. Compared with the conventional (non-resonant) inelastic X-ray scattering, RIXS has larger intensity and depends on each intermediate state, which is convenient to identify the character of electronic excitations. The second category of RIXS is when decay happens from one core state to another core state such that a core hole is left. Absorption occurs from a core electron with energy  $E_c$  to a valence state with energy  $E_w$ . Radiative decay occurs from the transition from a core level with energy  $E_c$  from a core level with energy  $E_c$ .

$$0 \xrightarrow{XAS} E_w - E_c \xrightarrow{XES} E_w - E_c'$$

The resulting emitted photons are highly dependent on the local conditions of the atom or ion. This provides a very clear way to measure the valence of an ion. There is

certainly a wealth of information that can be gained from performing these measurements about the local conditions, however the primary purpose for this work is to distinguish between the different valence states of europium ions in metallic compounds.

The experimental arrangement used here is shown in figure 14. A diamond anvil cell is placed on top of a micro-controlled stage that is used to control its position to an accuracy of  $1\mu\text{m}$  in all three spatial directions. X-rays from the synchrotron source go through optics to select the desired incident energy photons. They pass through a diode to sample the incident count rate and are then collimated before heading to the DAC. The detector array is arranged such that it can measure the scattered photons at 90 degrees from the incident beam thus ensuring only fluorescence is measured. After the photons are scattered, it is important to attempt to count as many as possible. The count rate for our RIXS measurements, being inelastic, will be very low and therefore the measurement time can be very long, between 1 and 8 hours. The space between the DAC and the detector is filled with helium to avoid attenuation from the atmosphere. Photons that pass through the DAC are then sampled again by a diode to measure absorption.

### **Understanding RIXS Data Beyond Valence**

For direct RIXS, the incoming photon promotes a core-electron to an empty valence band state. An electron from a different state in the valence band decays and annihilates the core hole. This is shown in figure 15. For this transition to be possible, the transition from the core state to a valence state and a different valence state back to core state (hole) must be allowed. The net result is a final state with an electron-hole

excitation, since an electron was created in an empty valence band state and a hole in the filled valence band. The electron-hole excitation can propagate through the material, carrying momentum  $\hbar\mathbf{q}$  and energy  $\hbar\omega$ . Momentum and energy conservation require that  $\mathbf{q} = \mathbf{k}' - \mathbf{k}$  and  $\omega = \omega_{\mathbf{k}'} - \omega_{\mathbf{k}}$ . The momentum and energy of the incoming photon are  $\hbar\mathbf{k}$  and  $\hbar\omega$  and the momentum and energy of the outgoing photon are  $\hbar\mathbf{k}'$   $\hbar\omega'$  [34]. Although the direct transitions into the valence shell dominate the spectral line shape (which is why data appears similar to X-ray absorption), the spectral weight can be affected by interactions in the intermediate state. [34]

For indirect RIXS, the incoming photon promotes a core-electron into an empty state several electron volts above the Fermi level. Subsequently the electron from this same state decays to fill the core hole. In the intermediate state the core hole is present, which exerts a strong potential valence electrons, that tend to screen the core hole. The core-hole potential scatters these valence electrons creating electron-hole excitations in the valence band. This is shown in figure 16.

To fully understand RIXS data beyond a simple tool used to identify valence state as is done in this study, the RIXS scattering amplitude must be derived. RIXS refers to the process where the material first absorbs a photon and is then in a short-lived intermediate state, from which it relaxes by radiating a photon. RIXS intensity can be calculated starting with the Kramers-Heisenberg formula for describing the cross section for scattering from an atomic electron [34]. Even using this as a starting point, calculating the RIXS cross section is a very long derivation that uses many approximations some of which are close to being not valid for heavier atoms. Even after these approximations, ultimately, numerical methods would have to be used to calculate

what the RIXS cross section would look like for a given material. Such calculations are currently an active field of research [36]. As such research progresses, RIXS data from this study and others using RIXS to probe valence states should be further analyzed.

### **Fitting RXES data to find Valence**

RXES experiments results can be represented by 2D images of photon counts where the incident energy is on one axis and the detector angle (emitted photon energy measured after diffracting through a monochromator crystal) is the other axis. The shape of the peaks seen in these measurements is dependent upon local conditions of the atom being probed. When an electron decays and emits a photon, the energy of the photon is the energy of the atomic transition. From the uncertainty principle,

$$\Delta E \Delta T \geq \hbar \quad \text{Equation 70}$$

This defines the minimum line width possible and has a Lorentzian shape. The centered Lorentzian profile is

$$L(x, \gamma) = \frac{\gamma}{\pi(x^2 + \gamma^2)} \quad \text{Equation 71}$$

Collisional and pressure broadening also have a Lorentzian shape. Thermal motion would result in Doppler broadening that has a Gaussian line shape where

$$G(x, \sigma) = \frac{1}{\sigma\sqrt{2\pi}} e^{-x^2/2\sigma^2} \quad \text{Equation 72}$$

The Voigt profile is the convolution of these two functions where

$$V(x; \sigma, \gamma) = \int_{-\infty}^{\infty} G(x', \sigma) L(x - x', \gamma) dx' \quad \text{Equation 73}$$



In RIXS measurements, incident photons are tuned to just below the lowest possible absorption energy of a particular core electron (the energy between the core electron energy and the lowest valence band), then tuned to past the ionization energy. The *absorption threshold* is determined by the transition to the lowest unoccupied states. The absorption spectrum while rising is therefore like the rising states of the Fermi energy in an arc-tangent shape in metals. This can be closely approximated by a sigmoidal function.

$$S(x, c) = \frac{1}{1+e^{-cx}} \quad \text{Equation 74}$$

The emitted photon will have this absorption distribution as part of its spectral intensity since emission requires incident absorption in RIXS. When the incident photon is past the ionization energy, a valence electron decays emitting a photon with a mostly Lorentzian distribution. This combined with the width of the valence and the peak positions  $\mu_x$ , and  $\mu_y$  gives us a peak shape of

$$P_1(x, y) = \frac{A}{\pi} \frac{\frac{1}{2}\Gamma}{(x-\mu_x)^2 + (\frac{1}{2}\Gamma)^2} \frac{1}{1+e^{-c(y-\mu_y)}} \quad \text{Equation 75}$$

When the incident energy is very close to the edge, the resonance can greatly enhance the inelastic scattering cross-section, sometimes by many orders of magnitude.

[34] The first assumption is to assume this resonant peak would have a Gaussian or Lorentzian distribution in both the incident energy axis and the emitted energy axis. However, upon examining the data, there appears to be a correlation in the incident energy and the resonant emitted energy. In other words, how much the energy of the incident photon is above the ionization energy influences which electron in the valence

band decays to fill the hole. This results in an apparent slant to the peak and was not assumed in the theory. If the signals were purely Gaussian in nature then a 2D Gaussian would be the ideal function to describe this scenario given by

$$G_2(x - \mu_x, y - \mu_y, \sigma_x, \sigma_y, \rho) = \frac{1}{2\pi\sigma_x\sigma_y\sqrt{1-\rho^2}} e^{-\frac{1}{2(1-\rho^2)}\left(\frac{(x-\mu_x)^2}{\sigma_x^2} + \frac{(y-\mu_y)^2}{\sigma_y^2} - \frac{2\rho(x-\mu_x)(y-\mu_y)}{\sigma_x\sigma_y}\right)}$$

**Equation 76**

This adds the term  $\rho$  in equation 76. If  $\rho = 0$ , there is no correlation between the incident energy and the emitted energy to is maximum as  $\rho$  approaches 1.

Unfortunately, the peak shapes are far more Lorentzian. A convolution of these functions would be needed to accurately describe the peak shape in one dimension. In two dimensions this is complicated. This would give the function

$$V_2(x, y) = \int_{-\infty}^{\infty} \int_{-\infty}^{\infty} G_2(x', y', \sigma_x, \sigma_y, \rho) L(x - x', \gamma_x) L(y - y', \gamma_y) dx' dy'$$

**Equation 77**

The alternative, and much quicker calculation, is to just use the 2D Gaussian such that

$$P_2(x, y) = \frac{B}{2\pi\sigma_x\sigma_y\sqrt{1-\rho^2}} e^{-\frac{1}{2(1-\rho^2)}\left(\frac{(x-\mu_x)^2}{\sigma_x^2} + \frac{(y-\mu_y)^2}{\sigma_y^2} - \frac{2\rho(x-\mu_x)(y-\mu_y)}{\sigma_x\sigma_y}\right)}$$

**Equation 78**

This may result in the shapes of the fit to not quite match the actual data, but does accurately estimate  $\rho$ . The sum equations 75 and 78 were used to the fit the ambient data for  $\text{Eu}_5\text{In}_2\text{Sb}_6$  shown in figure 23. The fit residual suggests that this method is not ideal, however should sufficiently describe the peaks to obtain relative valence. Using equation

76 for  $P_2$  would likely result in more accuracy and will be a future project for programming that utilizes massively parallel computation.

In a mixed valence system, there should be a peak corresponding to each valence state. The position of these peaks can be inferred from materials with single valence states. If the different valence states occupy the same site in the crystal unit cell, the peak shape should be the same, however the position in the 2D RXES data should be different. If there are multiple sites in the crystal unit cell occupied by the same ion type, then the peak shapes could be noticeably different. A good example of data with different shaped peaks in the same data set can be seen in figure 30 discussed later. By fitting each peak and comparing the relative magnitude of each, we can find the proportion of which valence states are occupied. A numerical method to fit these peaks was written using JavaScript for this dissertation and published on a website for use. This uses the simpler equations 75 and 78. It can be found at <https://futureoutput.com/RXESfit3.html>.

## Chapter III – Materials and Data

### Crystal Growth

EuMn<sub>2</sub>Si<sub>2</sub> and EuCo<sub>2</sub>Si<sub>2</sub> polycrystalline samples were prepared by induction melting the appropriate ratio of starting elements in a graphite crucible and inert argon atmosphere. The mixture was heated up to 1100 +/- 50-degree C, temperatures determined using an optical pyrometer, and then rapidly quenched. The sample was subsequently characterized by powder X-ray diffraction (XRD), which showed a single-phase formation for the sample with the ThCr<sub>2</sub>Si<sub>2</sub> type tetragonal crystal structure (space group 139, *I4/mmm*). This structure can be seen in figure 36.

Eu<sub>5</sub>In<sub>2</sub>Sb<sub>6</sub> crystallizes in the orthorhombic (space group 55, *Pbam*) Ca<sub>5</sub>Ga<sub>2</sub>As<sub>6</sub> crystal structure and is the only known rare earth analogue to it. [35]. A single crystal was made by mixing the correct stoichiometry of europium and antimony with a large amount of indium used as flux. It is sealed in a tantalum tube with an arc-melter and placed in an induction furnace. It is heated up to 1100 to 1200 C in increments of 50 C with 5 minute intervals and then slowly cooled down again in 5 minute intervals. After cooling, the Ta tube is broken and the contents etched in acid. The crystals are hand picked from the bulk and excess indium is physically removed.

All the samples were grown in collaboration with Los Alamos National Laboratory.

## EuT<sub>2</sub>M<sub>2</sub> systems

EuT<sub>2</sub>M<sub>2</sub> systems undergo temperature-induced valence transitions that have been investigated by a variety of techniques.<sup>4</sup> EuMn<sub>2</sub>Si<sub>2</sub> and EuCo<sub>2</sub>Si<sub>2</sub> crystallize in the body-centered tetragonal ThCr<sub>2</sub>Si<sub>2</sub> structure common to many compounds in the rare earth “1-2-2 class”.

The Mn sublattice of EuMn<sub>2</sub>Si<sub>2</sub> orders antiferromagnetically at T<sub>N</sub> = 395 K.[6] At lower temperatures - 107 K, 65 K, and 32 K- spin reorientation transitions with a ferromagnetic component have been reported.[6] Neutron diffraction experiments have shown that EuMn<sub>2</sub>Si<sub>2</sub> orders in a collinear antiferromagnetic arrangement of ferromagnetic (001) Mn layers coupled antiferromagnetically along the c axis with the Mn moments directed parallel and antiparallel to the c-axis.[4] Clear evidence of a thermally driven valence transition from nearly trivalent Eu at low temperatures (T < 90 K) to an intermediate state at higher temperatures has been demonstrated by <sup>151</sup>Eu isomer shift measurements as well as neutron diffraction patterns of <sup>153</sup>EuMn<sub>2</sub>Si<sub>2</sub>. [4,6] Temperature dependent RXES measurements shown in this work mostly agrees with these findings. The temperature-induced valence transition has been reported to inhibit the magnetic transition, causing EuMn<sub>2</sub>Si<sub>2</sub> to have a relatively low value for its antiferromagnetic ordering temperature at T<sub>N</sub> = 391 K. [4]

The divalent state can become unstable with decreasing temperatures. EuMn<sub>2</sub>Si<sub>2</sub> can change from an almost divalent state at high temperatures to a trivalent state at low temperatures, with the probability of finding it in a divalent state decreasing with temperature.

## Valence Changes measured by RIXS

The effect of pressure and temperature on the valence of the europium ion in  $\text{EuMn}_2\text{Si}_2$ ,  $\text{EuCo}_2\text{Si}_2$ , and  $\text{Eu}_5\text{In}_2\text{Sb}_6$  was inferred from fitting RIXS measurements under pressure and at different temperatures. Many partial fluorescence yield (PFY) measurements were done in between complete RIXS scans to increase the number of data points. PFY scans are much faster and can be correlated to the full RIXS scans. A complete RIXS scan is required to tell the true valence value. PFY scans are only useful to measure the change in valence. RIXS scans inside a diamond anvil cell can take between 3 and 8 hours at HPCAT (Sector 16) at the Advanced Photon Source (APS) at Argonne National Lab. PFY scans are taken at a single incident energy and therefore take a fraction of the time of the full RIXS scans.

These high-pressure resonance X-ray emission spectroscopy experiments were performed at Sector 16 ID-D of the APS. The incident X-ray beam was focused to dimensions of about  $4 \times 7 \mu\text{m}$  FWHM at the Eu  $L_3$  absorption edge (6.9769 keV) with an energy resolution of 1 eV. The emission X-rays observed is the  $L\text{-}\alpha_1$  line (5.849 keV). Spectra acquisition must be done off-axis from the incident beam during RXES measurements. For this reason, measurements were taken in a panoramic-style DAC paired with a beryllium gasket. The beryllium metal was pre-indented to approximately 50 microns, with a laser-drilled  $150 \mu\text{m}$  diameter sample chamber.  $\text{EuMn}_2\text{Si}_2$ ,  $\text{EuCo}_2\text{Si}_2$ , and  $\text{Eu}_5\text{In}_2\text{Sb}_6$  powder and ruby spheres were loaded with silicone oil as the pressure-transmitting medium. Partial fluorescence yield (PFY) spectra were collected in intervals between full RIXS scans. In PFY scans, the intensity of the emitted Eu  $L_3$  fluorescence was measured while scanning the energy of the primary beam in 0.5 eV steps. Presented

here are the data and the calculated valence changes in figures 17 – 35 for all three samples.

### **EuCo<sub>2</sub>Si<sub>2</sub>**

RIXS data shown in figures 17 and 18 show EuCo<sub>2</sub>Si<sub>2</sub> completely trivalent at ambient temperature and at both ambient pressure and 10.5 GPa. Increasing the pressure and decreasing the temperature should move the valence from 2+ to 3+. High temperature measurements could possibly show the valence shift to 2+ similar to what is seen in other europium 1-2-2 compounds. All the measurements performed here are effectively in the low temperature regime showing only trivalent europium. It is possible that the Eu<sup>3+</sup> state is stable throughout the entire range of temperatures the material is in this phase. A good indicator of a mixed valence state is if it changes with pressure or temperature but is structurally unchanged. This is not observed for EuCo<sub>2</sub>Si<sub>2</sub>. Other work has showed that divalent peaks seen in EuCo<sub>2</sub>Si<sub>2</sub> were from small clusters of europium oxide impurities. [12]

EuCo<sub>2</sub>Si<sub>2</sub> turned out to be a good reference material for this study which attempted to find ‘anomalous’ behavior, like correlated-electron effects, that will only occur when Eu moves away from its J=0 trivalent state. Since EuCo<sub>2</sub>Si<sub>2</sub> is trivalent at ambient conditions, increasing pressure at ambient temperature (which should make the system tend TOWARDS the 3+ state) should have no effect on valence as is seen.

### **EuMn<sub>2</sub>Si<sub>2</sub>**

The PFY spectra for pressures up to 25 GPa are shown Figure 21 for EuMn<sub>2</sub>Si<sub>2</sub>. The divalent (E = 6.975 keV) and trivalent (E = 6.983 keV) contributions may easily be

differentiated in the PFY spectrum as well as the RIXS scans in figures 19 and 20. The intensities of the divalent and trivalent peaks are estimated by first fitting the RIXS scans with the method describe previously and then fitting multi-peak functions to the corresponding PFY spectrum. After normalizing the values of the PFY scans to the RIXS data, the intensities of the complete PFY data set are then used to estimate the average valence of Eu at each pressure. Energy resolution of the incoming beam is 2.2 eV. The spectrometer energy resolution is 0.7 eV. The core-hole lifetime broadening from the Eu  $L_3$  edge is 3.91 eV.[10] The total broadening is 4.6 eV. [10]

The average effective europium valence obtained from PFY experiments are plotted as a function of pressure in figure 22. The trend shows increasing europium valence from +2.77 approaching +3 at 25 GPa. As this system displays intermediate valence (with a magnetic moment on the Eu site), it is ideal to look for correlated-electron behavior. The temperature induced valence shift in Europium is very similar to the pressure induced valence shift. Decreasing temperature or increasing pressure both move Europium into a trivalent state.

### **Eu<sub>5</sub>In<sub>2</sub>Sb<sub>6</sub>**

Eu<sub>5</sub>In<sub>2</sub>Sb<sub>6</sub> is more complicated than EuMn<sub>2</sub>Si<sub>2</sub> or EuCo<sub>2</sub>Si<sub>2</sub> due to the lower symmetry of the crystal structure. There are three distinct site locations for europium in its crystal structure as seen in figure 42. The fit and RXES measurement at ambient conditions are shown in figure 23 and 24. Two distinct peaks can be seen corresponding to the Eu<sup>2+</sup> and Eu<sup>3+</sup> states. The shape of the trivalent peak indicates that there may be 2 different site locations that are trivalent as demonstrated in figure 25. Fits to this data



show that the net valence is +2.63. Like  $\text{EuMn}_2\text{Si}_2$  the mixed valence state is worth investigating for correlated-electron behavior.

A series of PFY scans for  $\text{Eu}_5\text{In}_2\text{Sb}_6$  were performed similar to  $\text{EuMn}_2\text{Si}_2$  and is shown in figure 34. The PFY scans are more complicated compared to the other studied Eu systems primarily due to the different peak shapes seen at different energies associated with the different Eu sites and valences. The detector was set to the  $\text{La}_1$  line (5.845 keV), which completely misses the location of peaks seen in RXES data at higher pressures. This is a good illustration as to why full RXES scans are vastly superior to PFY scans. PFY scans should never be used to measure valence independent of a RXES measurement. In cases where there are different site locations for an element, there will almost certainly be different peak shapes associated with each site. These different peak shapes will result in different apparent measured valence for a one dimensional PFY scan heavily dependent on the set point energy of the detector. A plot of the valence versus pressure with just the RXES data is therefore shown in figure 35.

Fits to RXES measurements at 5.86 GPa and 9.5 GPa accurately show the net valence of +2.69 and +2.73 respectively shown in figures 26 - 28. This is negligible change in valence and within the error of the experiment. At 16 GPa a phase transition is observed corresponding to one seen in HPXRD measurements shown later. Three distinct peaks are visible in figure 29. The simplest explanation for this is that a europium site in this new phase has a partial valence +4 state. Fits to the data indicate a valence state occupancy of 0.23  $\text{Eu}^{2+}$ , 0.58  $\text{Eu}^{3+}$ , and 0.18  $\text{Eu}^{4+}$  giving a net valence of +2.94. A  $\text{Eu}^{4+}$  state would possess a  $J=5/2$  moment. As the pressure is increased to 35 GPa, and we fit to three peaks again, we get occupancy of 0.23  $\text{Eu}^{2+}$ , 0.67  $\text{Eu}^{3+}$ , and

0.09  $\text{Eu}^{4+}$  giving a net valence of +2.86. The divalent occupancy remains unchanged with pressure, and the  $\text{Eu}^{4+}$  state seems to be moved into the  $\text{Eu}^{3+}$  state. This effective quenching of the magnetic moment of one of the europium sites with pressure, but strangely lowering the valence is unique. This phase of the material likely has very interesting magnetic and electron transport properties that should be investigated further.

Low temperature RIXS measures at 15 K and at 1.0 GPa and 19 GPa do not see the same structure. Only the two peaks corresponding to  $\text{Eu}^{2+}$  and  $\text{Eu}^{3+}$  can be seen as seen in figures 32 and 33. Measurements at higher pressure may reveal the same structure, but it is unlikely since increasing the pressure moves the theoretical  $\text{Eu}^{4+}$  state to the  $\text{Eu}^{3+}$ . The valence at 15 K moves from +2.83 at 1.0 GPa to +2.87 at 19 GPa. This a measurable but very small change. The valence at low temperatures indicates that the divalent site may become a mixed valence site with it transitioning to  $\text{Eu}^{3+}$ . The measurable shift in valence with pressure also indicates movement toward the trivalent state, and further measurements at intermediate temperatures are warranted to fully determine this behavior.

There are ten europium atoms in the unit cell with three distinct sites, four europium in one and three in each of the other two. This is important to interpret the data. If we fit instead fit three peaks for the ambient image in figure 23 with two different but overlapping  $\text{Eu}^{3+}$  peaks instead of just two peaks, we get occupancy of 0.40  $\text{Eu}^{3+}$ , 0.30  $\text{Eu}^{3+}$  and 0.30  $\text{Eu}^{2+}$  with a net valence of 2.70. This is shown in figure 25. This matches perfectly the site location distribution. This implies that this really is not a system with mixed valence, but one in which different sites possess different valence. As pressure is increased, we do see a shift, but it is very small and still fits with this picture of a system

with different europium sites having a definite valence. The high-pressure phase is different though. We definitely see a shift in valence from  $\text{Eu}^{4+}$  to  $\text{Eu}^{3+}$  while the  $\text{Eu}^{2+}$  remains unchanged and can confidently determine that there is a mixed  $\text{Eu}^{4+}$  to  $\text{Eu}^{3+}$  valence state with a strong effect on it with pressure.

### **High Pressure X-ray Diffraction Experiments**

High-pressure XRD experiments were carried out in a symmetric-type diamond anvil cell (DAC). These experiments were in an angle dispersive geometry at Sector 16 ID-B of the Advanced Photon Source.  $\text{EuMn}_2\text{Si}_2$ ,  $\text{EuCo}_2\text{Si}_2$ , and  $\text{Eu}_5\text{In}_2\text{Sb}_6$  powder were ground for several hours in an agate mortar and pestle. The fine powder was packed in to a thin dense pellet, from which pieces were removed for sample loading. A rhenium gasket was pre-indented to approximately 50  $\mu\text{m}$  thickness, with a 135  $\mu\text{m}$  diameter sample chamber drilled using the HPCAT laser drill. [18] The samples were gas loaded with neon as a pressure transmitting medium and 2-3 ruby spheres (approximately 10  $\mu\text{m}$  in diameter) for measuring pressure using the ruby fluorescence technique. HPXRD measurements were done at ambient temperatures as well as in a cryostat. Diffraction images were collected using a MAR-345 imaging plate with an incident wavelength of  $\lambda = 0.4216 \text{ \AA}$  and integrated using the Dioptas software. [7] The sample-to-detector distance was calibrated using a  $\text{CeO}_2$  standard. The integrated diffraction patterns were further analyzed using Rietveld (RIETICA) package. [8]

Both  $\text{EuMn}_2\text{Si}_2$  and  $\text{EuCo}_2\text{Si}_2$  showed the single-phase  $\text{ThCr}_2\text{Si}_2$  type tetragonal structure with space group 139,  $I4/mmm$  throughout the experiment, as shown in figures

37-39 from the raw HPXRD waterfall plots. The pressure versus volume data for  $\text{EuCo}_2\text{Si}_2$  at ambient temperature is shown in figure 40.

The pressure versus volume for  $\text{EuMn}_2\text{Si}_2$  at both 7 K and ambient temperatures is shown in figures 41. A second-order Birch-Murnaghan equation of state (EOS) is fitted to the experimental data. We expect that the higher temperature sample should be more compressible than the low temperature sample, as going from  $\text{Eu}^{2+}$  to  $\text{Eu}^{3+}$  should result in a significant volume decrease. This is clearly evident from the data presented.

The bulk modulus and its pressure derivative are found to be  $B_0 = 72 \pm 6$  GPa and  $B_0' = 11 \pm 2$  at ambient temperature, and  $B_0 = 121 \pm 4$  GPa and  $B_0' = 4.9 \pm 0.5$  at  $T = 7$  K. There are no anomalies in the compressibility that would indicate a volume collapse associated with a first order transition.  $\text{EuMn}_2\text{Si}_2$  remains in the same phase throughout all the pressures and temperatures measured here. This indicates the transition from  $\text{Eu}^{2+}$  to  $\text{Eu}^{3+}$  appears to be continuous in nature as was also evident in the RXES measurements.

X-ray diffraction measurements show  $\text{Eu}_5\text{In}_2\text{Sb}_6$  in the rather complex orthorhombic (space group 55, Pbam)  $\text{Ca}_5\text{Ga}_2\text{As}_6$  crystal structure shown in figure 42. High pressure X-ray diffraction measurements are shown in figures 48 and 49. A structural phase transition to a yet to be determined structure is seen between 13.4 GPa and 17.1 GPa. This matches the phase transition seen in RXES data. Measurements at 7 K only were performed up to 15 GPa and no evidence of the phase transition was seen. RXES measurements showed no change up to 19 GPa at 15 K. Further low temperature measurements are required to determine where the phase boundary is.

## EuMn<sub>2</sub>Si<sub>2</sub> Magnetic Susceptibility and Specific Heat

Heat capacity measurements performed on EuMn<sub>2</sub>Si<sub>2</sub> are shown in Figure 45. Magnetic susceptibility measurements are shown in figure 52. The peak at 62 K corresponds to an antiferromagnetic transition and is seen in the magnetic susceptibility data as well. Susceptibility measurements below 62 K do not match well with those reported by Nowik.[6] This can be explained by sample variation. Below an antiferromagnetic transition, susceptibility can vary significantly depending on the local crystallite directions relative to the excitation field. Neutron diffraction experiments did not find evidence for the reorientation transitions in EuMn<sub>2</sub>Si<sub>2</sub> at 107 K, 65 K, and 32 K, reported previously.[4,6] Shown in figure 52 is a fit to the Currie-Weiss (equation 58) that gives  $T_N = 56.225 \pm 0.07$  K and a Currie constant of  $C = 4.894 \pm 0.05$  emu/mol K above about 60 K. Below what is assumed to be an antiferromagnetic transition we see what appears to be a second magnetic transition. A fit was done using the Currie-Weiss equation but does not yield any information.

Evidence for the reorientation transitions in EuMn<sub>2</sub>Si<sub>2</sub> at 107 K, 65 K, and 32 K, reported previously were not found by neutron diffraction experiments.[4,6] Susceptibility measurements shown here in Figure 36 do not match well with those reported by Nowik.[6]

Neutron diffraction has been used by Hofman *et al.* to make direct measurements of the magnetic ordering in EuMn<sub>2</sub>Si<sub>2-x</sub>Ge<sub>x</sub> at  $x = 0, 2$ . [4] They showed that the magnetic structures adopted by the Mn sublattices in the two compounds were simple commensurate antiferromagnetic structures. The magnetic order differs going from Ge to Si. for EuMn<sub>2</sub>Ge<sub>2</sub>, the Mn moments are arranged antiferromagnetically both within the

ab-plane and along the  $c$ -axis, while for  $\text{EuMn}_2\text{Si}_2$ , the Mn moments form ferromagnetic ab-sheets that are coupled antiferromagnetically along the  $c$ -axis.[4]

In  $\text{EuMn}_2\text{Ge}_2$ , the europium ion is firmly divalent and the Eu sub-lattice orders incommensurately at 9.8 K.[17] This differs greatly from  $\text{EuMn}_2\text{Si}_2$  where neutron diffraction measurements show no ordering in the europium sublattice above 1.8 K.[4] This result is expected since as europium becomes trivalent, there is no net moment to order.

Fitting equations 33 or 34 to the specific heat data fails to fit the features seen at all. This is not surprising since these would describe the heat capacity of completely non interacting spins. A Debye temperature of 366 K can be fit somewhat poorly. This is not a surprise since the Debye model assumes that the phonon energies are constant with Temperature. Given how the shift in valence with temperature significantly alters the bulk modulus, assuming that the phonon energies are constant is an extremely poor approximation and the Debye model is not valid. A polynomial fit was performed in order to attempt to isolate the specific heat of the transition near 60 K. This is shown in figure 46. The resulting non-lattice contribution is shown in figure 47. The entropy of this transition is then calculated and shown in figure 48. We see a very small amount of entropy from this transition that corresponds to about  $0.03 R \ln 8$ , implying that only 3% of europium is still divalent at this point.

Figure 53 shows the susceptibility plotted along side the non-lattice specific heat. This shows the transition seen matches the magnetic ordering. A second smaller peak in the specific heat matches with the peak of the unknown magnetic ordering. This is

perhaps a ferromagnetic ordering of canted antiferromagnetic europium. This is supported by the dependence of the susceptibility for this peak with the excitation field.

Significant differences between the magnetic susceptibility measurements between different groups suggest that this material's magnetic behavior is highly dependent on small impurities or site location disorder, especially below 65 K and/or texture in the samples. Europium is also an extremely volatile metal and there is difficulty in making samples without oxide impurities. Different techniques can result in different possible site location disorder even if the stoichiometry is exact.

### **Eu<sub>5</sub>In<sub>2</sub>Sb<sub>6</sub> Specific Heat and Magnetic Susceptibility**

The specific heat data is shown in figure 49 with a fit to the Debye model. A Debye temperature of 158 K is found. Subtracting the Debye fit from the specific heat gives us the non-lattice contribution to specific heat shown in figure 50. Two sharp lambda peaks are easily identified. It appears that there is a Shottkey like peak that is overlapping with this. The entropy for this peak is shown in figure 51. The total entropy is almost exactly  $5 R \ln 8$ . If these peaks are only from magnetic ordering, it implies all the europium is divalent, which we know is not true. These transitions require further study to determine their nature.

Magnetic susceptibility was performed on a 3.2 mg Eu<sub>5</sub>In<sub>2</sub>Sb<sub>6</sub> sample. This data is shown in figure 54. The signal from this small amount of sample was at the limit of what the Physical Properties Measurement Systems (PPMS) AC susceptibility options capabilities. To compensate for the noise, a robust amount of data was collected. The magnetic susceptibility behaves with Curie-Weiss behavior above a temperature of 14.2

K and can be fit with equation 58. The susceptibility after the transition temperature drops like a power law implying that the sample orders antiferromagnetically. A fit to the Curie-Weiss equation, shown in figure 38, gives us  $T_C = -6.49 \pm 0.09$  K indicative of AF correlations and a Curie constant of  $C = 8.05 \pm 0.03$  emu/mol Eu. This indicates an antiferromagnetic transition. Figure 55 shows the susceptibility, specific heat and DC magnetization plotted together. From this it is clear that the sharp lambda transition seen is associated with the antiferromagnetic ordering seen in the susceptibility. The second sharp transition corresponds to a maximum in the DC magnetization.

At 3.40 K we see a sharp superconducting transition begin. This is likely due to impurities of indium as this is the superconducting transition temperature of elemental indium. This sample was grown in an indium flux and even a tiny fraction pure indium as an impurity in the sample would dominate the signal with a superconducting transition. Any magnetic signal below this temperature is effectively screened by the indium impurity superconducting response.



## Conclusions

### EuMn<sub>2</sub>Si<sub>2</sub> and EuCo<sub>2</sub>Si<sub>2</sub>

EuCo<sub>2</sub>Si<sub>2</sub> was shown to not be a mixed valence system and having a stable Eu<sup>3+</sup> valence state within the pressures and temperature ranges measured here. It remains in the ThCr<sub>2</sub>Si<sub>2</sub> type tetragonal crystal structure up to highest pressures measured of 60 GPa. An equation of state fit gives us  $B_0 = 161 \pm 4$  GPa and  $B_0' = 4.0 \pm 0.3$ .

EuMn<sub>2</sub>Si<sub>2</sub> is shown to be a mixed valence system with valence dependent on both temperature and pressure. No structural phase transitions are observed up to 32 GPa at ambient temperatures and also at 7 K. Equation of state fits give us  $B = 72$  GPa and  $B' = 11$  at ambient temperature while at 7 K we get  $B = 121$  GPa and  $B' = 4.9$ . The large difference between the ambient temperature and low temperature equations of state fits can be explained by the shift in valence. At low temperatures, europium is completely in the trivalent state making the material much less compressible. At high temperatures, the europium larger divalent state is moved into the smaller trivalent state under pressure.

Specific heat measurements show a peak at about 60 K which matches a change in the paramagnetic response seen in magnetic susceptibility. The Debye model poorly fits specific heat measurements due to changes in temperature resulting in significant changes in the elastic constants because of a shift in valence from divalent to trivalent. Magnetic susceptibility measurements show a paramagnetic response above 58 K. Between 58 K and 30 K we see a different possibly paramagnetic response with a different  $T_c$  and Currie constant perhaps indicating a ferromagnetic ordering of canted antiferromagnetic ordering.

## Eu<sub>5</sub>In<sub>2</sub>Sb<sub>6</sub>

Eu<sub>5</sub>In<sub>2</sub>Sb<sub>6</sub> is shown to not be a mixed valence system in the ambient pressure phase at ambient temperature. The changes in valence due to pressure are negligible and within the error of the measurement. There are three different site locations for the ten europium atoms in the unit cell. Seven of the sites are Eu<sup>3+</sup> and three are Eu<sup>2+</sup>. The Eu<sup>2+</sup> sites antiferromagnetically order at 14.2 K with a very weak magnetic response. At 15 K there is some indication that the Eu<sup>2+</sup> site becomes an intermediate valence state. The occupancies no longer match those of the crystal structure. Pressure moves the net valence from Eu<sup>2+</sup> to Eu<sup>3+</sup> a small but measurable amount. Further valence measurements at a range of intermediate temperatures and lower temperatures than 15 K are required to determine this.

In the high-pressure phase above 16 GPa, we see what is most likely a mixed valence state between Eu<sup>4+</sup> and Eu<sup>3+</sup>. Increasing pressure moves the mixed valence state from Eu<sup>4+</sup> to Eu<sup>3+</sup>. The Eu<sup>2+</sup> site is unaffected by pressure and it assumed to not be in a mixed valence state. The decreasing of valence with pressure is not something commonly observed nor was it expected. Further study of this high-pressure phase is warranted and could possess very unique electronic and magnetic properties.

The specific heat data show a good fit to the Debye model. The series of peaks seen at low temperatures correspond to magnetic ordering seen in susceptibility measurements. Antiferromagnetic ordering is likely. The nature to the two lambda transitions is unknown. It is possible that at low temperatures, the europium valence becomes unstable. This is supported by the RXES measurements done here. Lower

temperature measurements of the valence as a function of temperature would shed some clarity on this.

### Appendix

n	$l_z = 3, 2, 1, 0, -1, -2, -3$	S	$L = \left  \sum l_z \right $	J	Symbol
1	↓	1/2	3	5/2	${}^2F_{5/2}$
2	↓ ↓	1	5	4	${}^3H_4$
3	↓ ↓ ↓	3/2	6	9/2	${}^4I_{9/2}$
4	↓ ↓ ↓ ↓	2	6	4	${}^5I_4$
5	↓ ↓ ↓ ↓ ↓	5/2	5	5/2	${}^6H_{5/2}$
6	↓ ↓ ↓ ↓ ↓ ↓	3	3	0	${}^7F_0$
7	↓ ↓ ↓ ↓ ↓ ↓ ↓	7/2	0	7/2	${}^8S_{7/2}$
8	↓↑ ↑ ↑ ↑ ↑ ↑ ↑	3	3	6	${}^7F_6$
9	↓↑ ↓↑ ↑ ↑ ↑ ↑ ↑	5/2	5	15/2	${}^6H_{15/2}$
10	↓↑ ↓↑ ↓↑ ↑ ↑ ↑ ↑	2	6	8	${}^5I_8$
11	↓↑ ↓↑ ↓↑ ↓↑ ↑ ↑ ↑	3/2	6	15/2	${}^4I_{15/2}$
12	↓↑ ↓↑ ↓↑ ↓↑ ↓↑ ↑ ↑	1	5	6	${}^3H_6$
13	↓↑ ↓↑ ↓↑ ↓↑ ↓↑ ↓↑ ↑	1/2	3	7/2	${}^2F_{7/2}$
14	↓↑ ↓↑ ↓↑ ↓↑ ↓↑ ↓↑ ↓↑	0	0	0	${}^1S_0$

**Table 1. Ground states of ions with partially filled f-shells constructed from Hund's rules.**

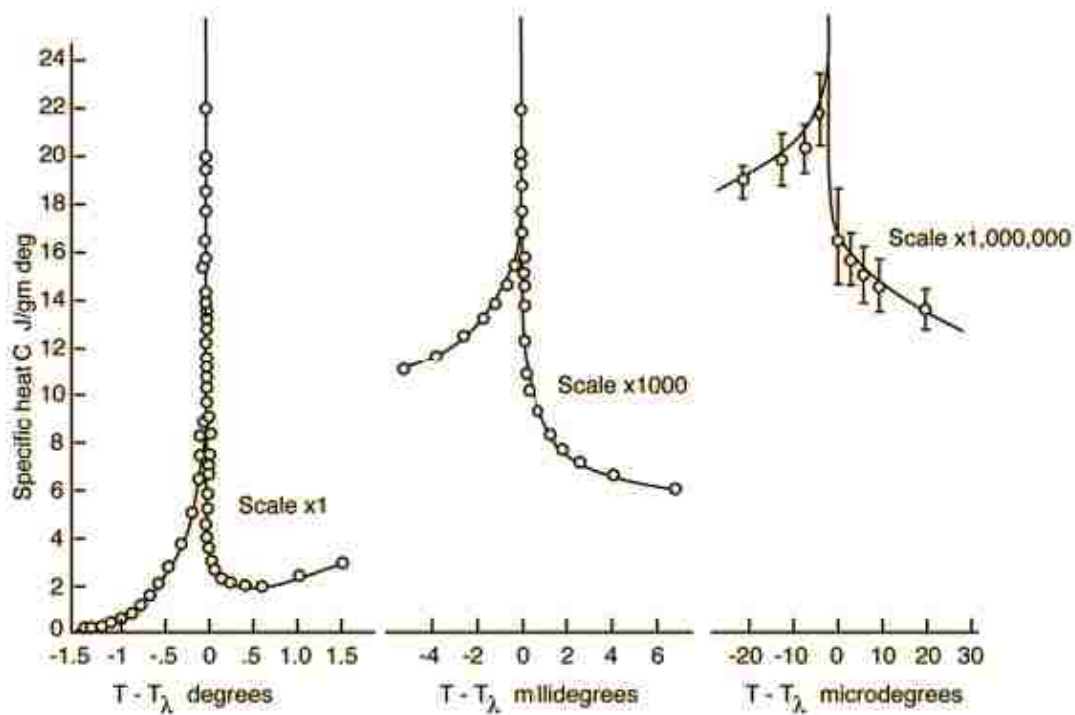


**Figure 1. Heat capacity of the lambda transition in  $^4\text{He}$ .**

This is the heat capacity of liquid  $^4\text{He}$  at the superfluid to normal transition temperature. It is called the lambda point due to the shape of the peak being similar to the greek letter  $\lambda$ . It is an example of a second order phase transition in which there is no entropy difference between the two phases at a single temperature. Image from Cochran (1966) [32].

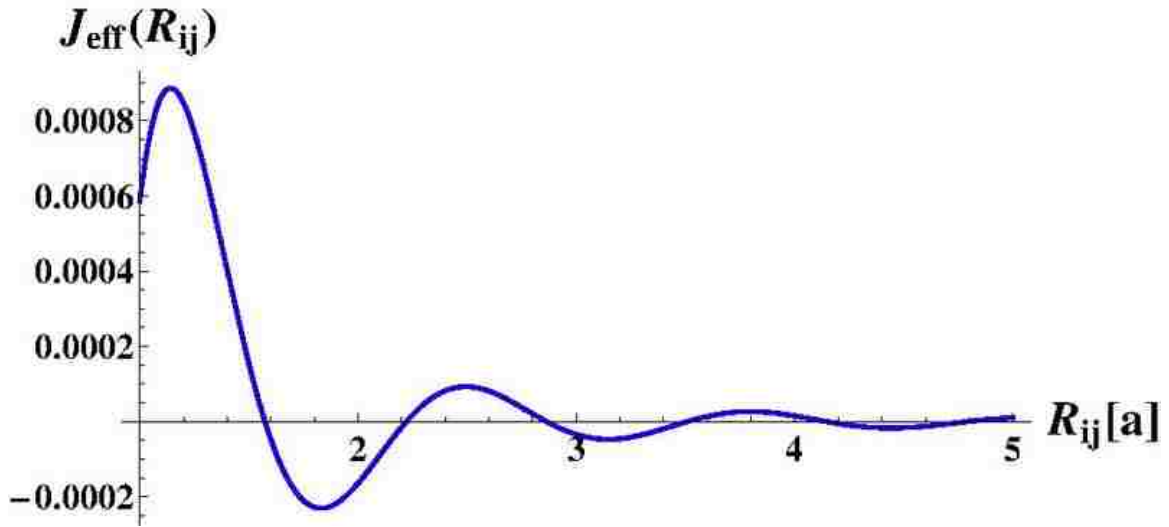


**Figure 2. RKKY Interaction**

$J_{\text{RKKY}}(r) \sim -J^2\rho (\cos 2k_{\text{F}}r)/k_{\text{F}}r$ ,  $T_{\text{RKKY}} = J^2\rho$ . In dense systems, the RKKY interaction typically gives rise to an ordered antiferromagnetic state with a Neel temperature  $T_{\text{N}}$  of the order  $J^2\rho$

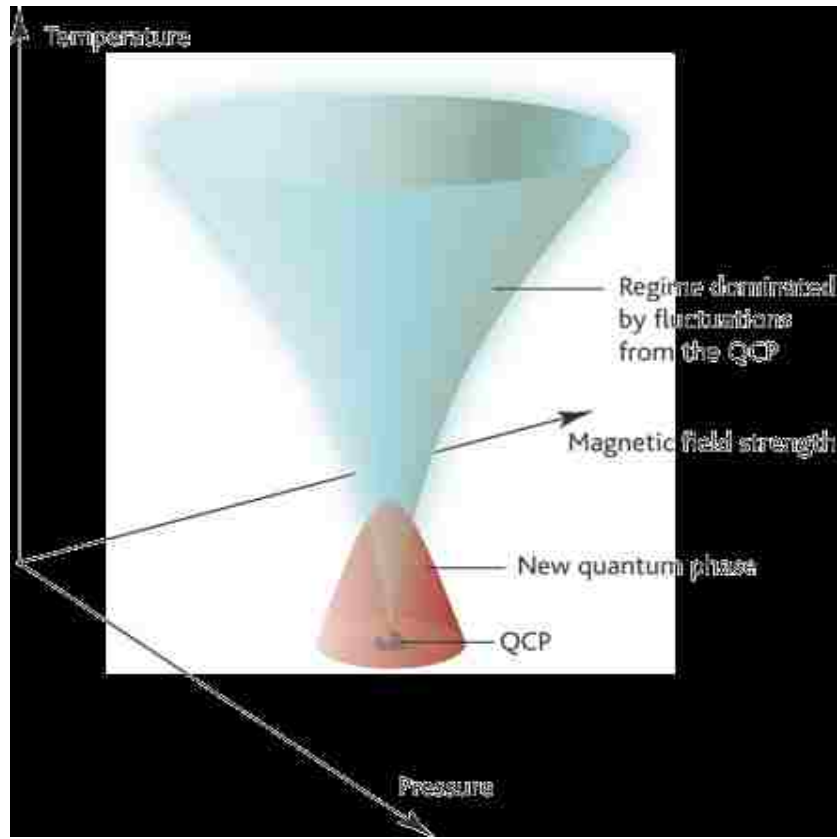


**Figure 3. Quantum critical point diagram**

This is a schematic of a generalized quantum critical phase diagram. The quantum critical point (QCP) is formed by tuning some combination of external parameters such as pressure and magnetic field. This point is where a continuous phase transition takes place at zero temperature. New phases are often found surrounding the QCP. Image taken, A. P. Mackenzie, s. A. Grigera, from *A Quantum Critical Route to Field-Induced Superconductivity* Science 26 AUG 2005 : 1330-1331

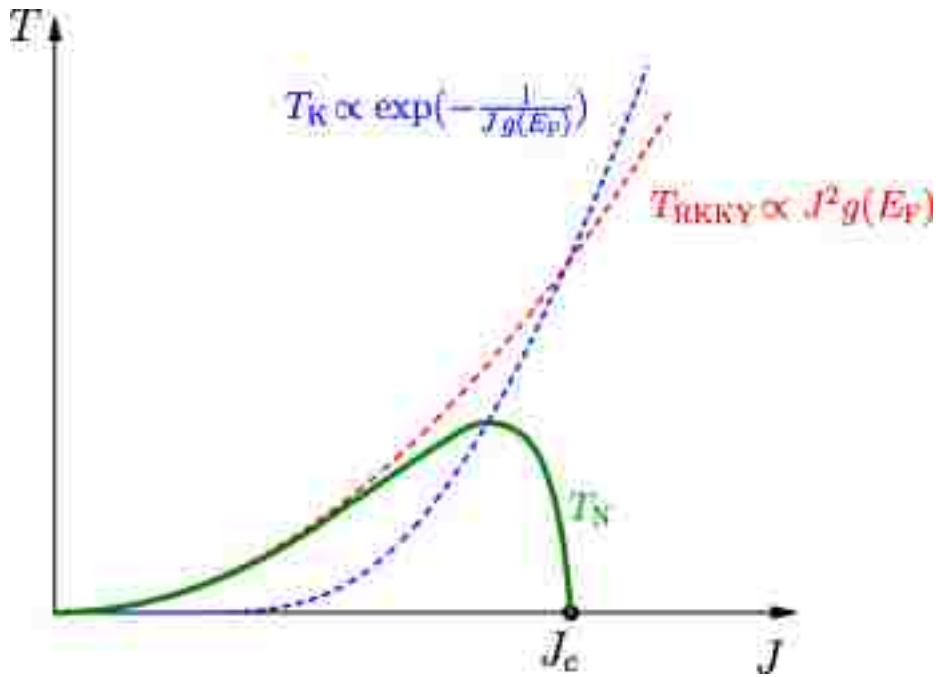


**Figure 4. Dziabach diagram**

This shows the competing RKKY interaction with Kondo screening resulting in a quantum critical point. F Steglich et al *Magnetism, f-electron localization and superconductivity in 122-type heavy-fermion metals*. 2012 J. Phys.: Condens. Matter 24 294201



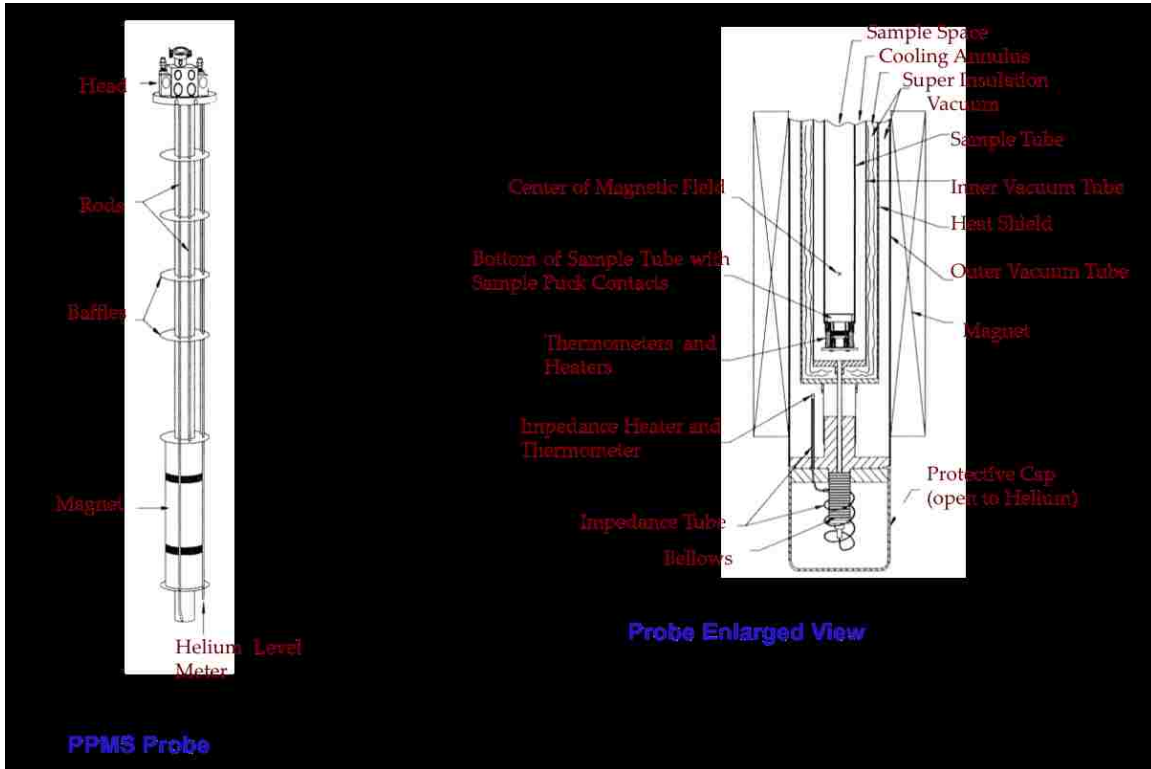


**Figure 5. Physical Properties Measurement System (PPMS) probe chamber.**

This illustrates the probe and sample chamber that use used for both magnetic susceptibility and calorimeter measurements.

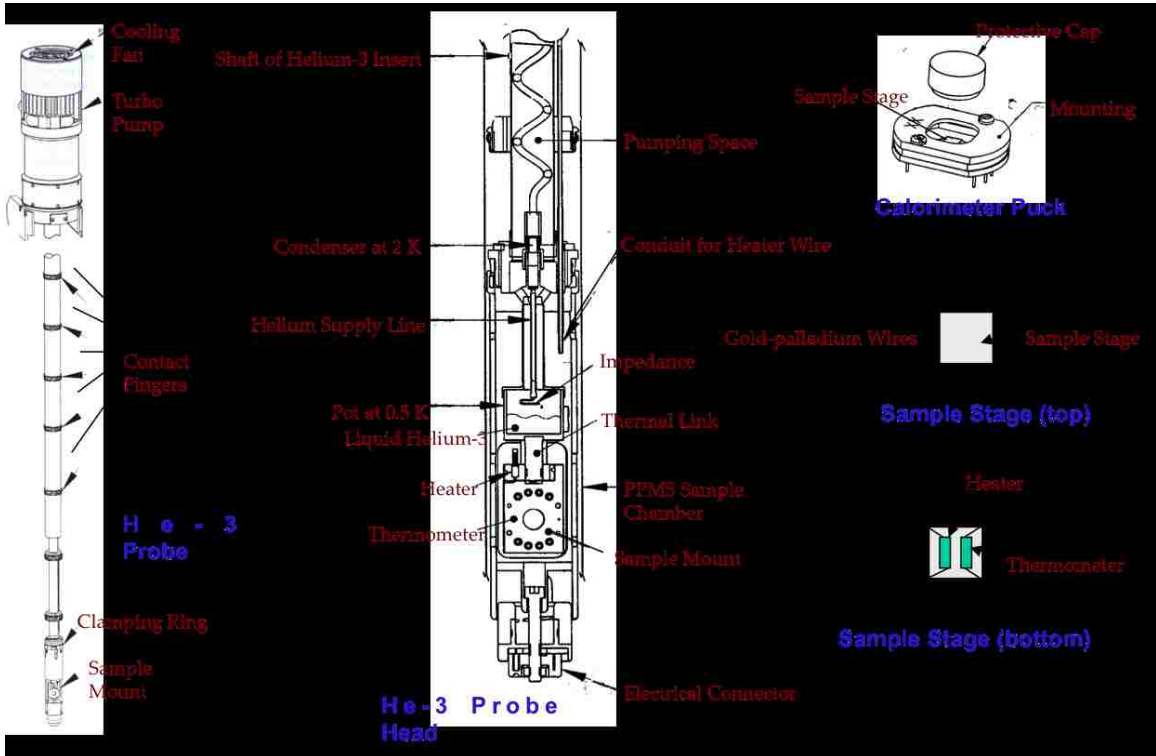


**Figure 6. Physical Properties Measurement System (PPMS) He-3 and calorimeter puck.**

The He-3 refrigerator with the calorimeter puck is shown here. Temperatures down to 0.35 K can be reached. The samples are placed on the sample stage and are adhered with thermal grease.

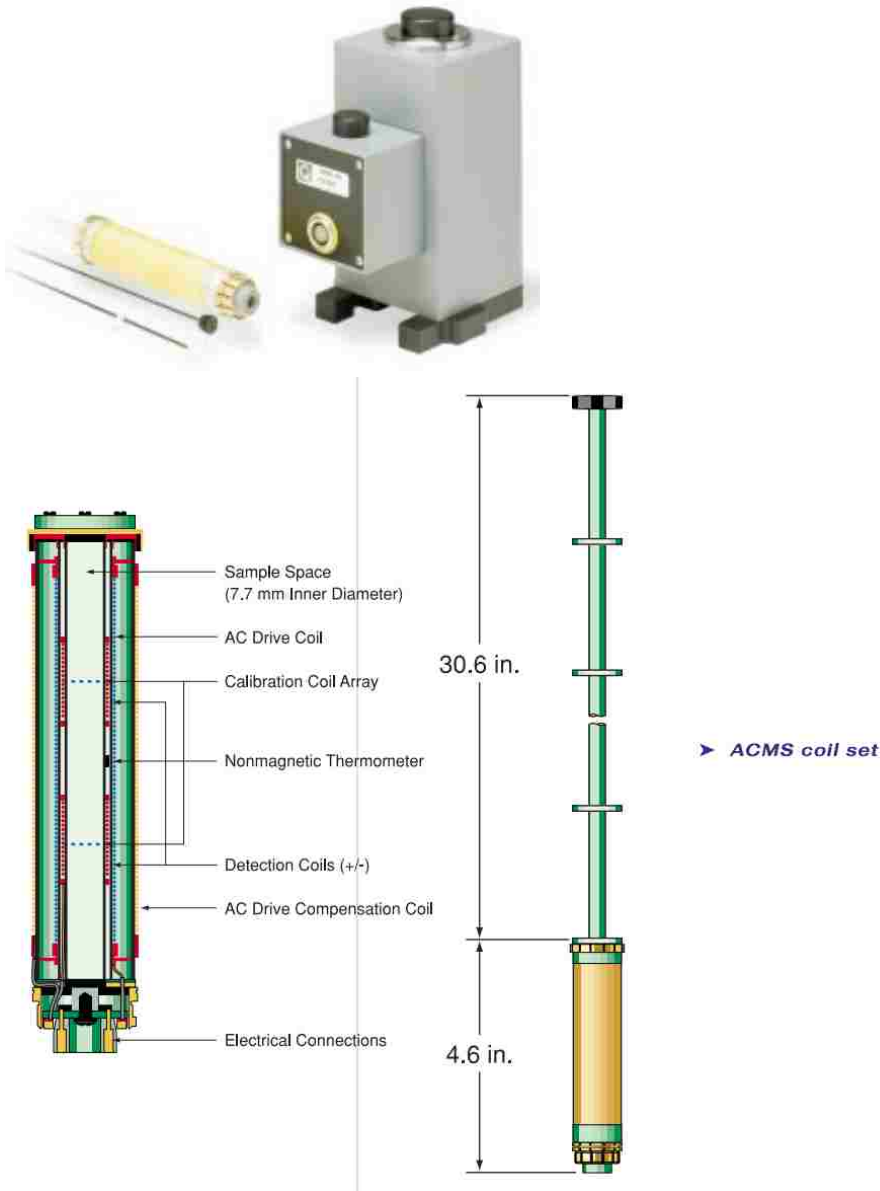


**Figure 7. Physical Properties Measurement System (PPMS) magnetometry system.**

A sample is placed inside a capsule that is attached to a non-magnetic rod. The sample is inserted into the ACMS coil with the rod attached to the drive motor positioned above the sample chamber and the sample is centered. Both DC magnetization or AC susceptibility can be measured. Images were taken from the Quantum Design PPMS magnetometry brochure.



**Figure 8. Princeton symmetric type diamond anvil cell (DAC)**

This is a picture of the diamond anvil cell used for all high pressure measurements performed here.

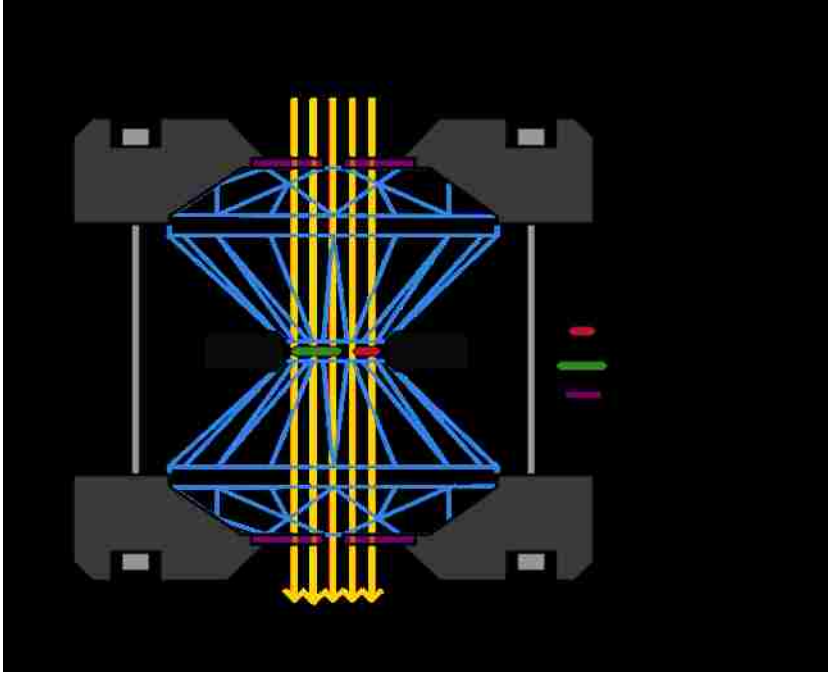


**Figure 9. Diamond anvil cell schematic**

A DAC generates pressure to a sample through the use of two opposing diamond anvils where the force is supplied through the tightening of a series of screws or a membrane. The small area of the culet compared to the area of the back of the diamond enables the creation of very large pressures with modest force. The diamonds also proved convenient windows to visually inspect the sample space or perform optical measurements. The gasket material is usually steel or rhenium. If beryllium is used, the gasket can be a convenient window for X-ray measurements. Using a small ruby sphere and measuring the shift in its fluorescence, pressure can be measured. Performing XRD measurements on a gold or other standard can be done to measure pressure as well.

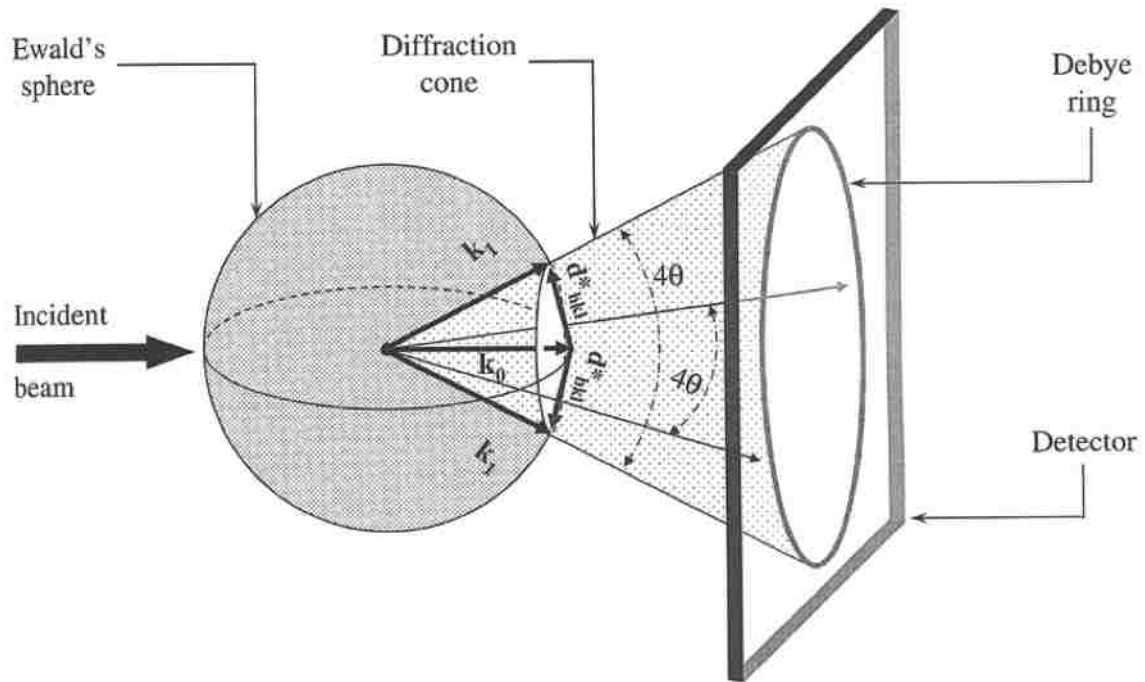


**Figure 10. X-ray diffraction geometry.**

Shown here is the standard geometry used to create x-ray diffraction images. The incident beam is refracted off of the crystal structure and the scattered light is collected on a plate or detector. From this geometry, the angle of refracted light can be measured with each angle resolved peak corresponding to a particular spacing between planes of the crystal. Figure taken from Fundamentals of Powder Diffraction and Structural Characterization of Materials [33].

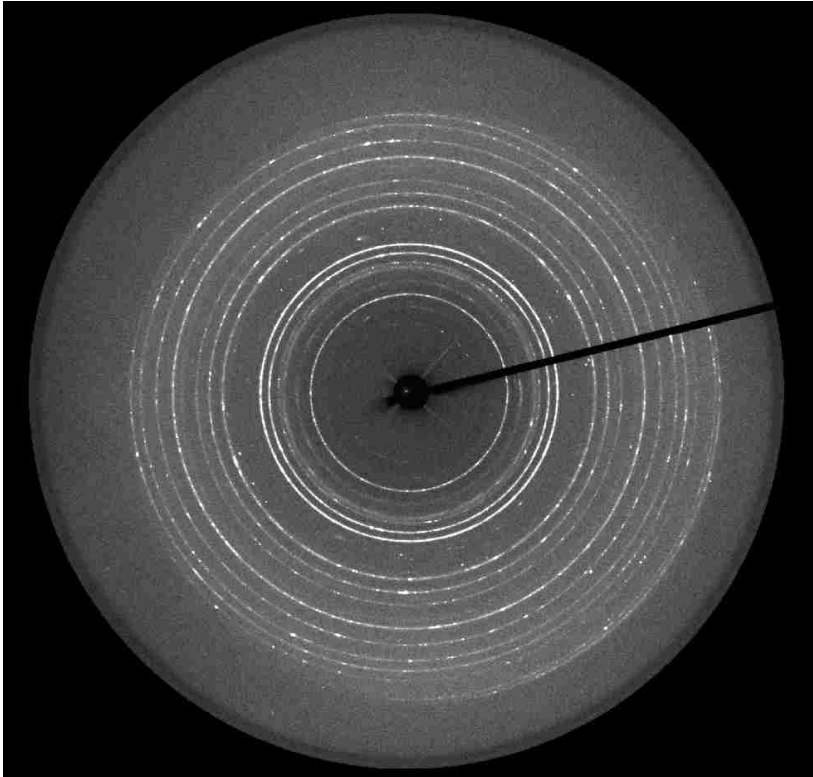


**Figure 11. X-Ray diffraction image**

This is an example powder diffraction image. This particular sample is  $\text{EuMn}_2\text{Si}_2$  inside a diamond anvil cell. The raw data shown requires software to integrate the rings into a diffraction pattern and then also to analyze the pattern to obtain lattice information.

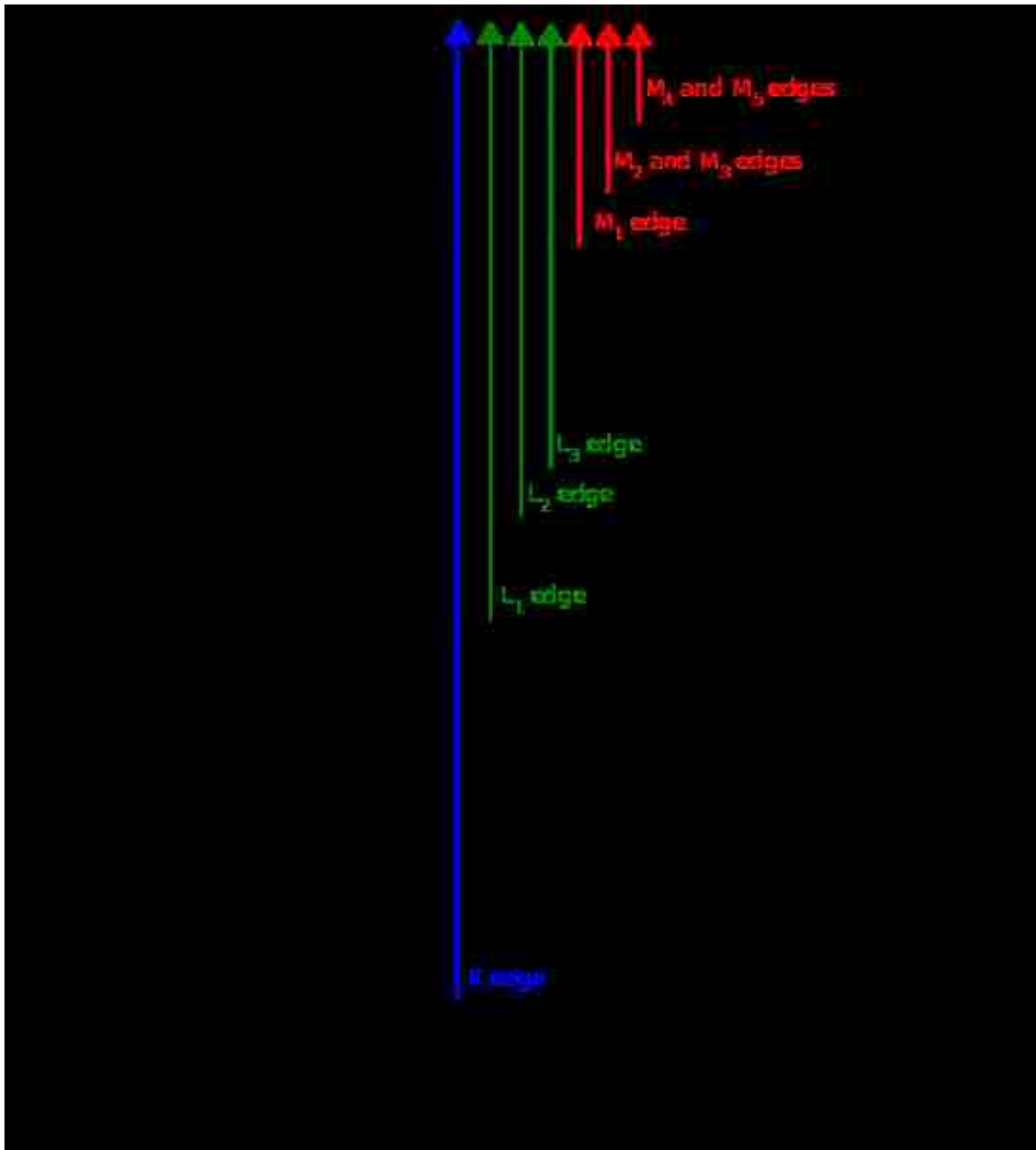
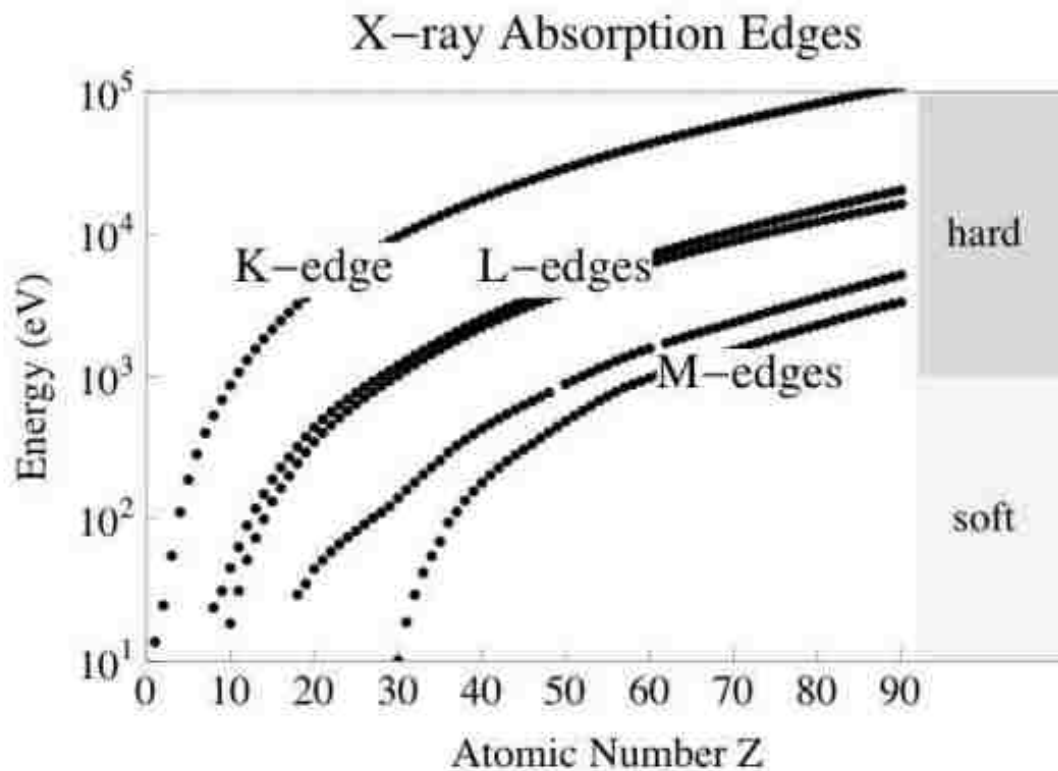


Figure 12. X-ray absorption spectroscopy (XAS) edges.





**Figure 13. X-ray absorption spectroscopy (XAS) edges by atomic number.**

Energy of the K, L1, L3, M1, and M5 X-ray absorption edges as a function of atomic number. This image was taken from Brink, Jeroen van den, *Resonant Inelastic X-ray Scattering on Elementary Excitations*

Edge	keV	Å
K	48.5190	0.2555
L-I	8.0520	1.5398
L-II	7.6171	1.6277
L-III	6.9769	1.7771
M1	1.8000	6.8880
M2	1.6139	7.6823
M3	1.4806	8.3739
M4	1.1606	10.6828
M5	1.1309	10.9633

**Table 2. Europium absorption energies and wavelengths.**

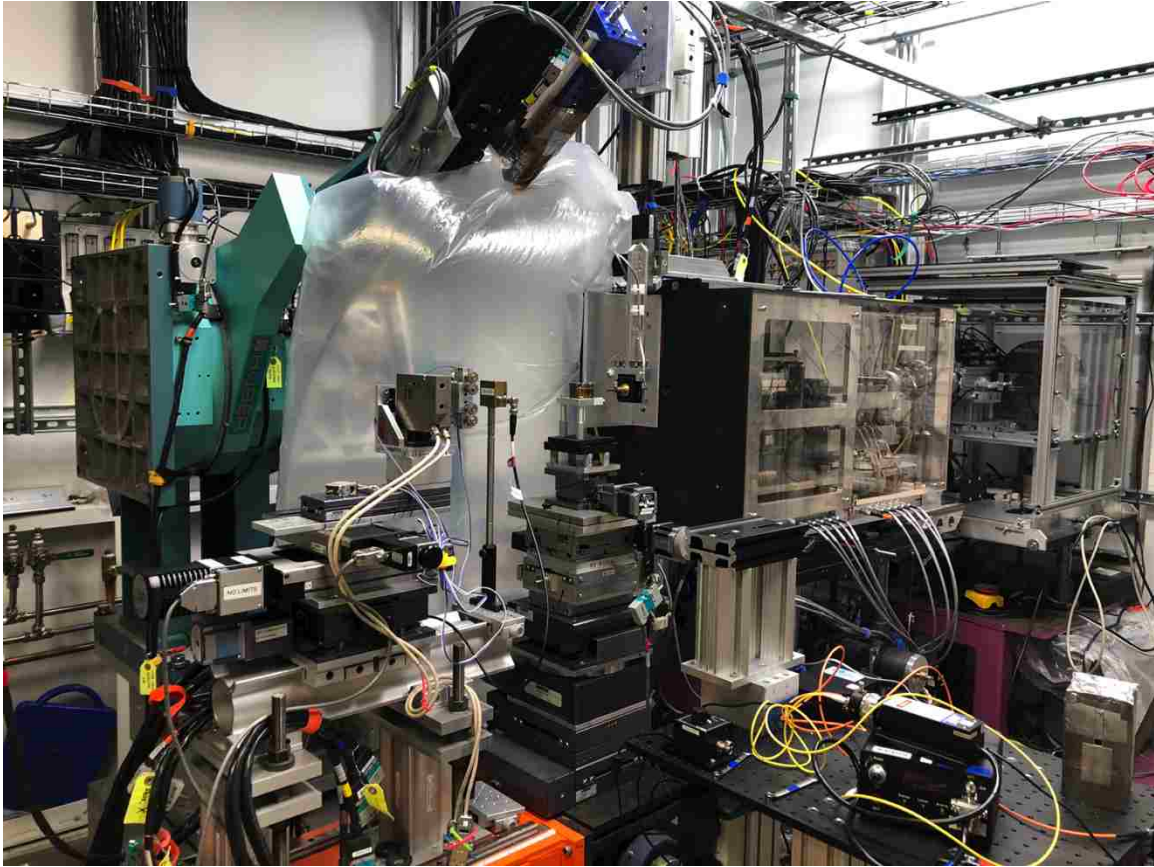


**Figure 14. Resonant X-ray emission spectroscopy (RXES) apparatus.**

This is inside the measurement hutch at IDD sector 16 at the Advanced Photon Source and Argonne National Laboratory. The High Pressure Collaborative Access Team (HPCAT) maintains this instrument. At almost the exact center of the image is the diamond anvil cell on top of a stage used to control its position. The large bag is filled with helium to reduce the attenuation of scattered photons by the atmosphere. The large green arm holds the detectors at the desired angles. On the far right is where the X-ray beam comes in and is diffracted through silicon crystals to select the desired energy. It is then collimated immediately before the DAC. Diodes before and after the DAC are present to perform X-ray absorption measurements and sample locating.

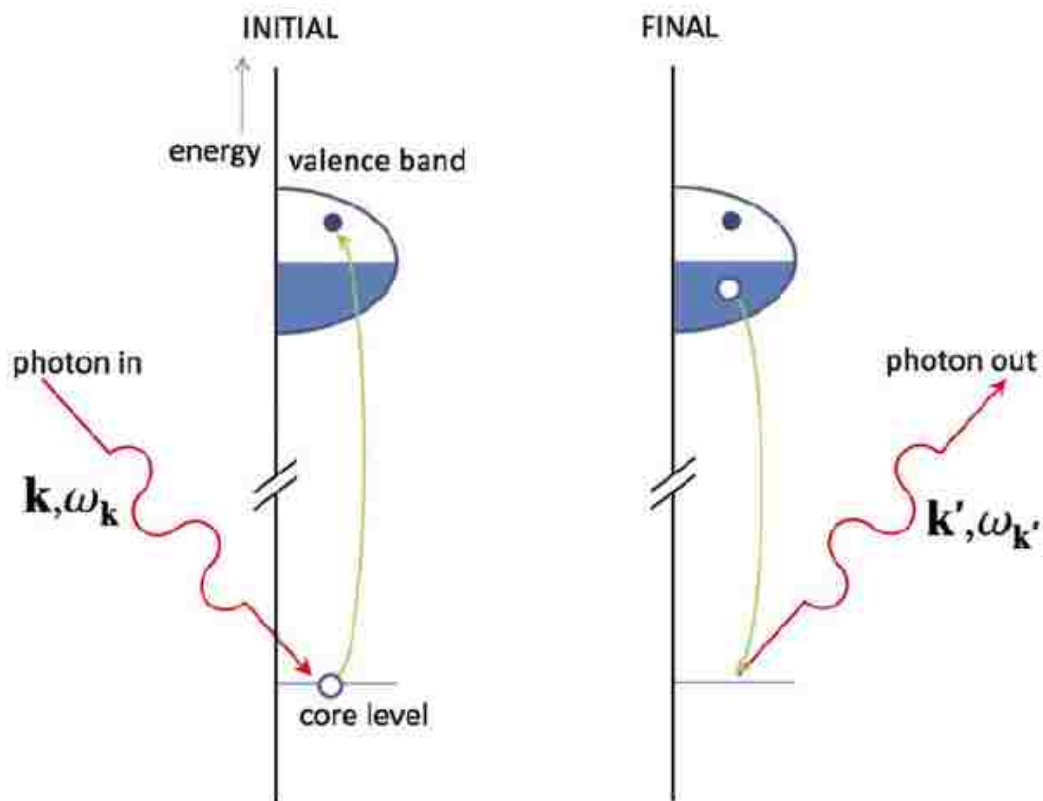


**Figure 15. Direct resonant inelastic X-ray spectroscopy (RIXS)**

In a direct RIXS process the incoming X-rays excite an electron from a deep-lying core level into the empty valence. The empty core state is then filled by an electron from the occupied states under the emission of an X-ray. This RIXS process creates a valence excitation with momentum  $\hbar\mathbf{k}' - \hbar\mathbf{k}$  and energy  $\hbar\omega_k - \hbar\omega_{k'}$ . [34] This image was taken from Brink, Jeroen van den, *Resonant Inelastic X-ray Scattering on Elementary Excitations*.

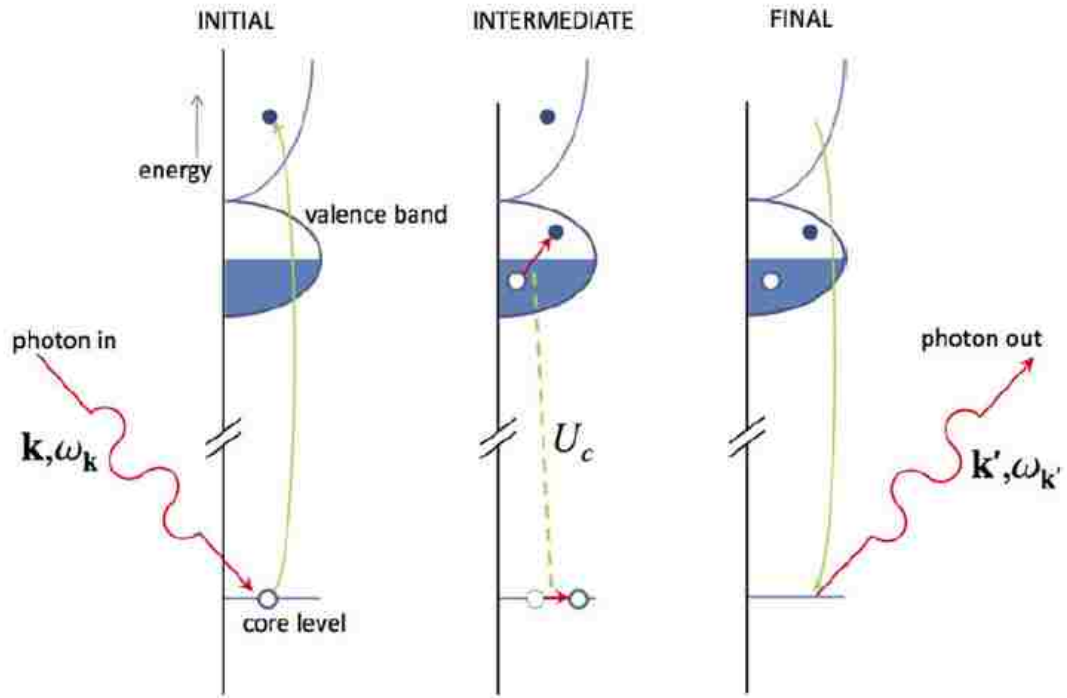


**Figure 16. Indirect resonant inelastic X-ray spectroscopy (RIXS)**

In an indirect RIXS process the incoming X-rays excite an electron from a deep-lying core level into the empty valence. [34] This image was taken from Brink, Jeroen van den, *Resonant Inelastic X-ray Scattering on Elementary Excitations*.

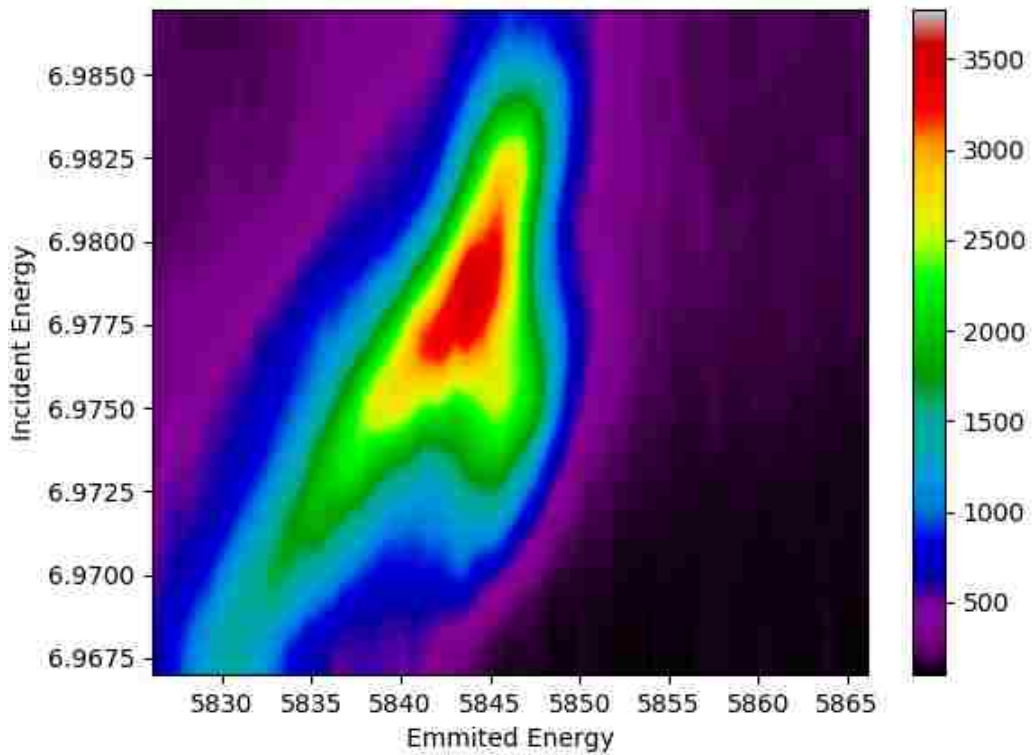


**Figure 17. Ambient RIXS data for  $\text{EuCo}_2\text{Si}_2$**

Europium RIXS data for  $\text{EuCo}_2\text{Si}_2$  is shown at ambient conditions. There is only one visible peak in the  $\text{Eu}^{3+}$  configuration. The strange shape of the peak is unknown but could be due to disorder in the crystal structure.

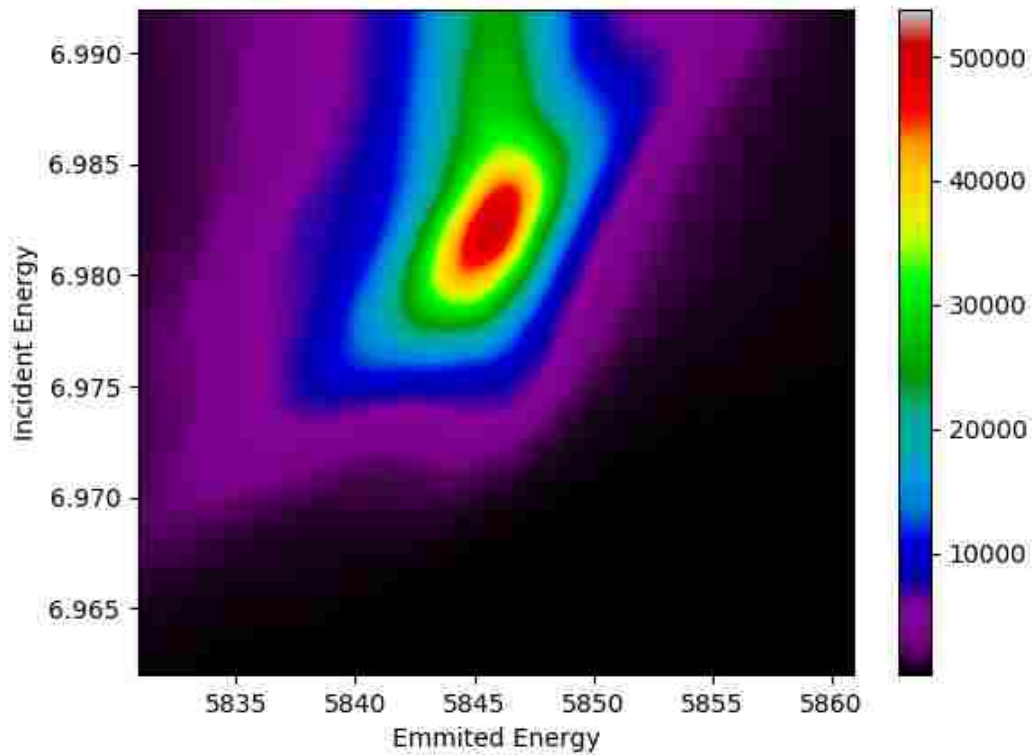


**Figure 18. RIXS data for  $\text{EuCo}_2\text{Si}_2$  at 10.5 GPa and ambient temperatures**

Europium RIXS data for  $\text{EuCo}_2\text{Si}_2$  is shown at 10.5 GPa and ambient temperature. There is only one visible peak and is only in the  $\text{Eu}^{3+}$  configuration.

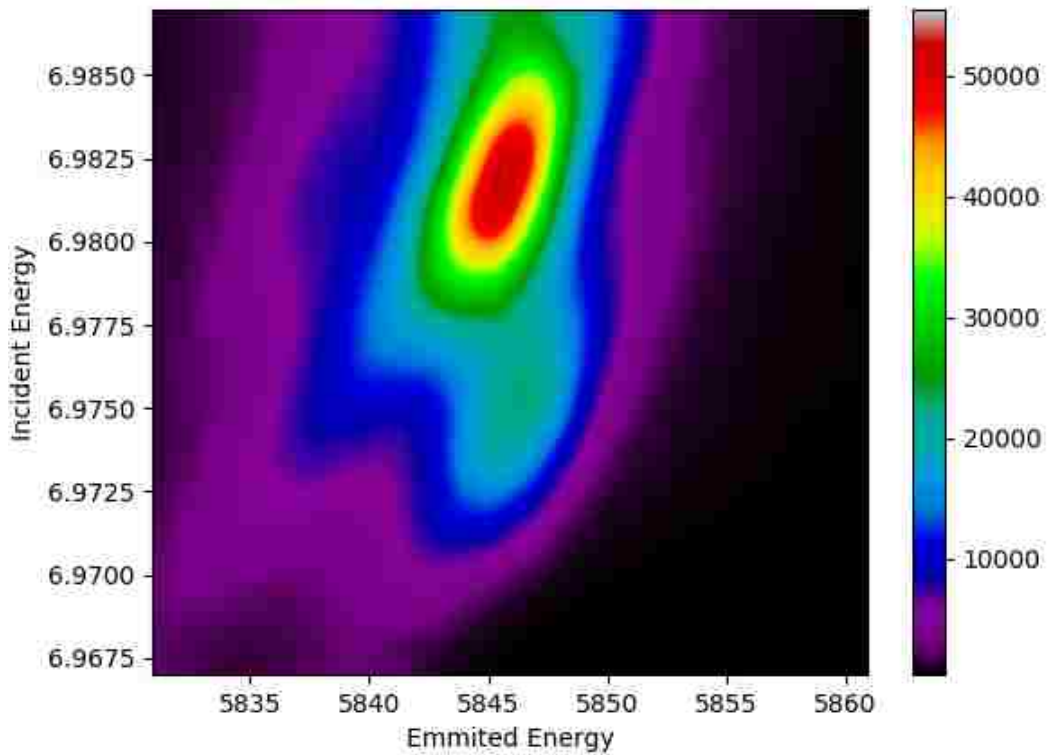


**Figure 19. Ambient RIXS data for  $\text{EuMn}_2\text{Si}_2$**

Europium RIXS data of  $\text{EuMn}_2\text{Si}_2$  at ambient conditions is shown. Two distinct peaks can be seen corresponding to the  $\text{Eu}^{2+}$  and  $\text{Eu}^{3+}$  states. Fits to this data show that the valence at ambient conditions is mostly trivalent at +2.76.



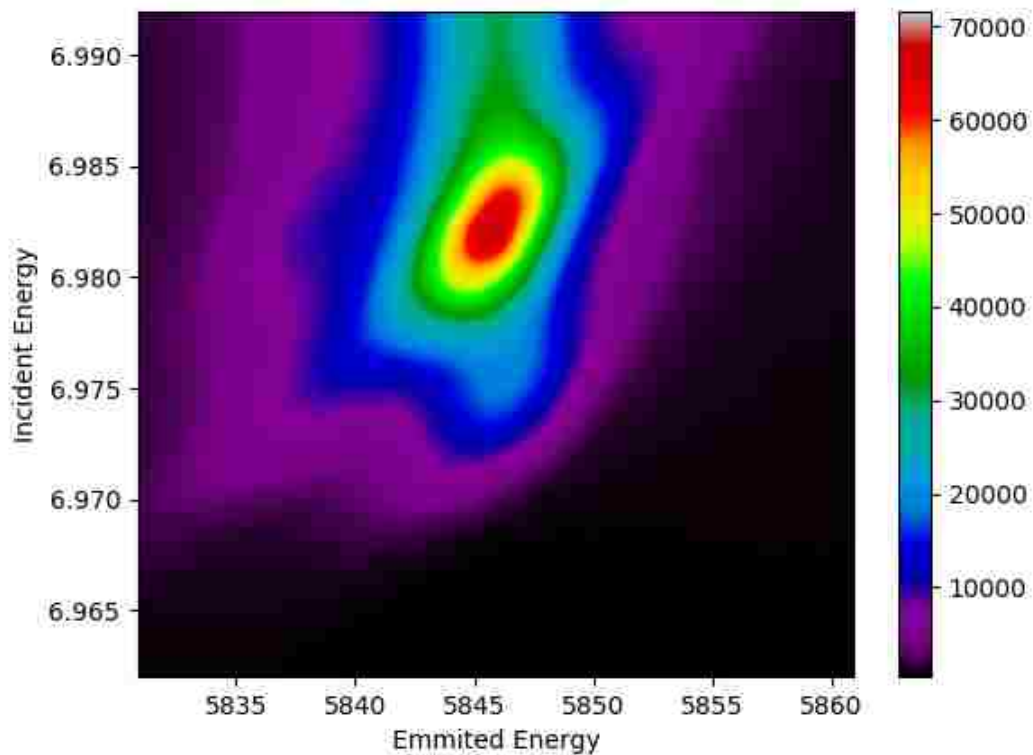


**Figure 20. RIXS data for  $\text{EuMn}_2\text{Si}_2$  at 13.1GPa at ambient temperature.**

Europium RIXS data of  $\text{EuMn}_2\text{Si}_2$  at 13.1 GPa and ambient temperature is shown. Two distinct peaks can still be seen corresponding to the  $\text{Eu}^{2+}$  and  $\text{Eu}^{3+}$  states. Fits to this data show that the valence at ambient conditions is almost completely trivalent at +2.93.

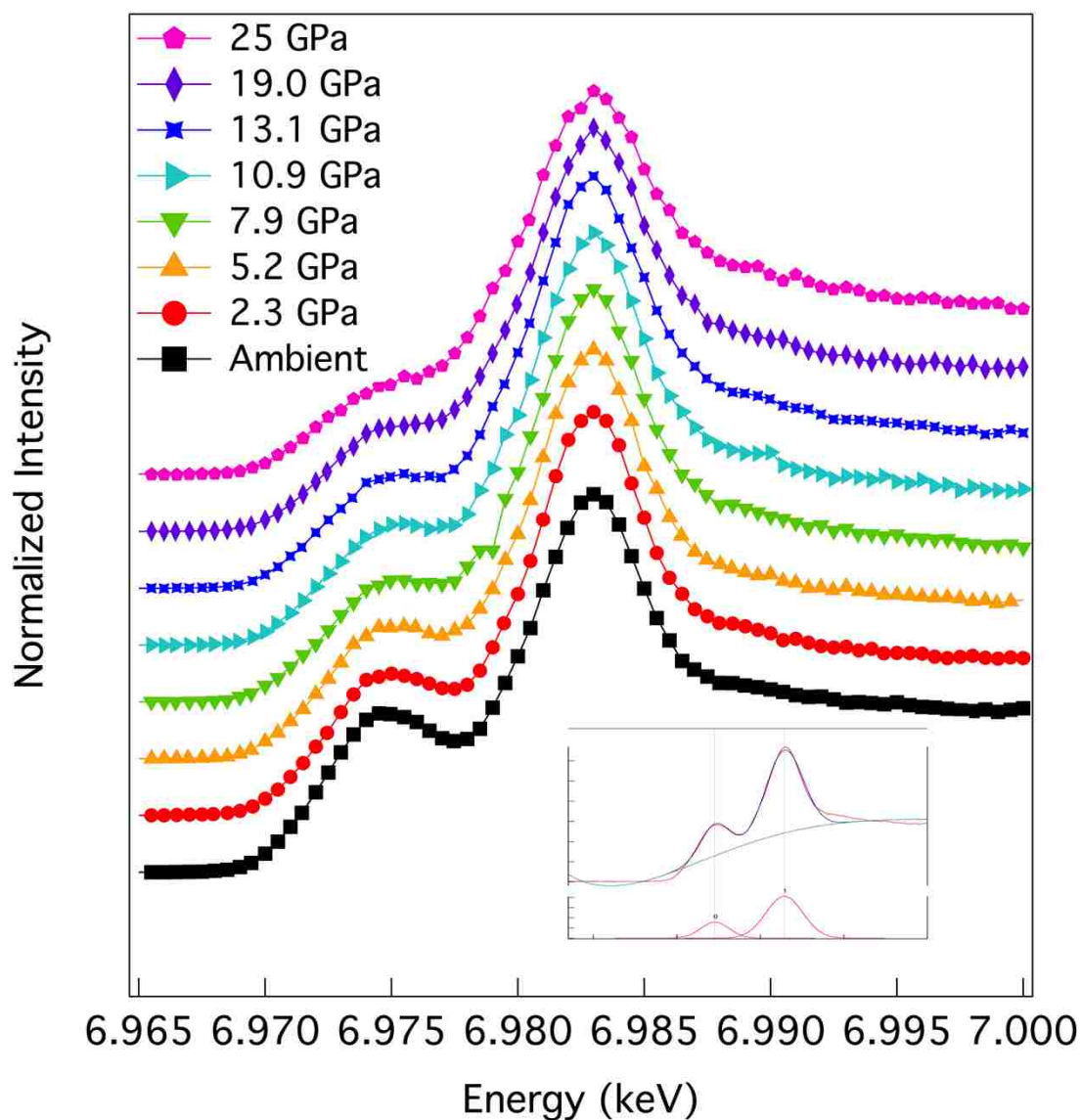


**Figure 21. Partial fluorescence yield (PFY) data for  $\text{EuMn}_2\text{Si}_2$  at multiple pressures at ambient temperature.**

Europium PFY data of  $\text{EuMn}_2\text{Si}_2$  at multiple pressures and ambient temperature is shown. Two distinct peaks can still be seen corresponding to the  $\text{Eu}^{2+}$  and  $\text{Eu}^{3+}$  states in the PFY data. An example fit to the PFY data can be seen in the inset.

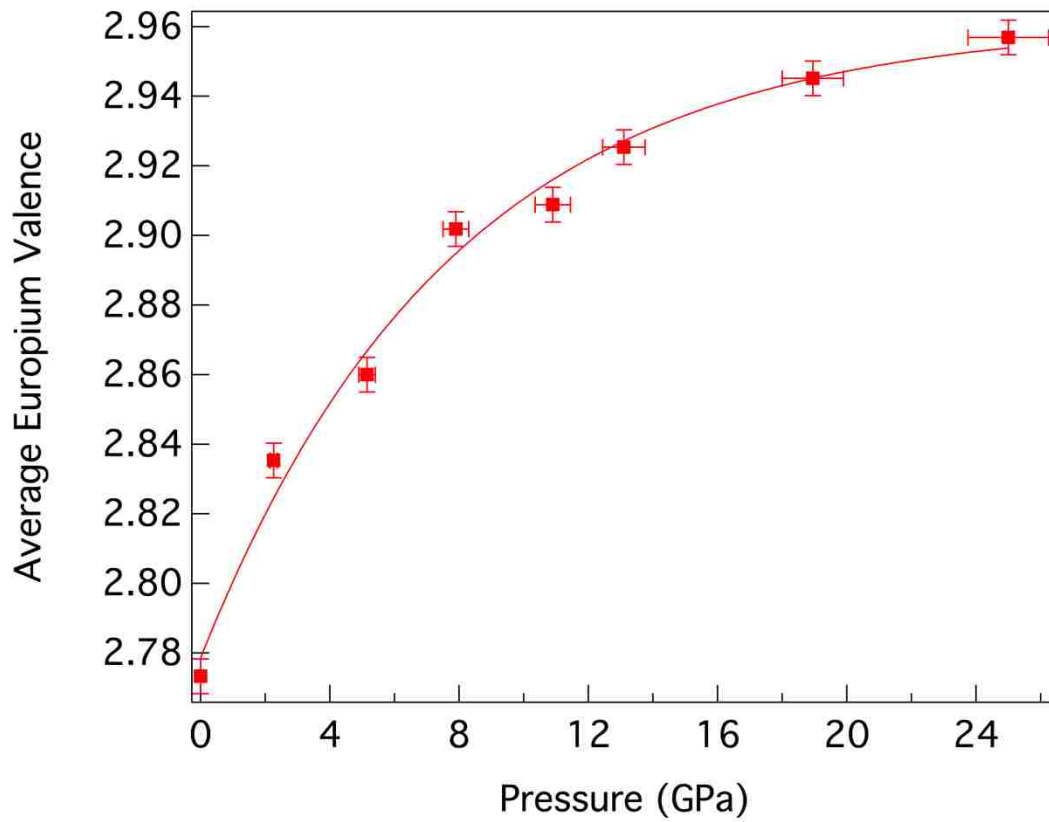


**Figure 22. Europium valence as a function of pressure in  $\text{EuMn}_2\text{Si}_2$**

Plotted here is the europium valence of  $\text{EuMn}_2\text{Si}_2$  as function of pressure at ambient temperature. The europium valence clearly approaches +3 as pressure increases.

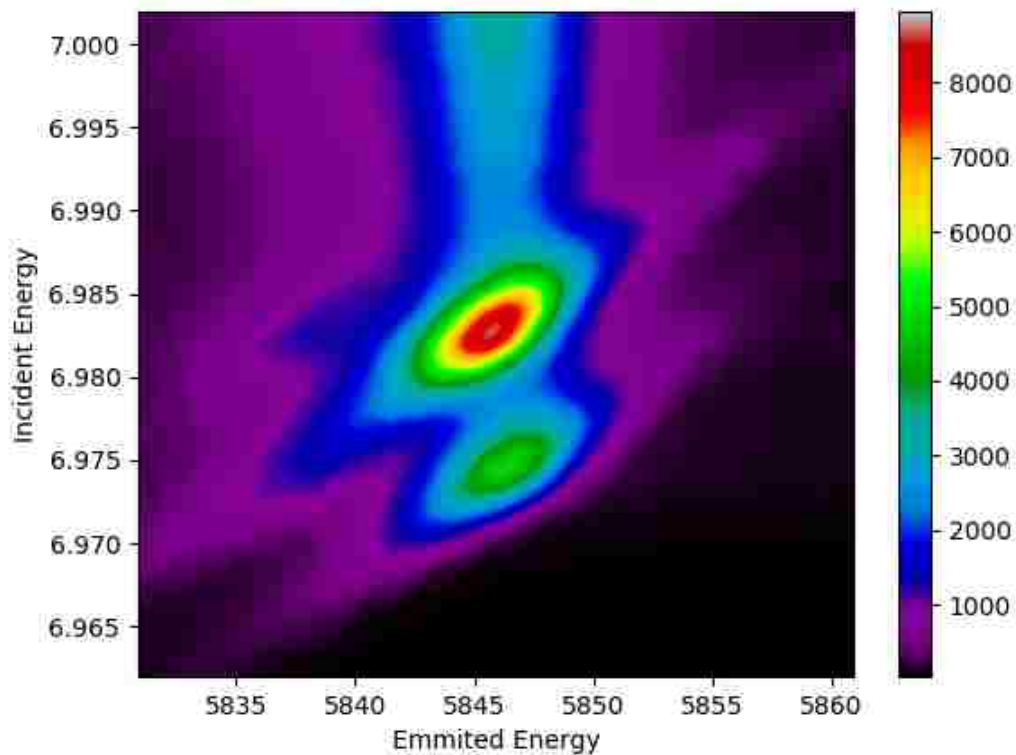


**Figure 23. RIXS data for  $\text{Eu}_5\text{In}_2\text{Sb}_6$  at ambient temperatures and pressures.**

Europium RIXS data for  $\text{Eu}_5\text{In}_2\text{Sb}_6$  is shown at ambient temperature and pressure. Two distinct peaks can be seen corresponding to the  $\text{Eu}^{2+}$  and  $\text{Eu}^{3+}$  states. The shape of the trivalent peak indicates that there may be 2 different site locations that are trivalent. Fits to this data show that the net valence is +2.63 or +2.70 if three peaks are used.

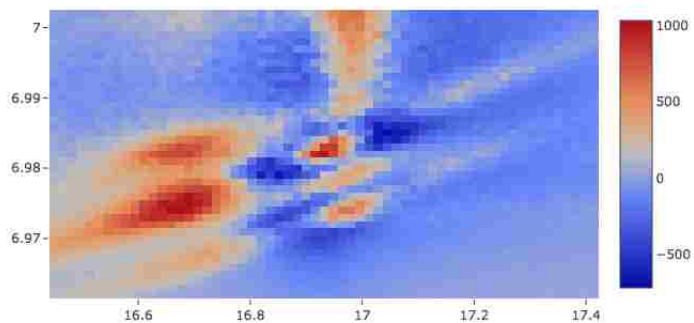
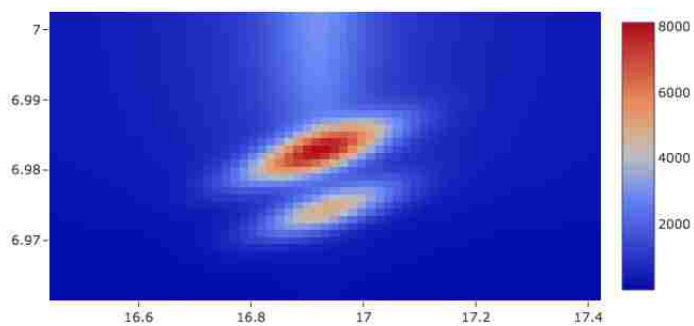
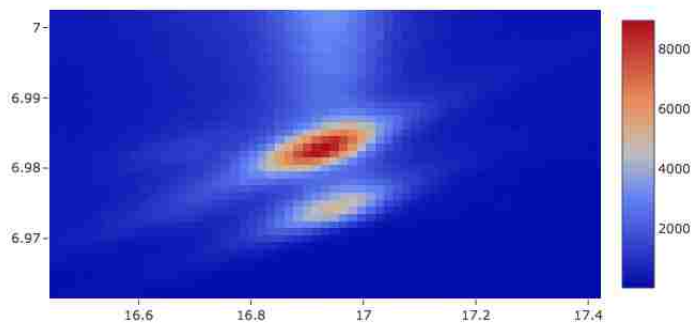


**Figure 24. fit of RXES data for  $\text{Eu}_5\text{In}_2\text{Sb}_6$  at ambient temperatures and pressures.**

The first image is the actual data, the second is the fit of two peaks using equations 75 and 78. The third image shows the residual of the fit.

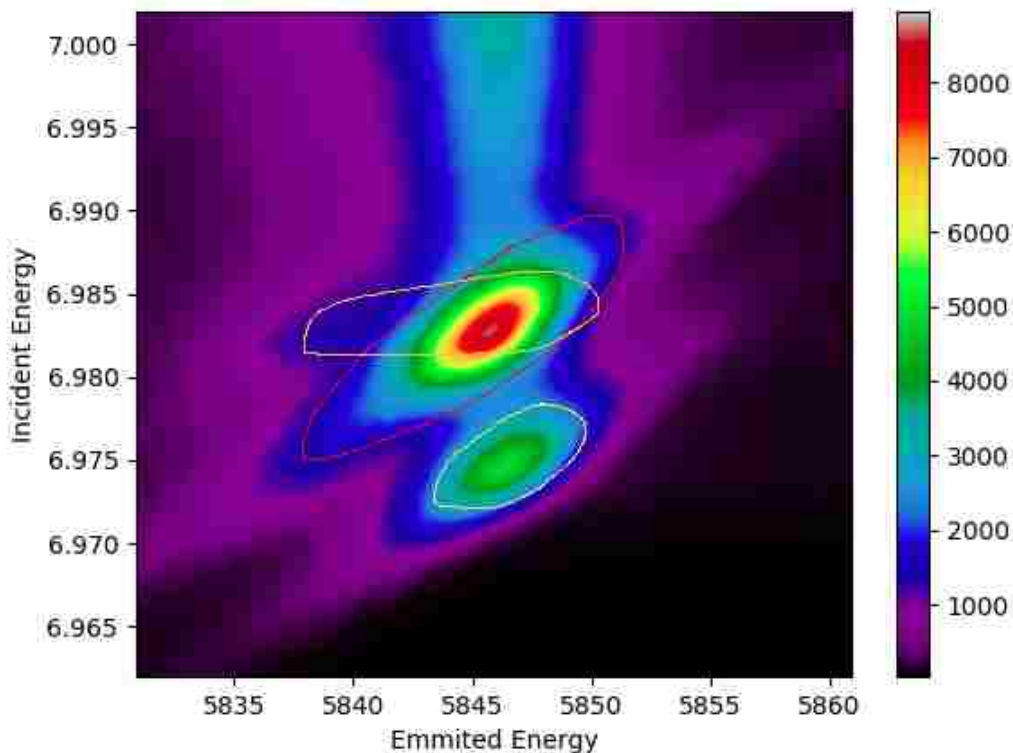


**Figure 25. RIXS data for  $\text{Eu}_5\text{In}_2\text{Sb}_6$  at ambient temperatures and pressures showing three possible peaks.**

Europium RIXS data for  $\text{Eu}_5\text{In}_2\text{Sb}_6$  is shown at ambient temperature and pressure. Two distinct peaks can be seen corresponding to the  $\text{Eu}^{2+}$  and  $\text{Eu}^{3+}$  states. The shape of the trivalent peak indicates that there may be 2 different site locations that are trivalent. Fitting three different peaks gives occupancy of 0.40 and 0.30  $\text{Eu}^{3+}$  and 0.30  $\text{Eu}^{2+}$ . This matches exactly the different site locations present in the ambient crystal and implies that this system is not actually a mixed valence system, but a system with different sight locations having different valence. The net valence from this fit is +2.70.

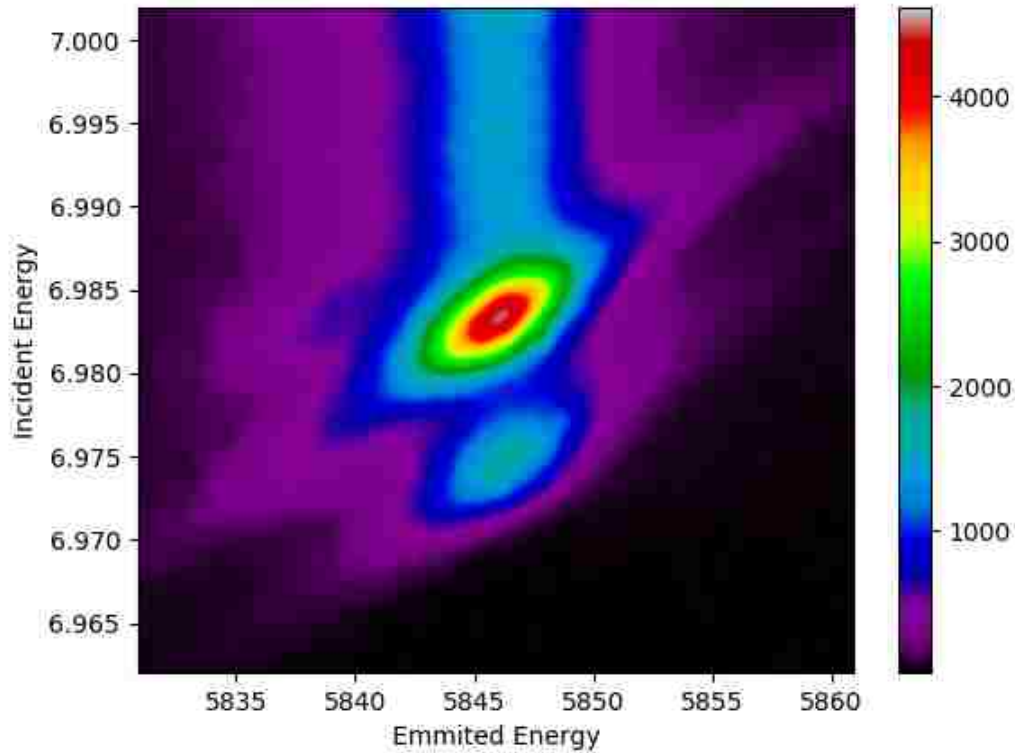


**Figure 26. RIXS data for  $\text{Eu}_5\text{In}_2\text{Sb}_6$  at ambient temperatures and 5.86 GPa.**

Europium RIXS data for  $\text{Eu}_5\text{In}_2\text{Sb}_6$  is shown at ambient temperature and 5.86 GPa. Two distinct peaks can be seen corresponding to the  $\text{Eu}^{2+}$  and  $\text{Eu}^{3+}$  states. Fits to this data show that the valence is +2.69 showing that continued increasing pressure moves the valence towards +3. Two different  $\text{Eu}^{3+}$  peak shapes still appear to be present.

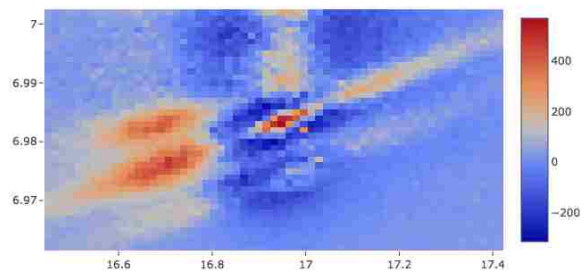
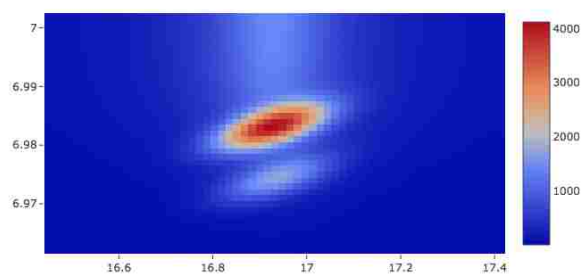
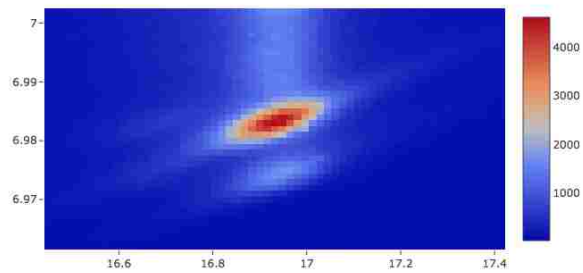


**Figure 27. fit of RXES data for  $\text{Eu}_5\text{In}_2\text{Sb}_6$  at ambient temperatures and 5.86 GPa.**

The first image is the actual data, the second is the fit of two peaks using equations 75 and 78. The third image shows the residual of the fit.



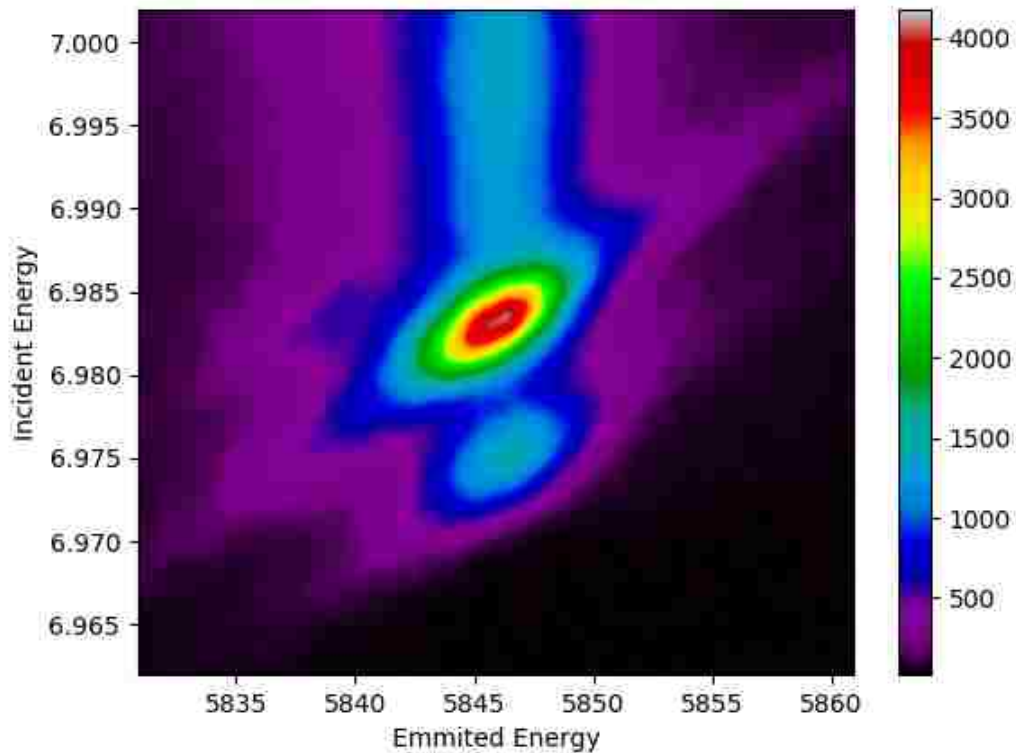


**Figure 28. RIXS data for  $\text{Eu}_5\text{In}_2\text{Sb}_6$  at ambient temperatures and 9.5 GPa.**

Europium RIXS data for  $\text{Eu}_5\text{In}_2\text{Sb}_6$  is shown at ambient temperature and 9.5 GPa. Two distinct peaks can be seen corresponding to the  $\text{Eu}^{2+}$  and  $\text{Eu}^{3+}$  states. Fits to this data show that the valence is +2.73 showing that continued increasing pressure moves the valence towards +3. Two different  $\text{Eu}^{3+}$  peak shapes still appear to be present.

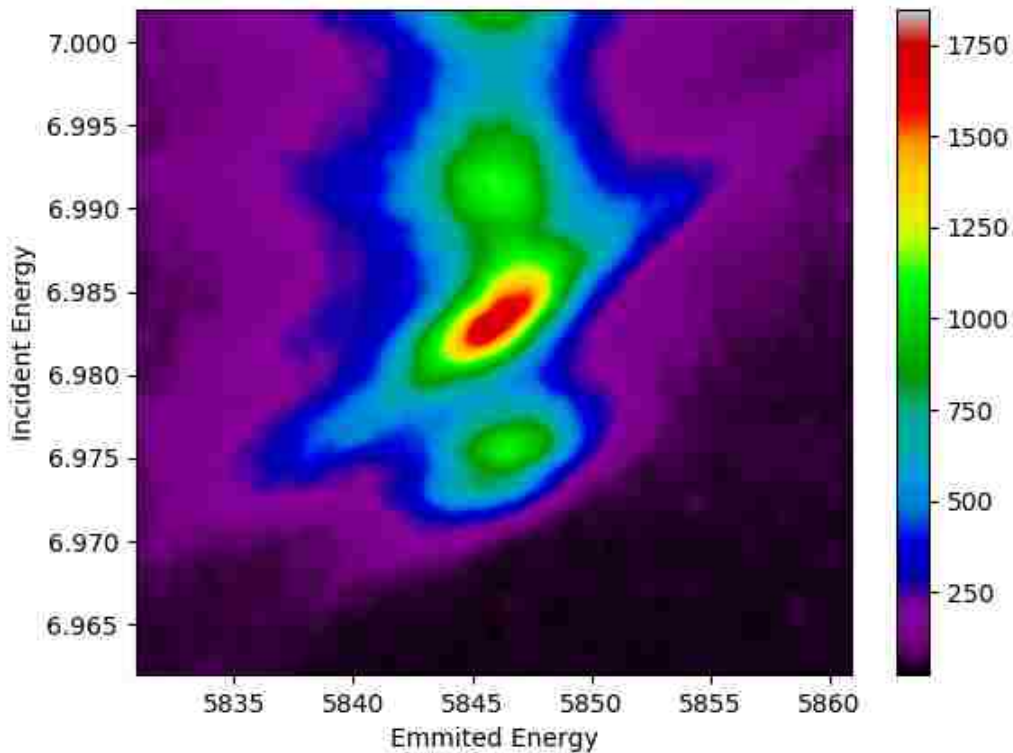


**Figure 29. RIXS data for  $\text{Eu}_5\text{In}_2\text{Sb}_6$  at ambient temperatures and 16 GPa.**

Europium RIXS data for  $\text{Eu}_5\text{In}_2\text{Sb}_6$  is shown at ambient temperature and 16 GPa. A phase transition is observed, as all of the peaks have completely changed shape. Two peaks can be seen corresponding to the  $\text{Eu}^{2+}$  and  $\text{Eu}^{3+}$  states. A third peak higher in energy emerges as well. This could possibly be evidence of a  $\text{Eu}^{4+}$  state. With a fit to 3 peaks, we get occupancy of 0.23  $\text{Eu}^{2+}$ , 0.58  $\text{Eu}^{3+}$ , and 0.18  $\text{Eu}^{4+}$  giving a net valence of +2.94.

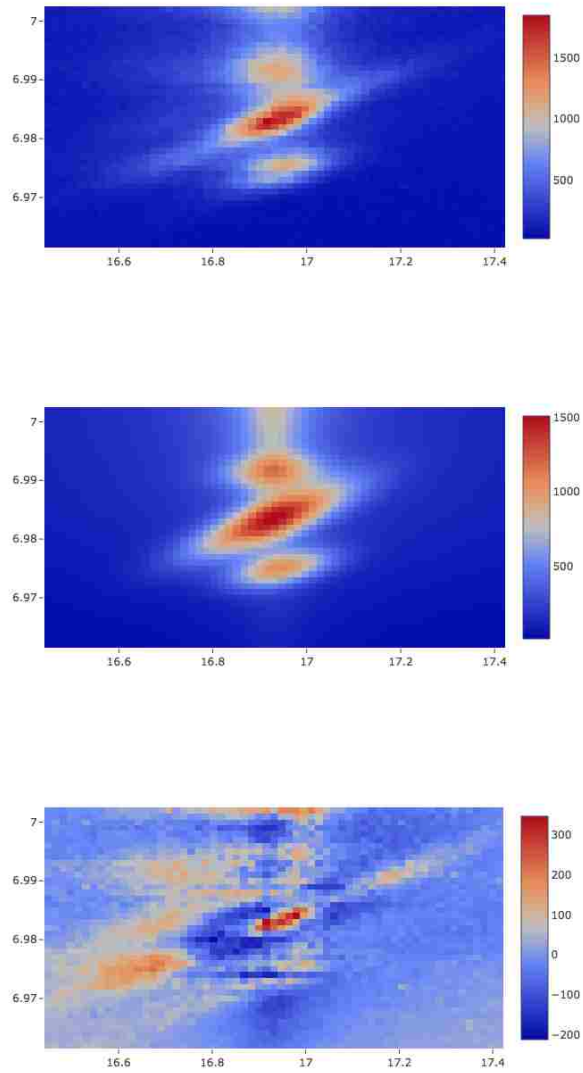


**Figure 30. fit of RIXS data for  $\text{Eu}_5\text{In}_2\text{Sb}_6$  at ambient temperatures and 16 GPa.**

The first image is the actual data, the second is the fit of two peaks using equations 75 and 78. The third image shows the residual of the fit.

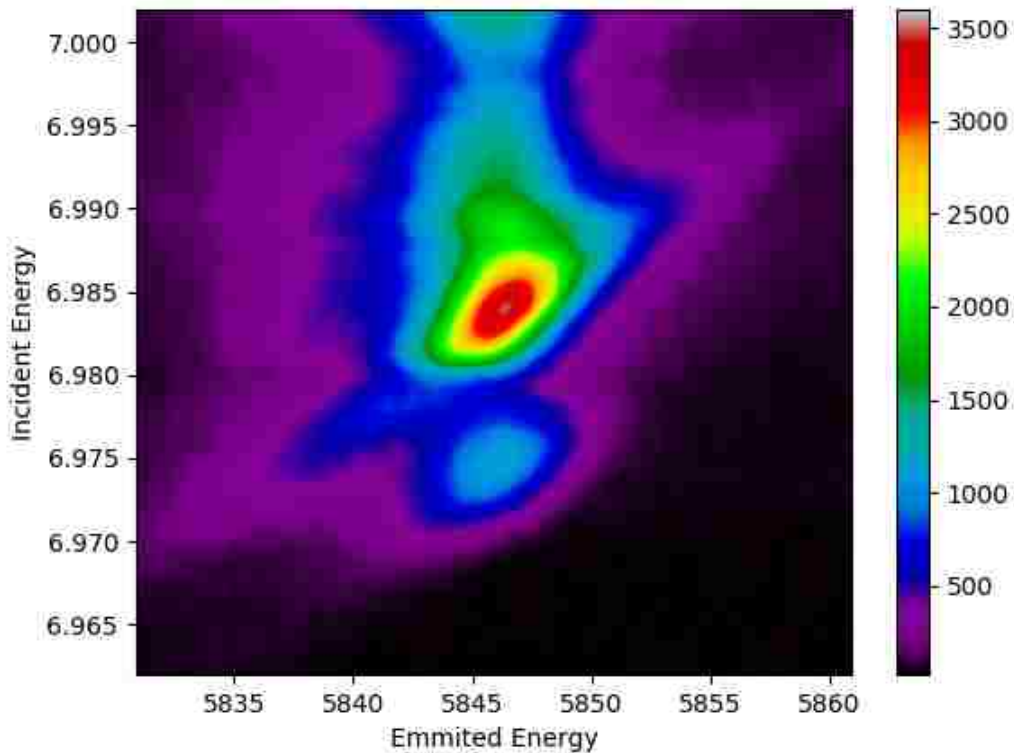


**Figure 31. RIXS data for  $\text{Eu}_5\text{In}_2\text{Sb}_6$  at ambient temperatures and 35 GPa.**

Europium RIXS data for  $\text{Eu}_5\text{In}_2\text{Sb}_6$  is shown at ambient temperature and 35 GPa. The material appears to remain in the same phase as at 16 GPa. The two peaks that are corresponding to the  $\text{Eu}^{2+}$  and  $\text{Eu}^{3+}$  states are visible in addition to the 3<sup>rd</sup> peak at higher energy. With a fit to 3 peaks, we get occupancy of 0.23  $\text{Eu}^{2+}$ , 0.67  $\text{Eu}^{3+}$ , and 0.09  $\text{Eu}^{4+}$  giving a net valence of +2.86. This implies that the  $\text{Eu}^{2+}$  state is unaffected by pressure, however there is a shift from the  $\text{Eu}^{4+}$  to  $\text{Eu}^{3+}$  with increasing pressure.

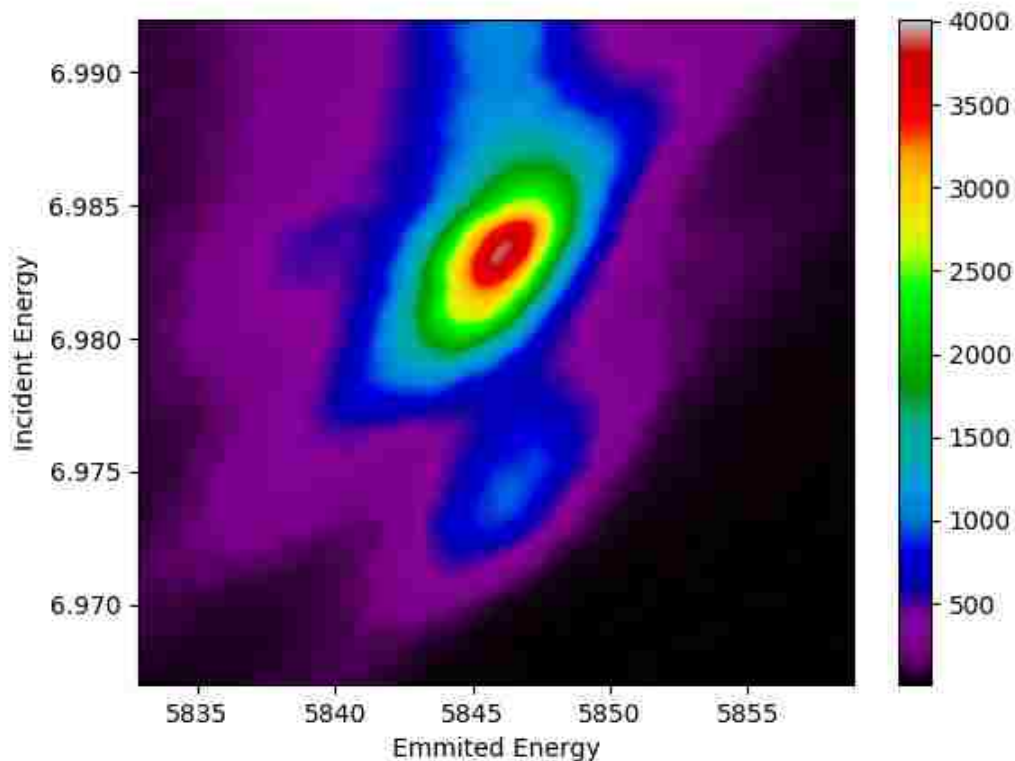


**Figure 32. RIXS data for  $\text{Eu}_5\text{In}_2\text{Sb}_6$  at 15.25 K and 1.0 GPa.**

Europium RIXS data for  $\text{Eu}_5\text{In}_2\text{Sb}_6$  is shown at 15.25 K and 1.0 GPa. Two distinct peaks can be seen corresponding to the  $\text{Eu}^{2+}$  and  $\text{Eu}^{3+}$  states. The shape of the trivalent peak indicates that there may be 2 different site locations that are trivalent as was the ambient temperature data in figure 16. Fits to this data show that the net valence is +2.83. Lowering the temperature moves europium from the  $\text{Eu}^{2+}$  state to the  $\text{Eu}^{3+}$  state. It is unclear if this is due to one of the transitions seen at low temperatures in the specific heat that has caused the valence to become unstable.

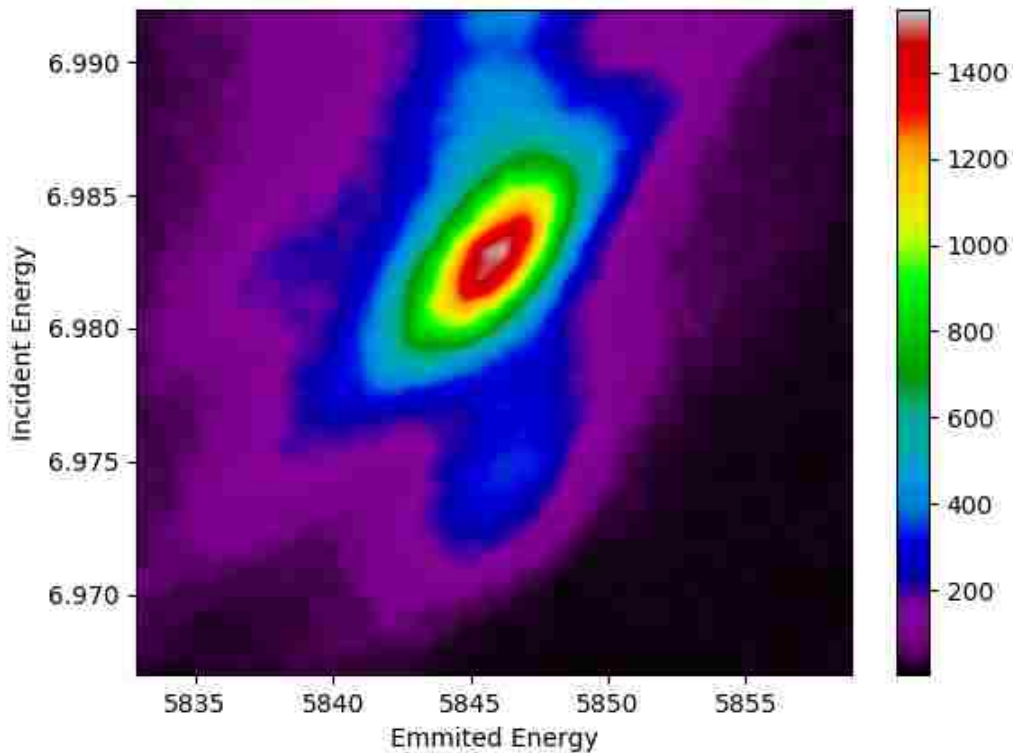


**Figure 33. RIXS data for  $\text{Eu}_5\text{In}_2\text{Sb}_6$  at 15.25 K and 19 GPa.**

Europium RIXS data for  $\text{Eu}_5\text{In}_2\text{Sb}_6$  is shown at 15.25 K and 19 GPa. Two distinct peaks can be seen corresponding to the  $\text{Eu}^{2+}$  and  $\text{Eu}^{3+}$  states. The shape of the trivalent peak indicates that there still may be 2 different site locations that are trivalent as was the ambient temperature data in figure 16. We noticeably do not see the same phase transition at low temperature at this pressure. Fits to this data show that the net valence is +2.87. Increasing the pressure at low temperature moves europium from the 2+ state to the 3+ state slightly. This is in contrast to the ambient temperature results.

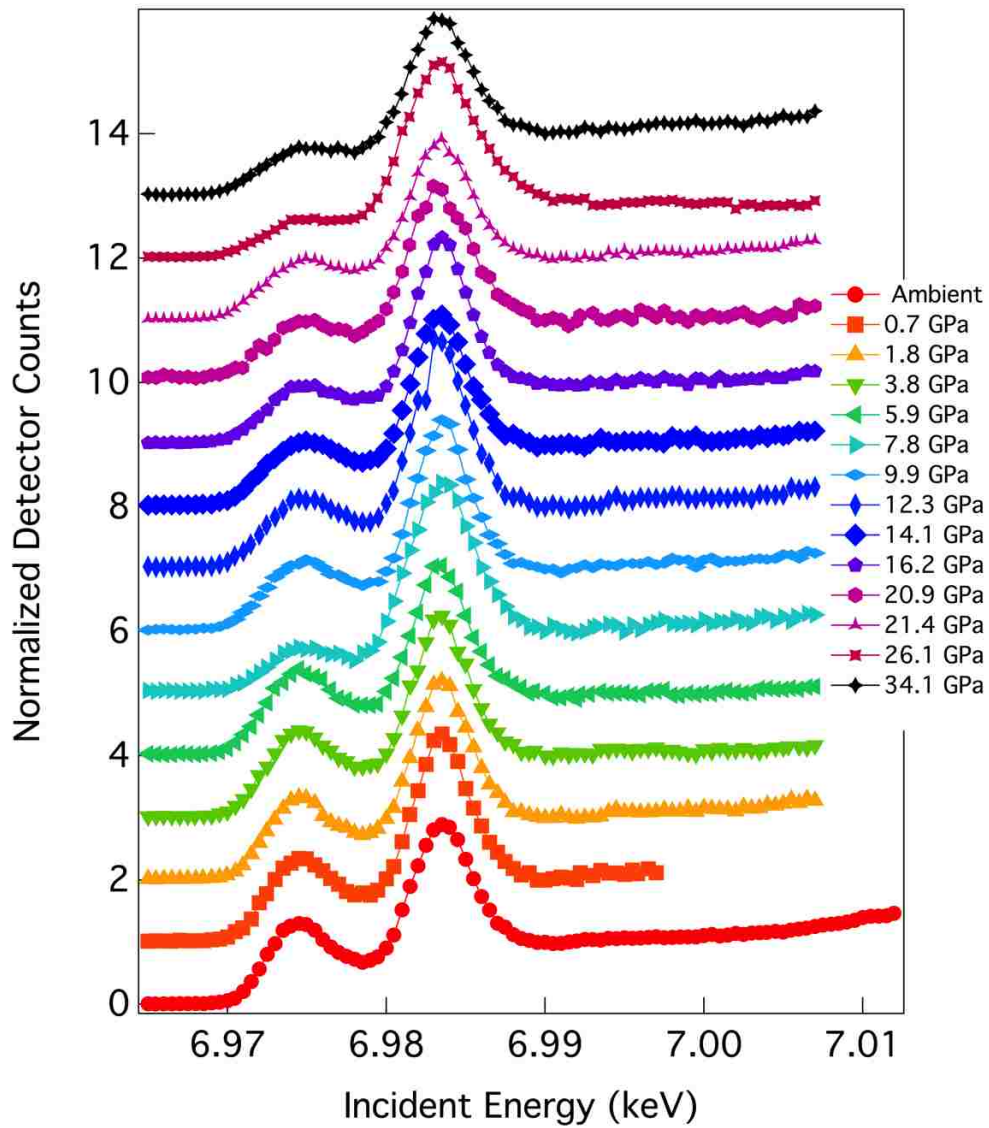


**Figure 34. Partial fluorescence yield (PFY) data for  $\text{Eu}_5\text{In}_2\text{Sb}_6$  at multiple pressures at ambient temperature.**

Europium PFY data of  $\text{Eu}_5\text{In}_2\text{Sb}_6$  at multiple pressures and ambient temperature is shown. Two distinct peaks can still be seen corresponding to the  $\text{Eu}^{2+}$  and  $\text{Eu}^{3+}$  states in the PFY data. The other features seen in the full RIXS data above 10 GPa is not as apparent indicating the structure may be too complex to accurately measure valence with PFY scans.

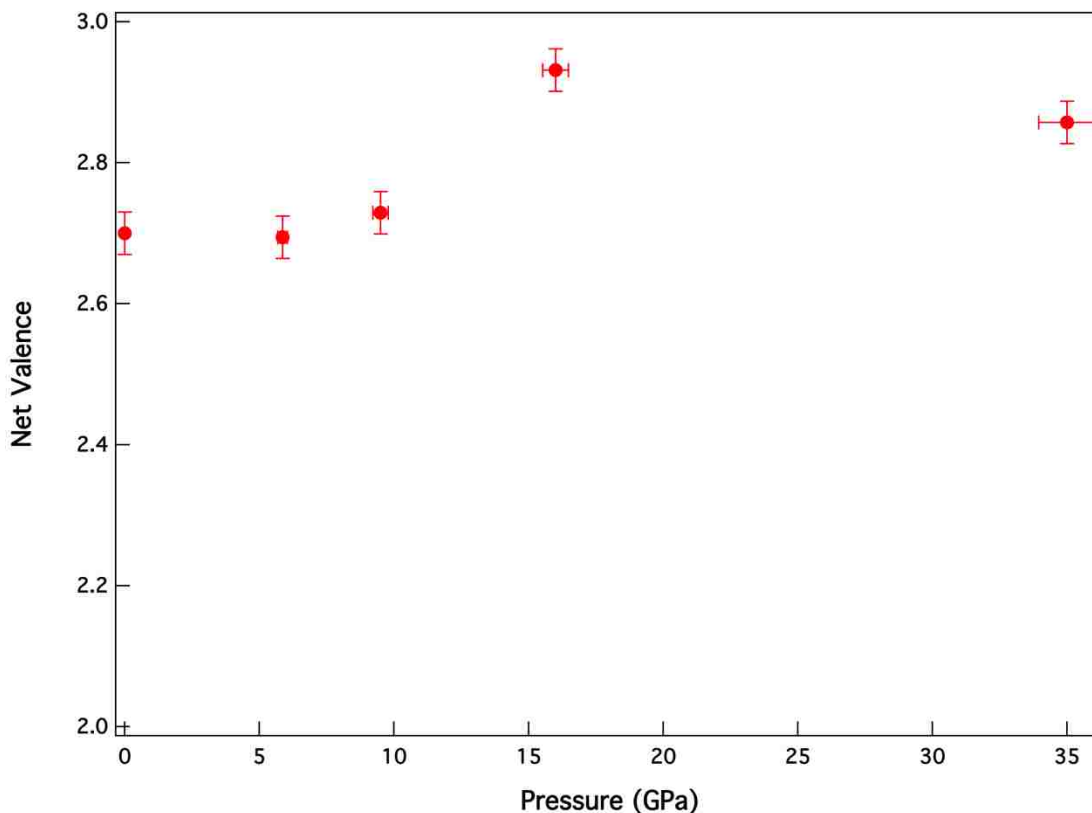


**Figure 35.  $\text{Eu}_5\text{In}_2\text{Sb}_6$  valence versus pressure.**

In the ambient phase, no shift in valence is seen within the experimental error. It is determined here that  $\text{Eu}_5\text{In}_2\text{Sb}_6$  is not a mixed valence system in the ambient phase, but does have europium at different sites possessing different valence. The high-pressure phase does show a measurable shift in valence with a theorized  $\text{Eu}^{4+}$  and  $\text{Eu}^{3+}$  mixed valence state that moves from  $\text{Eu}^{4+}$  to  $\text{Eu}^{3+}$  with increasing pressure.



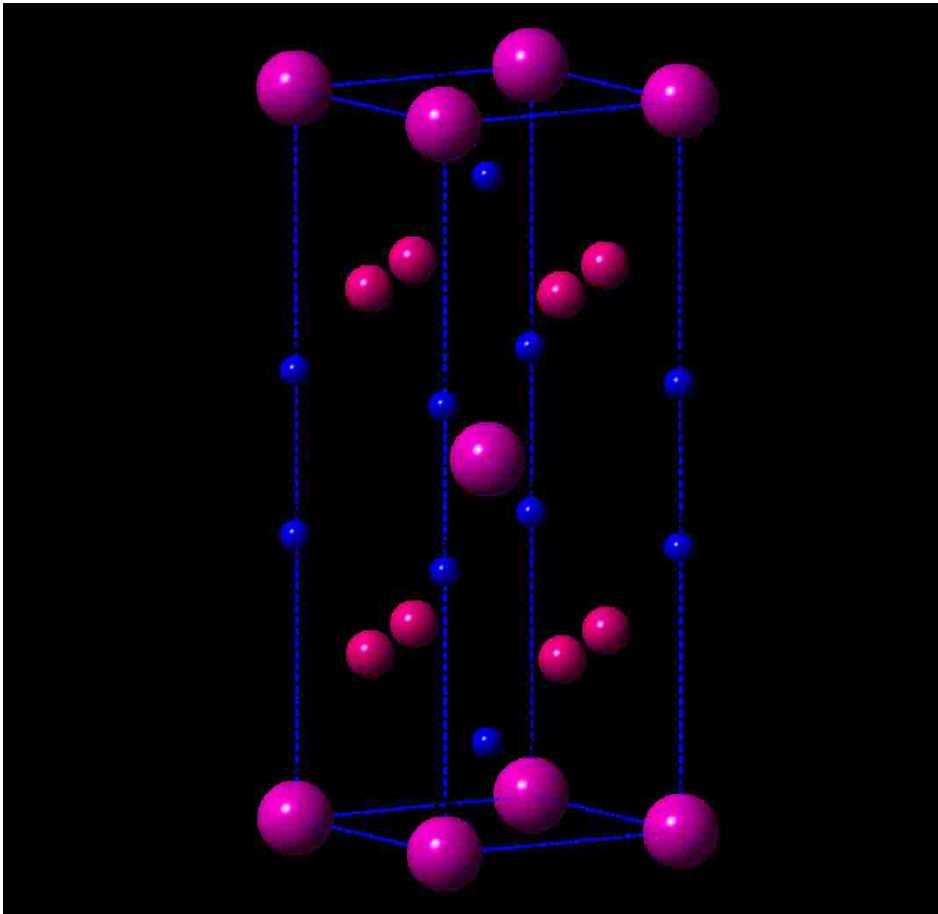


**Figure 36.  $\text{EuMn}_2\text{Si}_2$  crystal structure**

$\text{EuMn}_2\text{Si}_2$  and  $\text{EuCo}_2\text{Si}_2$  crystallize in the  $\text{ThCr}_2\text{Si}_2$  type tetragonal crystal structure (space group 139,  $I4/mmm$ )

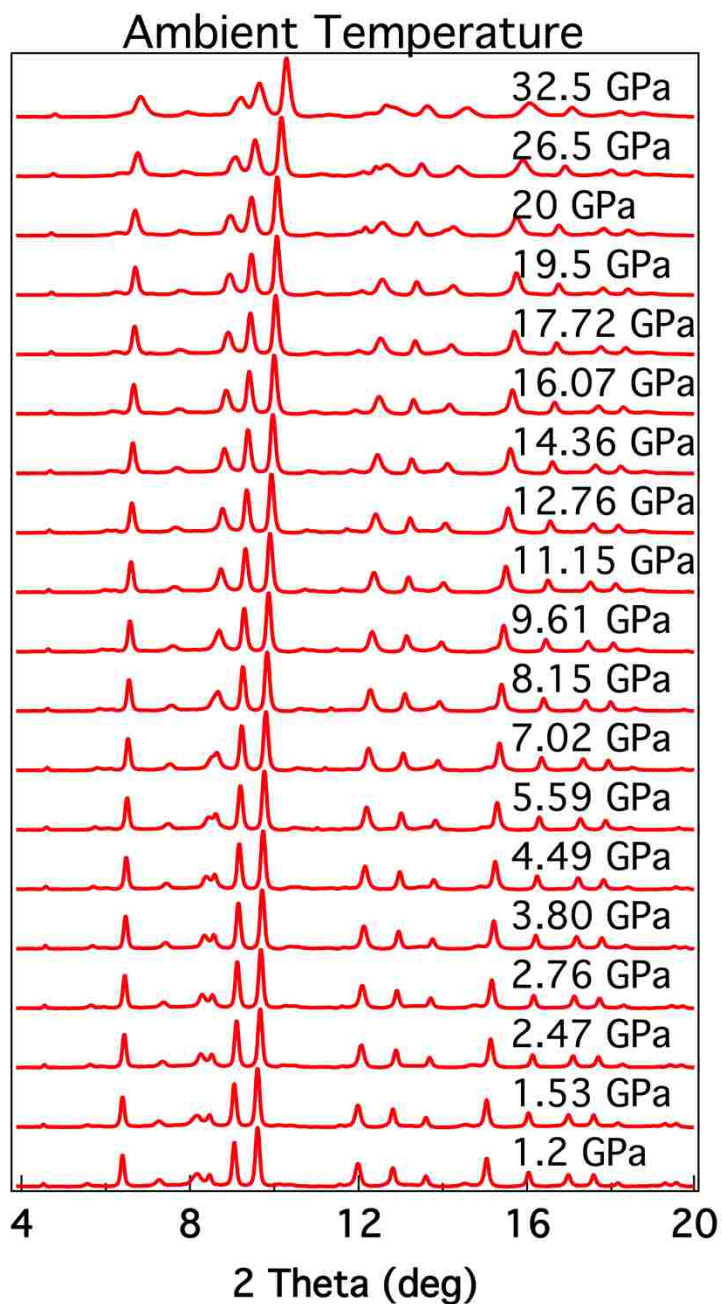


**Figure 37. High pressure X-ray diffraction data for  $\text{EuMn}_2\text{Si}_2$  at ambient temperatures.**

No phase transitions are seen throughout the experiment. The structure remains in the  $\text{ThCr}_2\text{Si}_2$  type tetragonal structure.

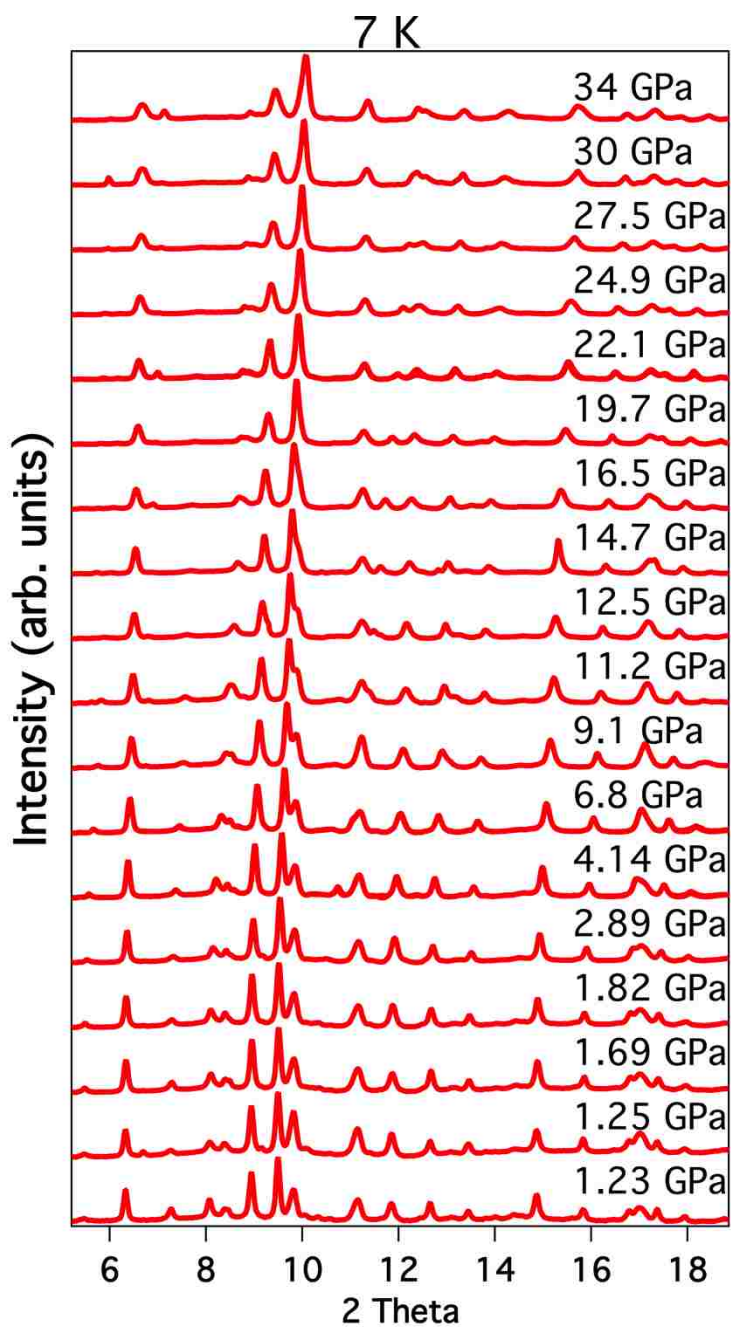


**Figure 38. High pressure X-ray diffraction data for  $\text{EuMn}_2\text{Si}_2$  at 7 Kelvin.**

No phase transitions are seen throughout the experiment. The structure remains in the  $\text{ThCr}_2\text{Si}_2$  type tetragonal structure.

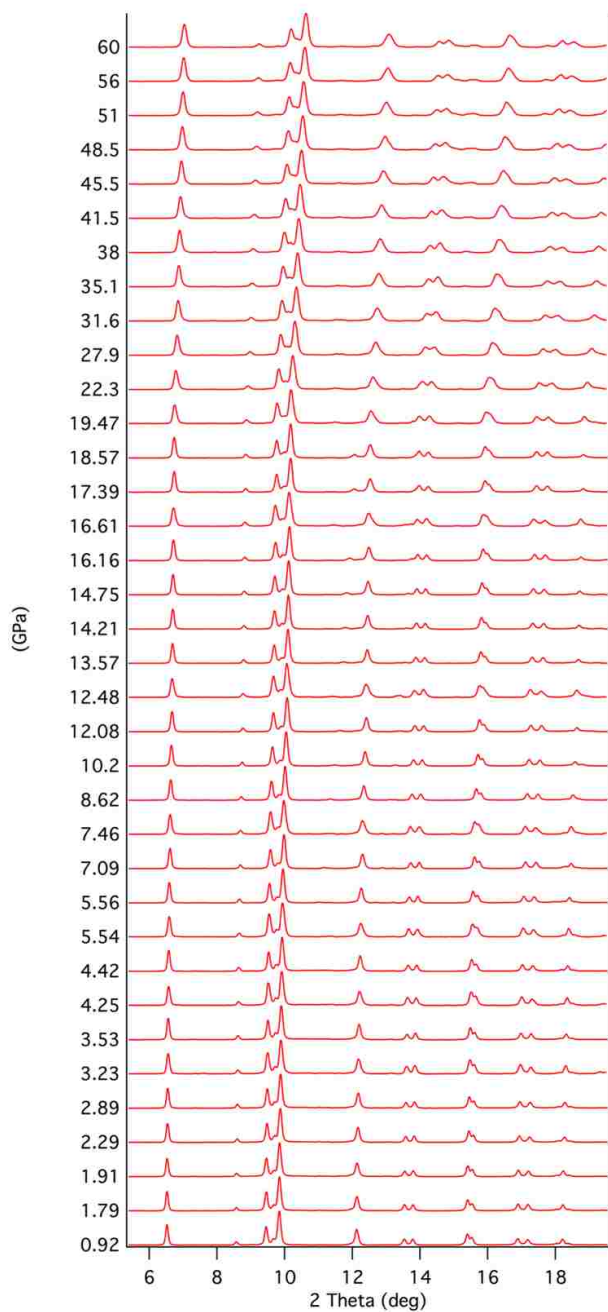


**Figure 39. High pressure X-ray diffraction data for EuCo<sub>2</sub>Si<sub>2</sub> at ambient temperature.**

No phase transitions are seen throughout the experiment. The structure remains in the ThCr<sub>2</sub>Si<sub>2</sub> type tetragonal structure.

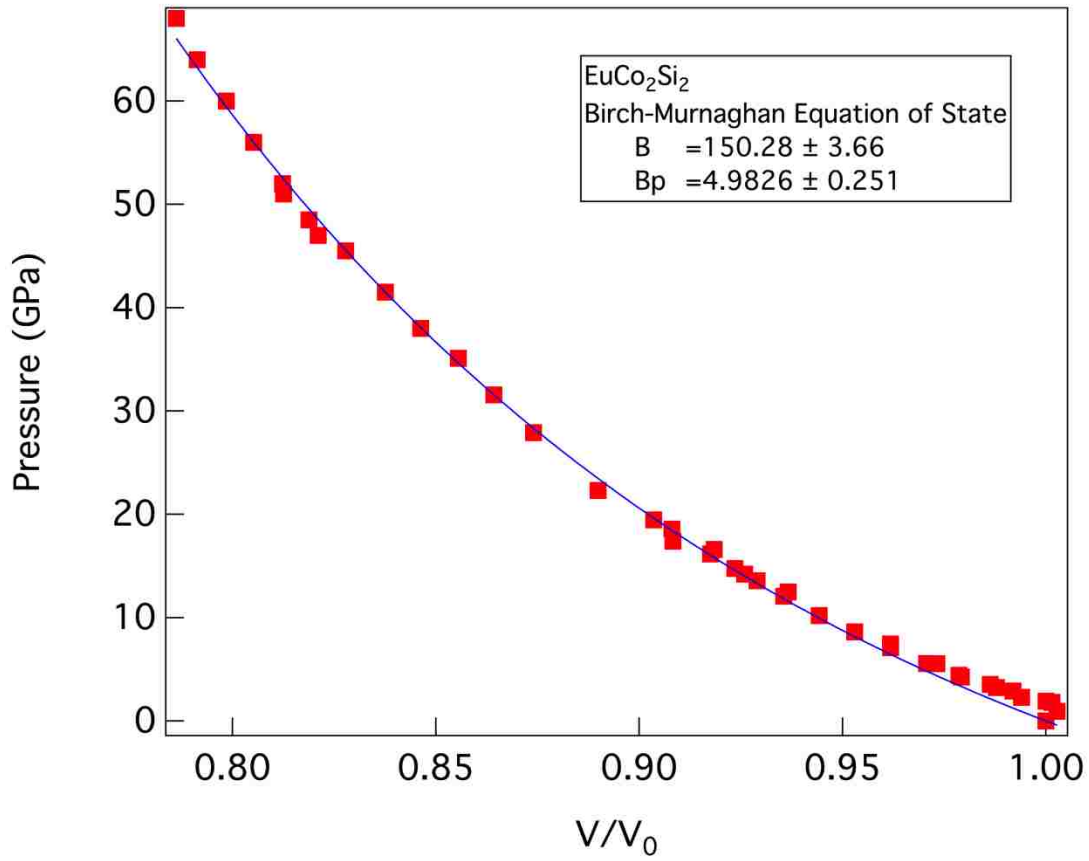


**Figure 40. Equation of state for EuCo<sub>2</sub>Si<sub>2</sub>.**

The Birch-Murnaghan equation of state was fit to the HPXRD data with  $B = 150 \pm 3$  GPa and  $B' = 5.0 \pm 0.3$

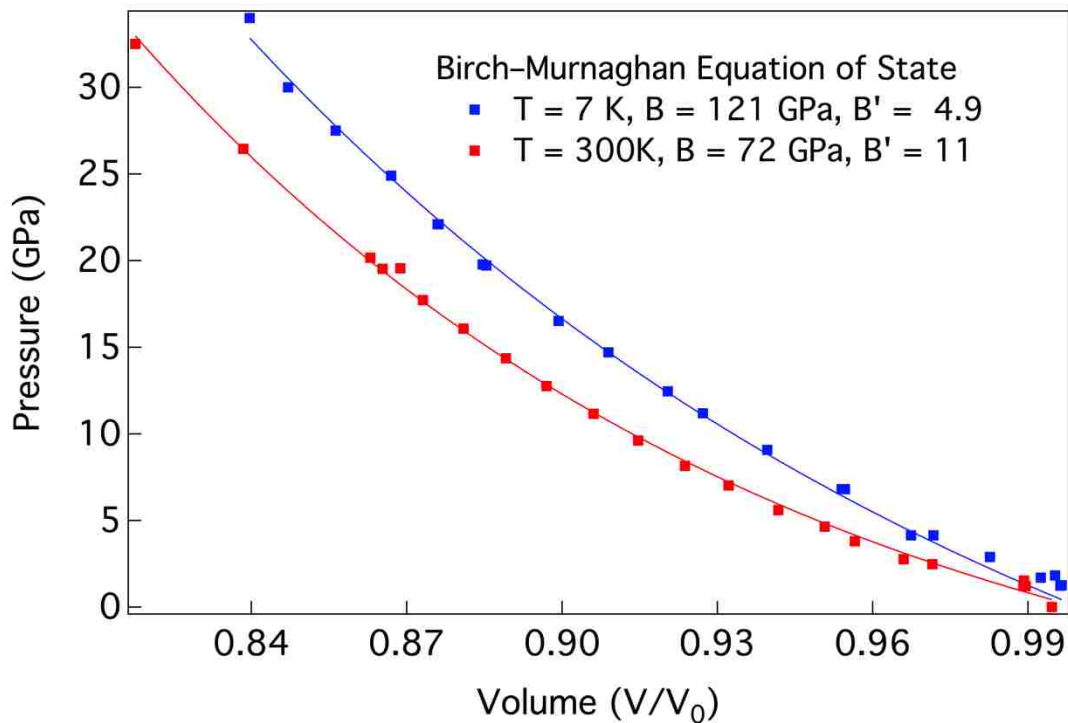


**Figure 41. Equations of state for  $\text{EuMn}_2\text{Si}_2$  at ambient temperature and 7K**

The Birch-Murnaghan equation of state was fit to both the 7K and the ambient temperature data. A large difference is immediately apparent and is almost certainly due to the europium valence already mostly in the 3+ state in the low temperature data at ambient pressure. The volume collapse from 2+ to 3+ is significant.

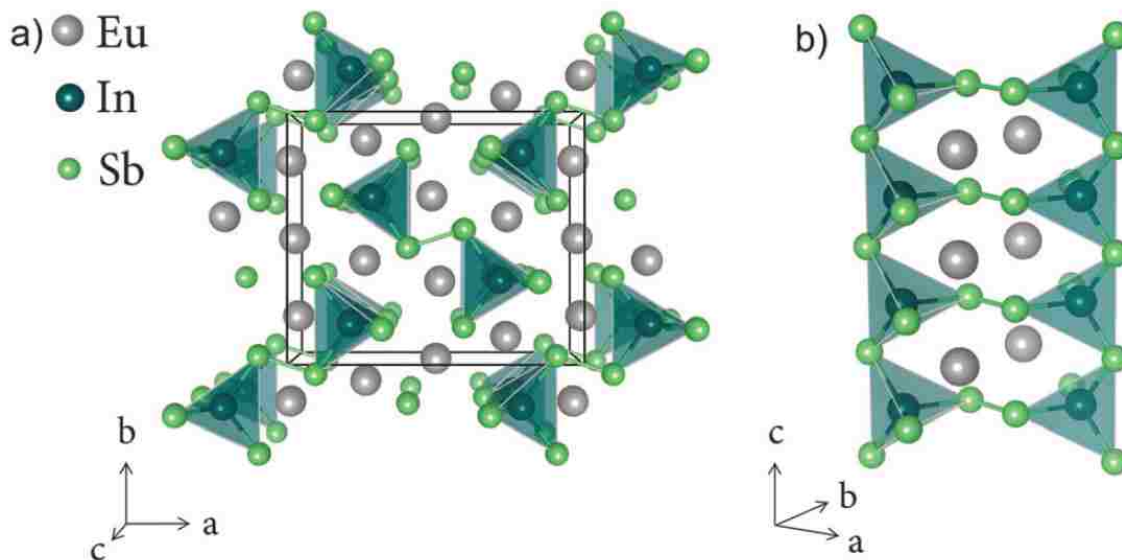


**Figure 42.  $\text{Eu}_5\text{In}_2\text{Sb}_6$  crystal structure**

$\text{Eu}_5\text{In}_2\text{Sb}_6$  has 26 atoms per unit cell. It crystallizes in the orthorhombic (space group 55, Pbam)  $\text{Ca}_5\text{Ga}_2\text{As}_6$  crystal structure and is the only known rare earth analogue to it. There are 10 europium atoms in the unit cell. It is difficult to see, but there effectively only 3 different distinct site locations in the unit cell. There are four europium in one and three in each of the other two. Image borrowed from Chanakian, High temperature thermoelectric properties of Zn-doped  $\text{Eu}_5\text{In}_2\text{Sb}_6$ , J. Mater. Chem. C, 2015,3, 10518-10524. [35]

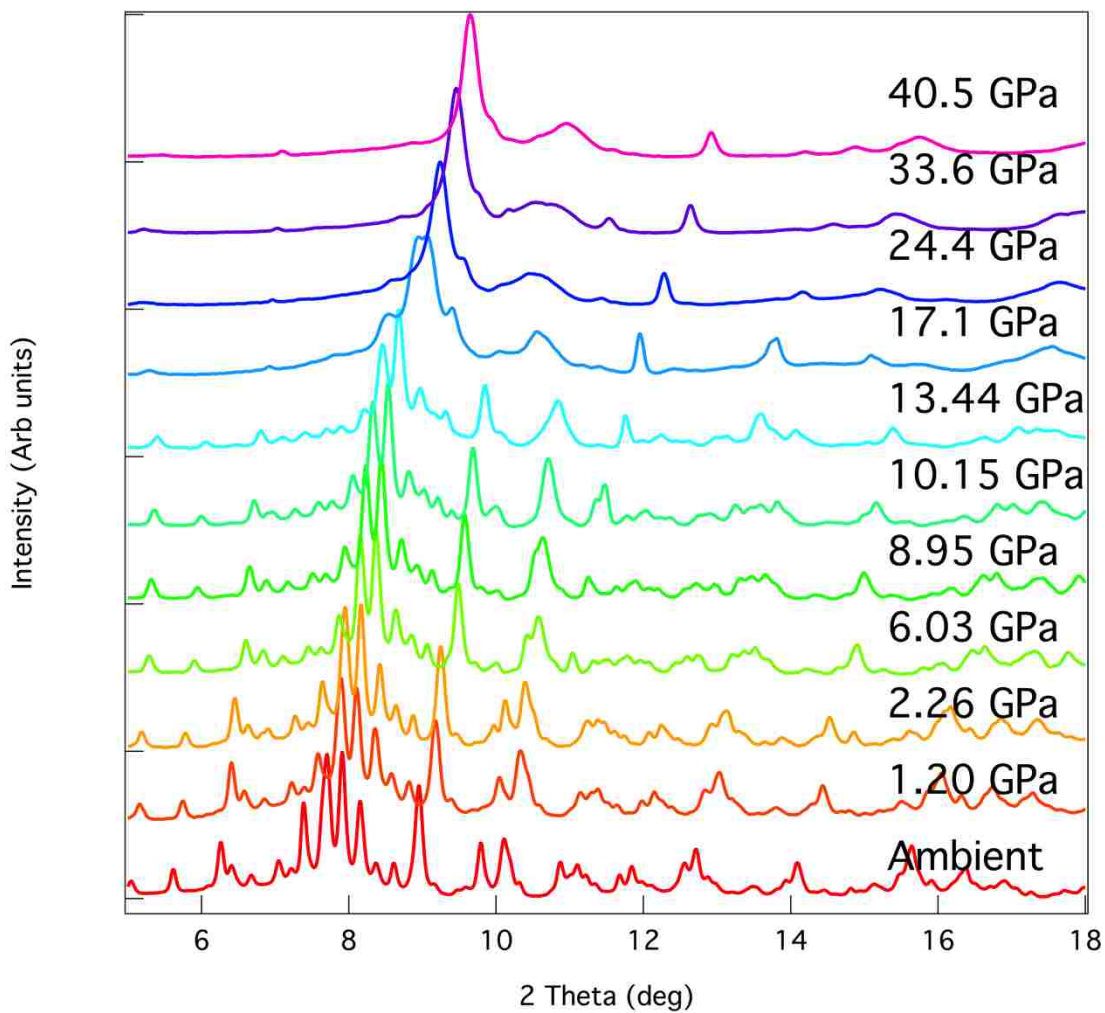


**Figure 43. High pressure XRD for  $\text{Eu}_5\text{In}_2\text{Sb}_6$  at ambient temperatures.**

The sample starts out in the orthorhombic (space group 55,  $Pbam$ )  $\text{Ca}_5\text{Ga}_2\text{As}_6$  crystal structure. It goes through a structural phase transition at about 16 GPa.



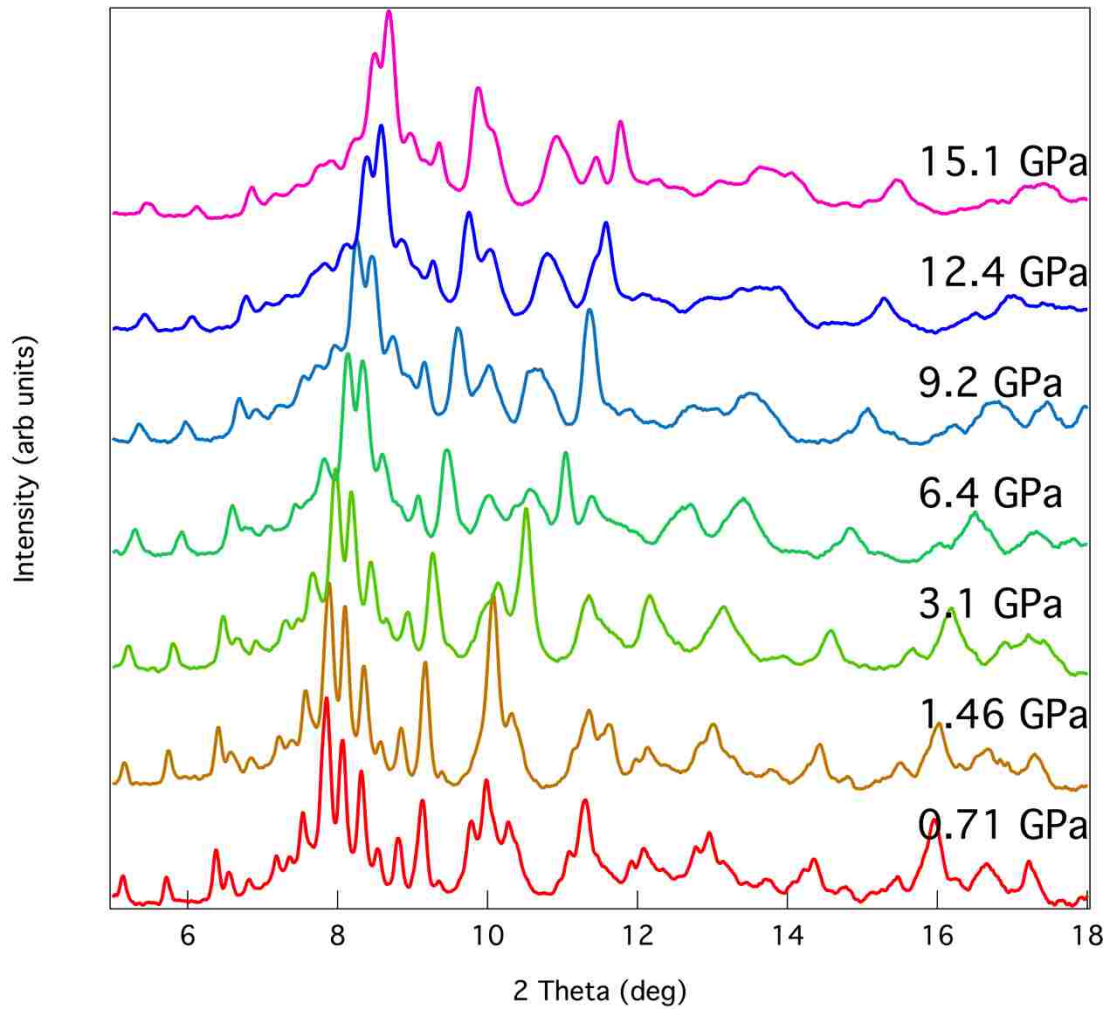


**Figure 44. High pressure X-ray diffraction data for  $\text{Eu}_5\text{In}_2\text{Sb}_6$  at 7 Kelvin.**

The sample starts out in the orthorhombic (space group 55,  $\text{Pbam}$ )  $\text{Ca}_5\text{Ga}_2\text{As}_6$  crystal structure and stays there up to 15.1 GPa.

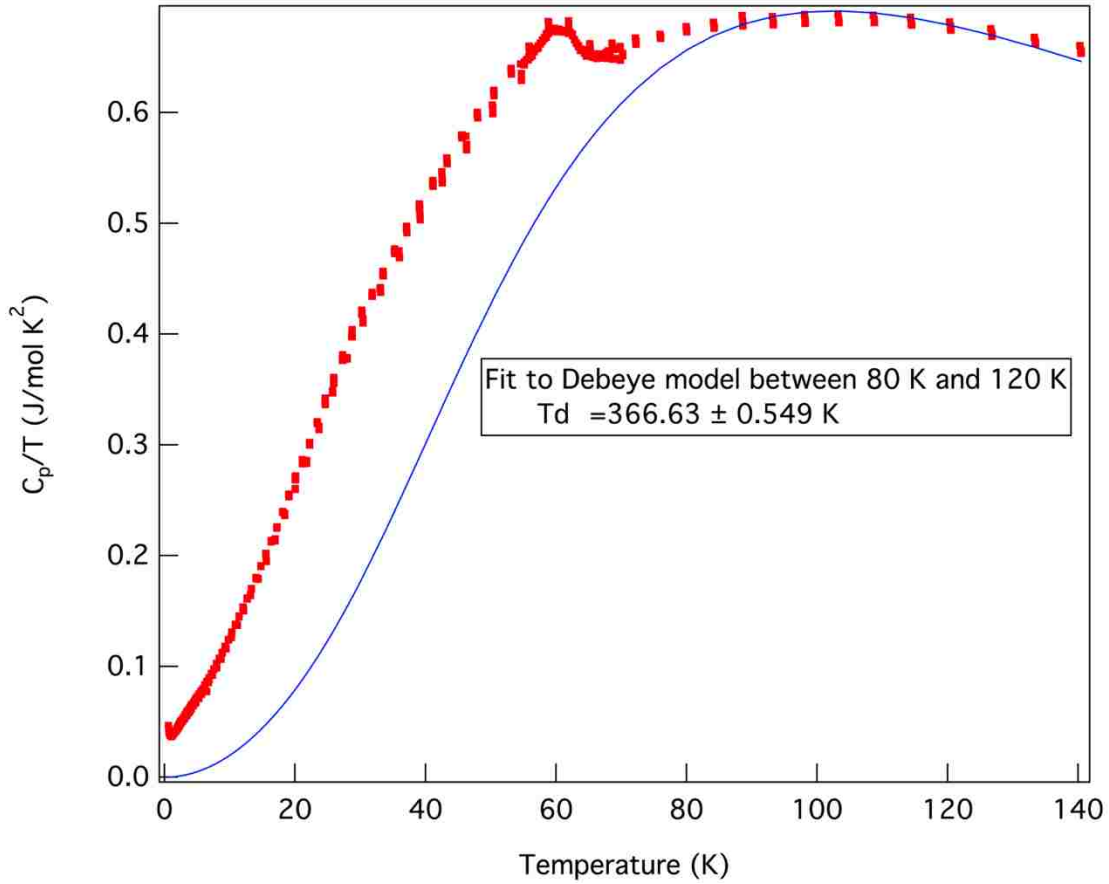


**Figure 45. Specific heat over temperature of  $\text{EuMn}_2\text{Si}_2$**

Specific heat over temperature is shown with a fit to the Debye model. As expected, the Debye model is a poor fit to the lattice contribution from these materials. The temperature shift in valence causes a temperature dependence of the phonon density of states. The Debye model assumes constant phonon modes.

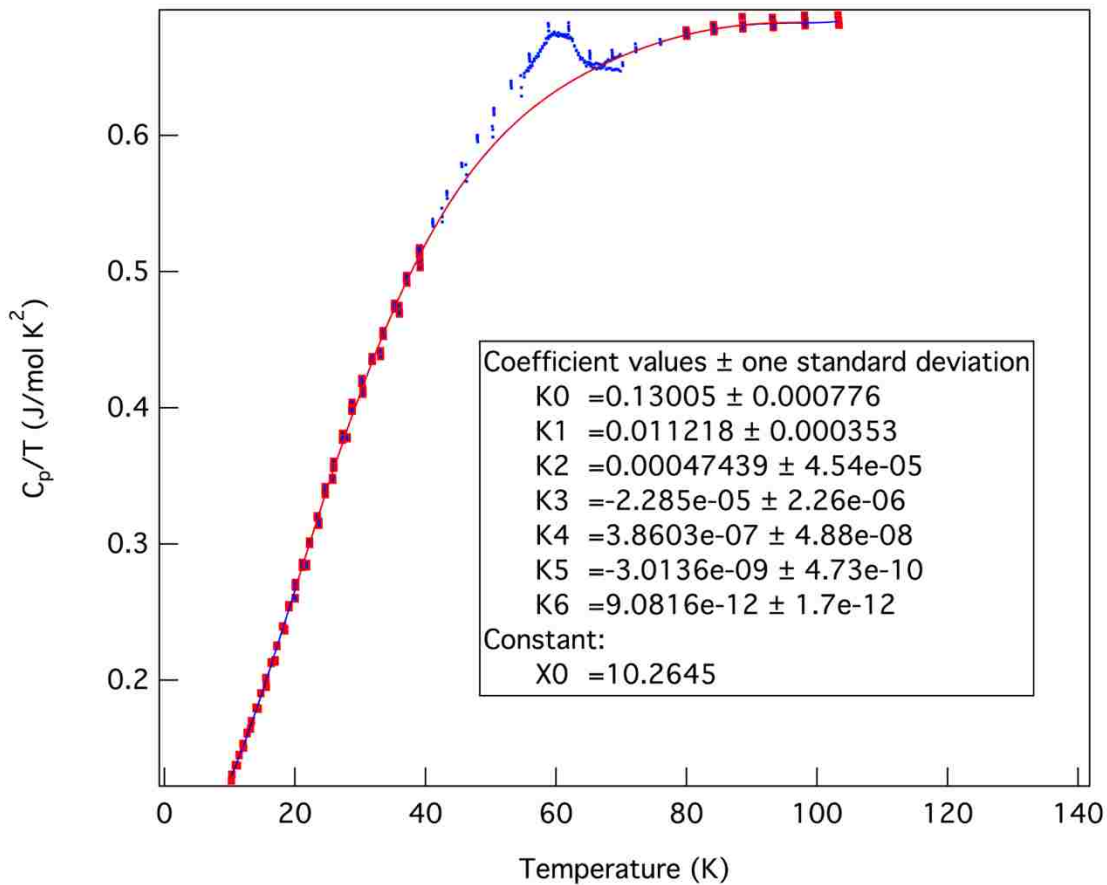


**Figure 46.  $\text{EuMn}_2\text{Si}_2$  specific heat over T fitted to a polynomial approximation**

In order to separate the small transition seen from the lattice, a polynomial was fit to segments surrounding the transition. This fit can then be used to subtract from the data to isolate the non-lattice contribution.

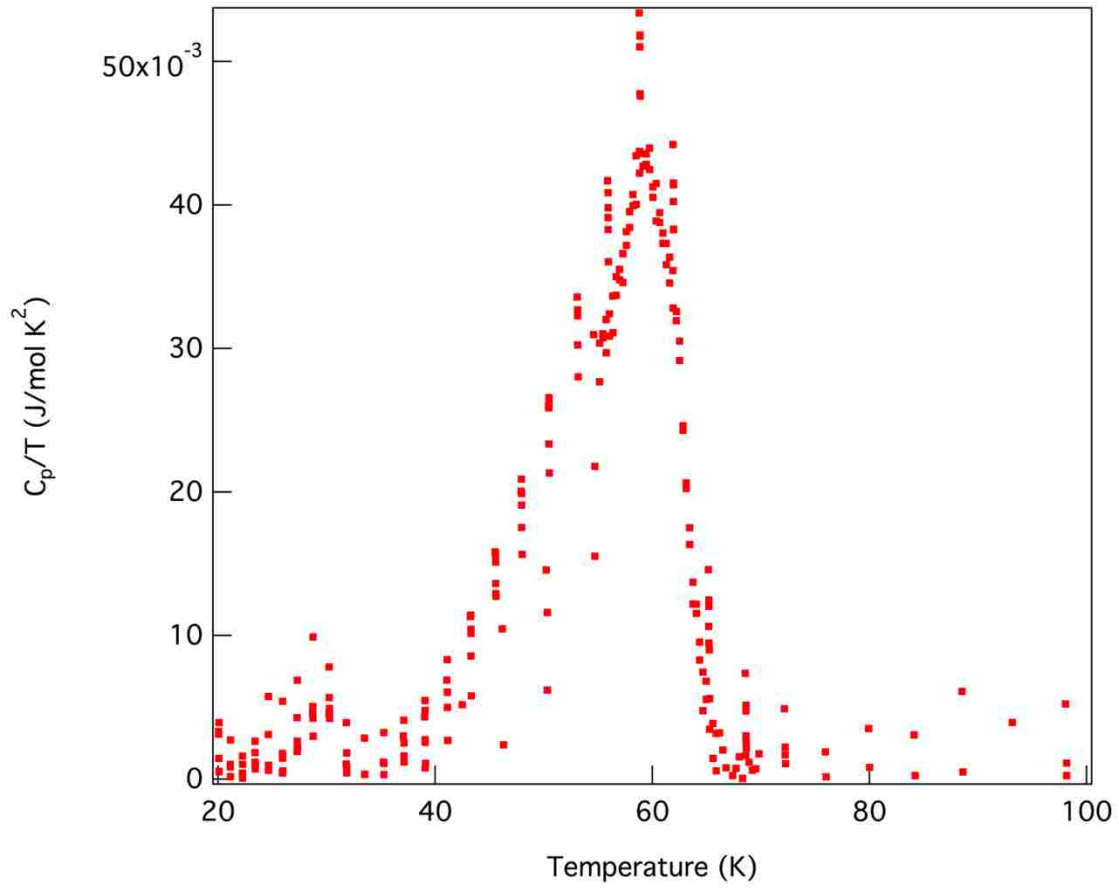


**Figure 47. Approximate non-lattice specific heat  $\text{EuMn}_2\text{Si}_2$**

This is the approximated non-lattice specific heat remaining after subtracting the polynomial fit.

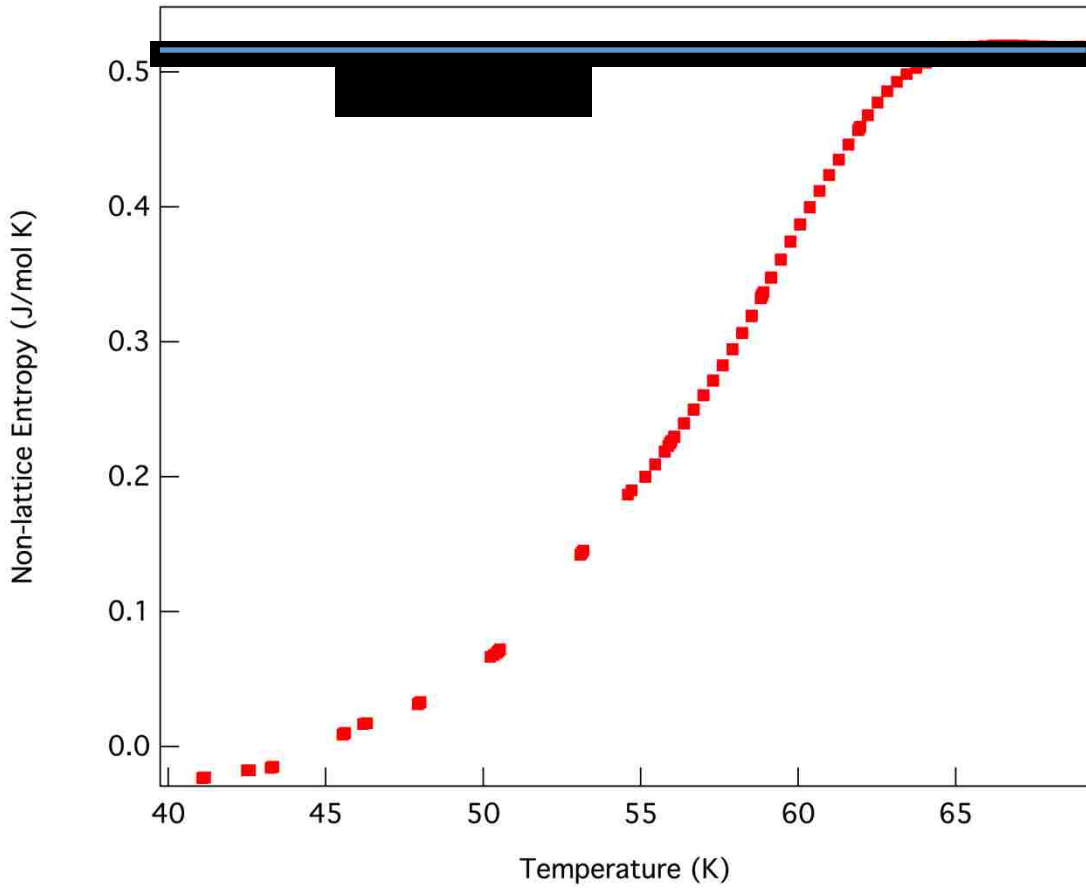


**Figure 48. Approximate non-lattice entropy of  $\text{EuMn}_2\text{Si}_2$**

Integrating the data in figure 47 gives us the entropy. We see here that the entropy is only 3% of what would be expected from fully divalent europium. This implies that the valence is almost completely trivalent. Note that the ordering temperature does not change, only the magnitude of the signal seen. Using a tuning parameter to change the valence from  $\text{Eu}^{2+}$  to  $\text{Eu}^{3+}$  will not result in the same type of quantum critical point seen from the Kondo-RKKY systems.

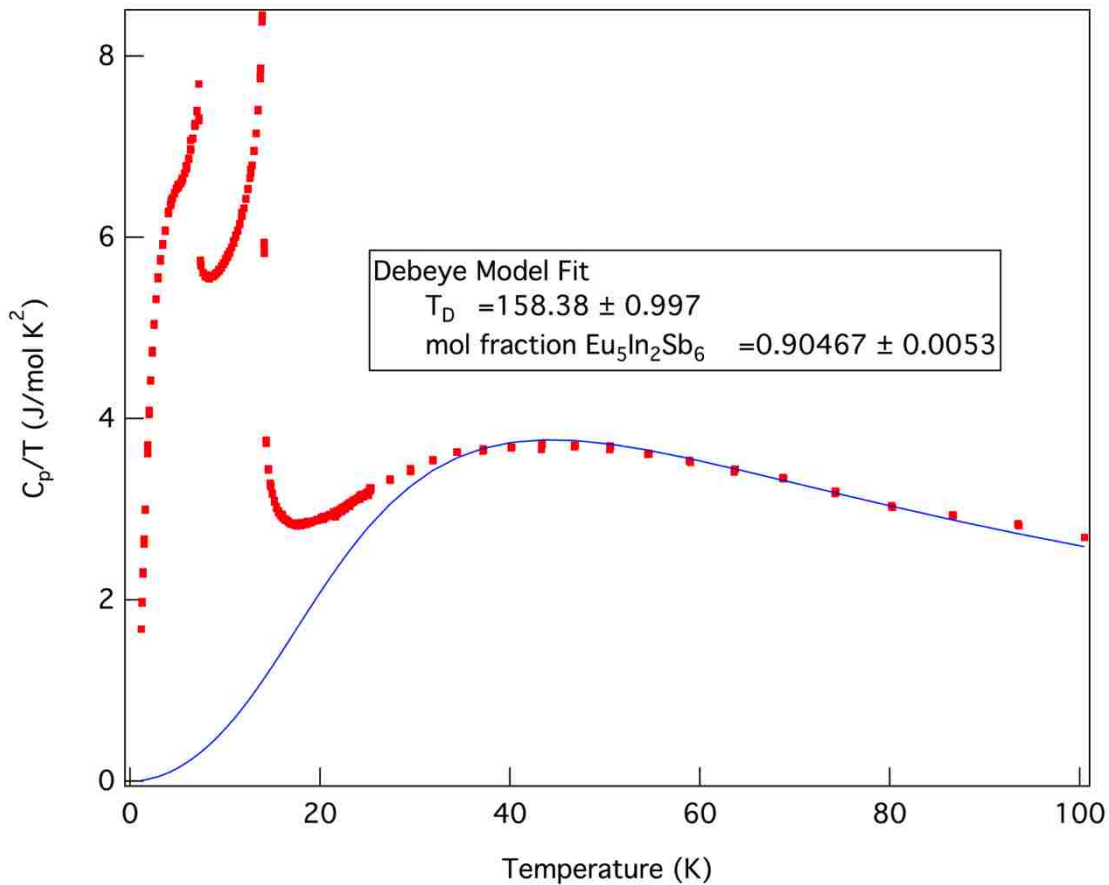


**Figure 49. Specific heat over temperature of  $\text{Eu}_2\text{In}_2\text{Sb}_6$**

Specific heat over temperature is shown with a fit to the Debye model. A reasonable fit of  $T_D = 158\text{K}$  is found. This is expected since the same type of temperature dependence of the europium valence was not seen. The molar fraction was added to the fit to account for significant indium inclusions in the material.

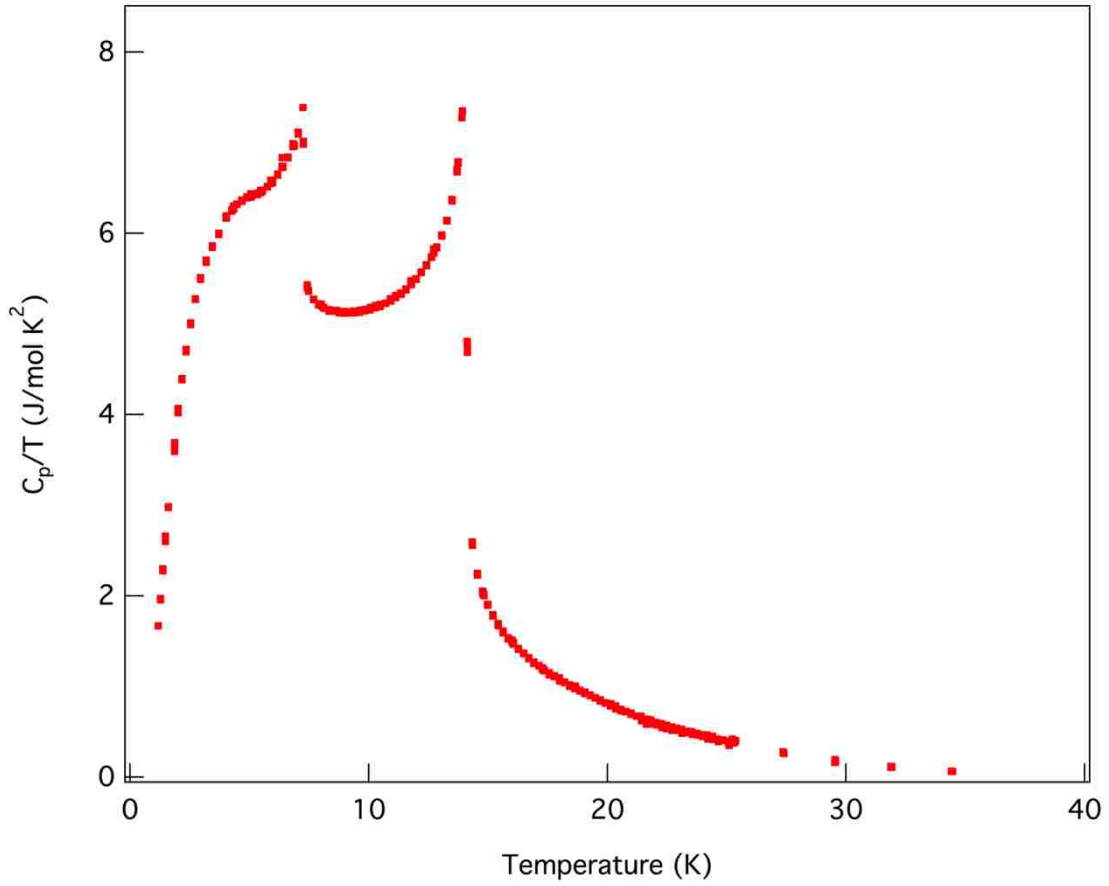


**Figure 50. Non-lattice specific heat over temperature of  $\text{Eu}_2\text{In}_2\text{Sb}_6$**

The non-lattice specific heat over temperature is shown. There appears to be two lambda type transitions and a Shottkey like peak overlapping.

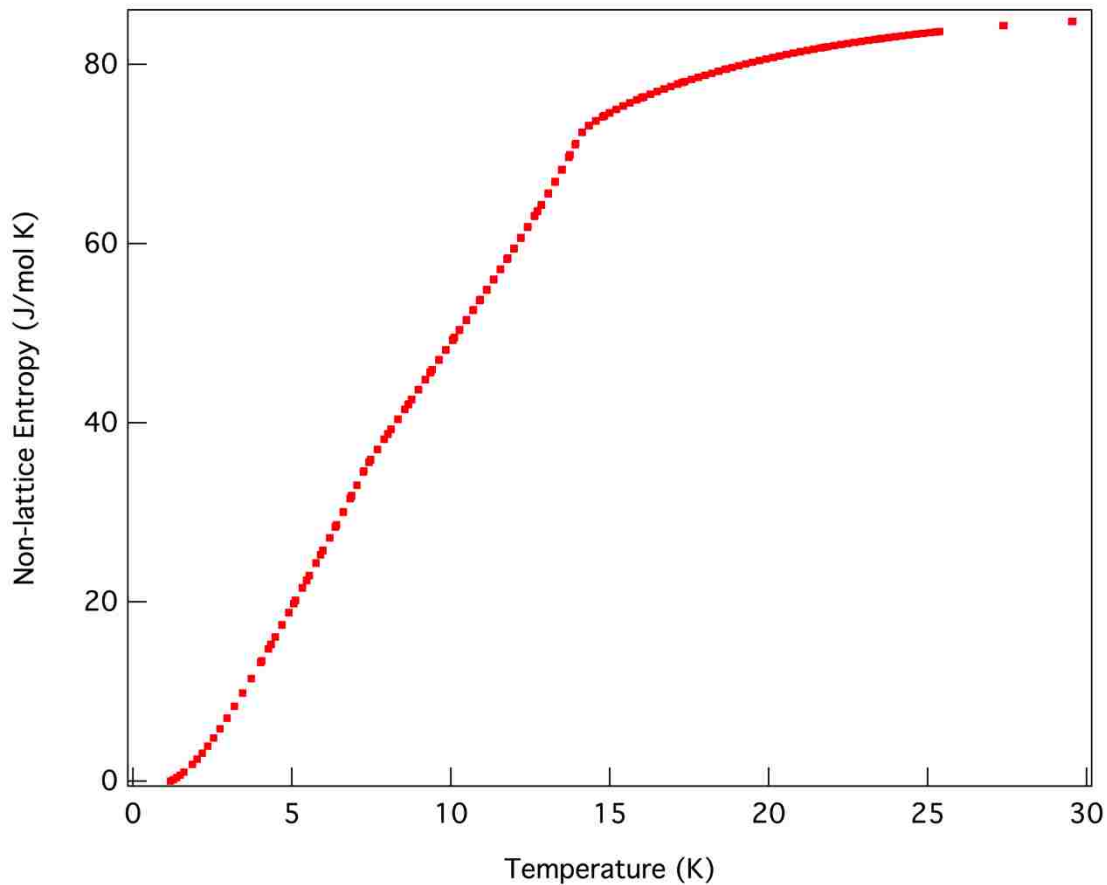


**Figure 51. Non-lattice entropy of  $\text{Eu}_5\text{In}_2\text{Sb}_6$**

The entropy of  $\text{Eu}_5\text{In}_2\text{Sb}_6$  was found by integrating the data shown in figure 50. The total entropy approaches about 86 J/mol K. This is about  $5 R \ln 8$ . This is strange since that would imply that all of the europium is divalent which we know is not true.



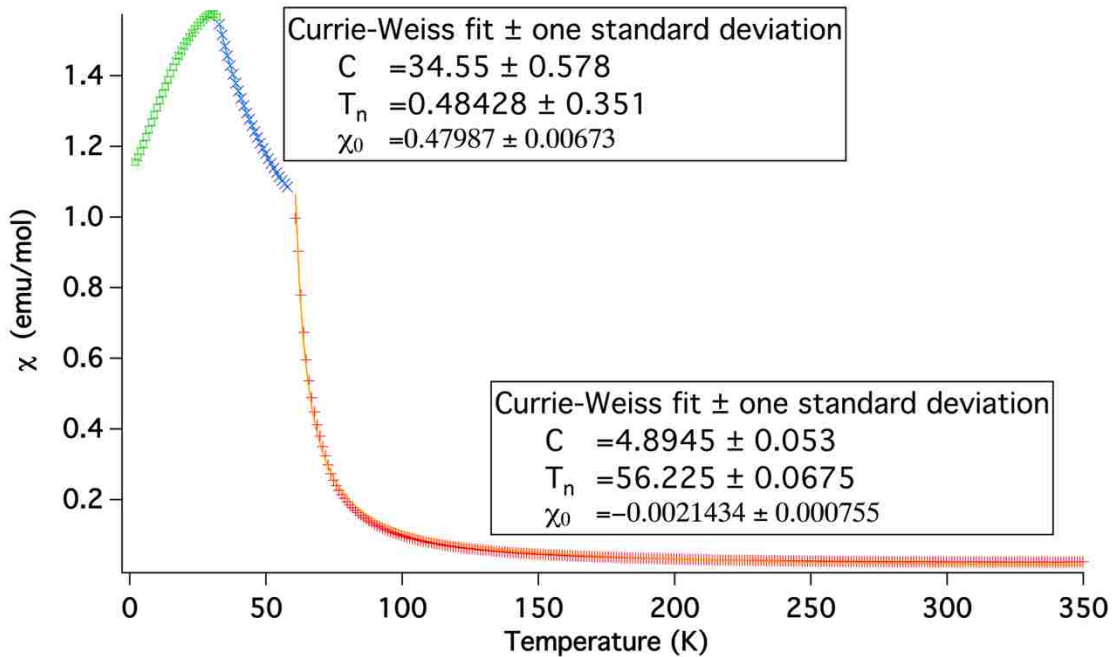


**Figure 52. Fits to magnetic susceptibility of  $\text{EuMn}_2\text{Si}_2$**

A fit to the Currie-Weiss (equation 58) gives  $T_N = 56.23 \pm 0.07$  K and a Currie constant of  $C = 4.89 \pm 0.05$  emu/mol K above about 60 K. Below what is assumed to be an antiferromagnetic transition we see what appears to be a second unknown ordering transition. A strong dependence of the susceptibility (not shown) with excitation field indicates that this could be ferromagnetic. Sample variation below the ordering temperature inhibits any conclusions about this though.

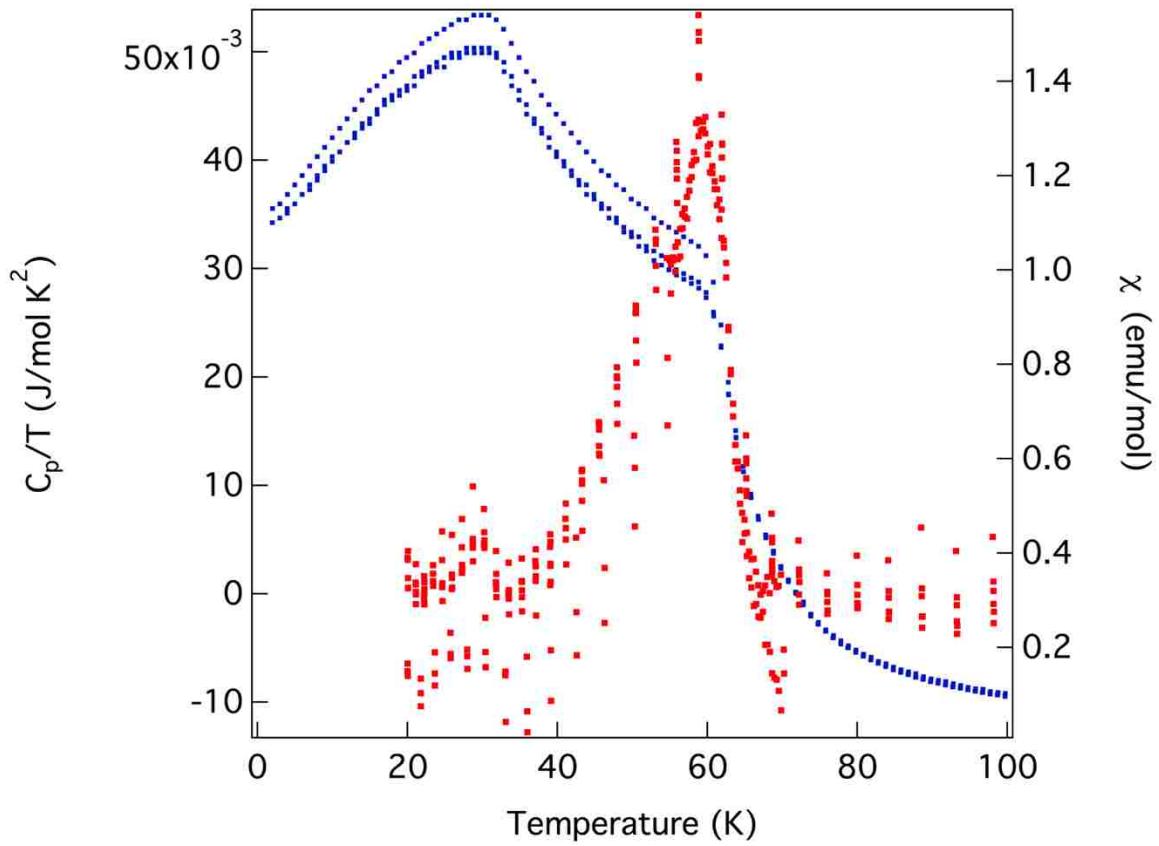


**Figure 53. Comparison of non-lattice specific heat and susceptibility  $\text{EuMn}_2\text{Si}_2$ .**

The peak seen in the heat capacity clearly lines up with the magnetic ordering seen in the susceptibility data. A very small peak amongst the noise in the specific heat can be seen to line up with the peak of the susceptibility as well.

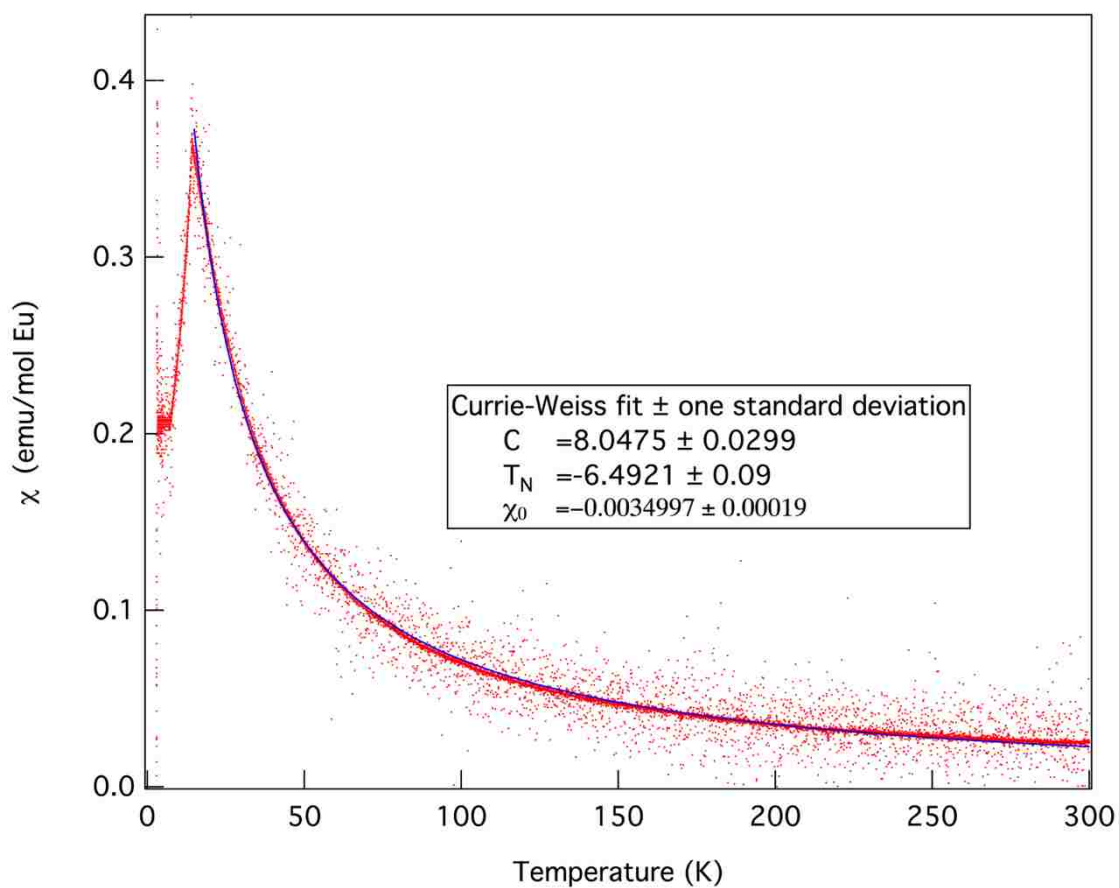


**Figure 54. Magnetic susceptibility of  $\text{Eu}_5\text{In}_2\text{Sb}_6$**

The magnetic susceptibility behaves with Curie-Weiss behavior above a temperature of 14.2 K. A fit to the Curie-Weiss equation is shown.

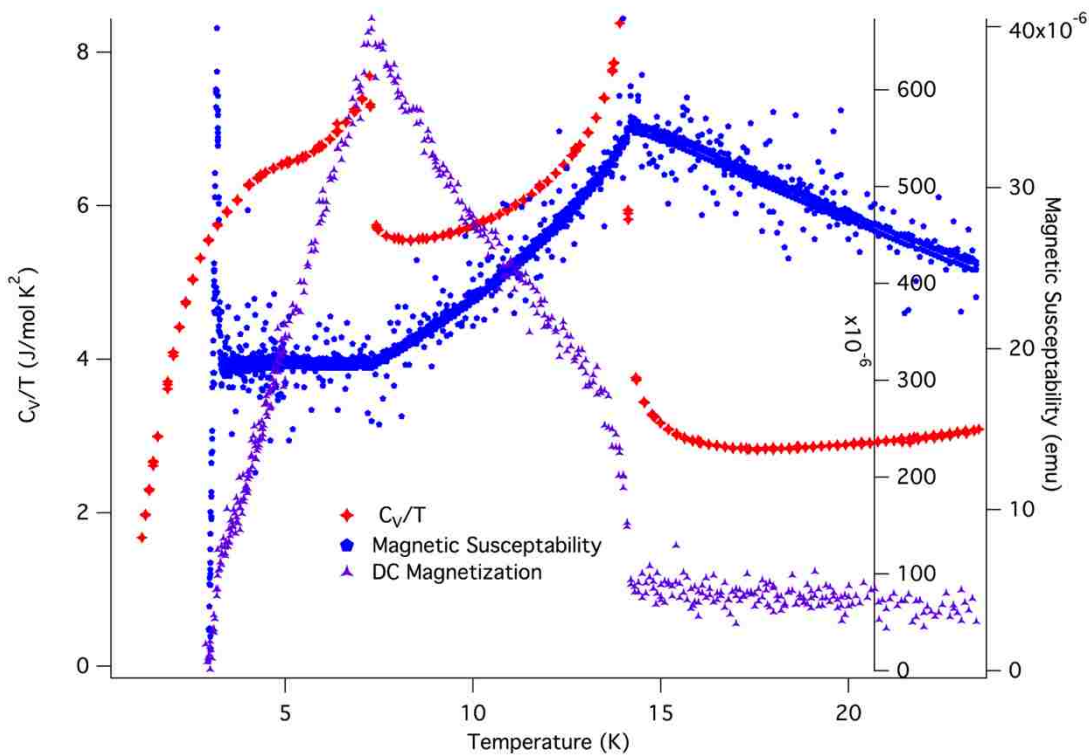


**Figure 55. Comparison of specific heat and susceptibility  $\text{Eu}_5\text{In}_2\text{Sb}_6$**

The sharp peaks seen in the specific heat correspond to a peak in the susceptibility as well as the DC magnetization. The magnetic ordering that is occurring here is unknown but could indicate a low temperature destabilization of the valence as was indicated by the low temperature RXES.

## References

- [1] Stewart, G R. “Non-Fermi-Liquid Behavior in d- and f-Electron Metals.” *Review of Modern Physics*, vol. 73, no. 4, Oct. 2001, pp. 797–855.
- [2] Q. Si and F. Steglich. “Heavy Fermions and Quantum Phase Transitions.” *Science*, vol. 329, no. 5996, 2010, pp. 1161–1166.
- [3] A. T. Holmes, D. Jaccard, and K. Miyake. “Valence Instability and Superconductivity in Heavy Fermion System.” *Journal of the Physical Society of Japan*, vol. 76, no. 5, 2007, p. 51002.
- [4] M. Hofmann, S. J. Campbell, and A. V. J. Edge. “EuMn<sub>2</sub>Ge<sub>2</sub> and EuMn<sub>2</sub>Si<sub>2</sub>: Magnetic structures and valence transitions.” *Physical Review B*, vol. 69, no. 17, May 2004, p. 174432.
- [5] R. S. Kumar *et al.* “Effect of Pressure on Valence and Structural Properties of YbFe<sub>2</sub>Ge<sub>2</sub> Heavy Fermion Compound—A Combined Inelastic X-ray Spectroscopy, X-ray Diffraction, and Theoretical Investigation.” *Inorganic Chemistry*, vol. 54, no. 21, 2015, pp. 10250–10255.
- [6] I. Nowik, I. Felner, and E. R. Bauminger. “Phase Transitions of Europium Valency and Manganese Magnetic Order and Thermal Hysteresis Phenomena in EuMn<sub>2</sub>Si<sub>2</sub>xGe<sub>x</sub>.” *Physical Review B*, vol. 55, no. 5, Feb. 1997, pp. 3033–3041.
- [7] C. Prescher and V. B. Prakapenka. “DIOPTAS: A Program for Reduction of Two-Dimensional X-ray Diffraction Data and Data Exploration.” *High Pressure Research*, vol. 35, no. 3, 2015, pp. 223–230.

- [8] Hunter, B.A. (2000). Rietica - a Visual Rietveld Program. *2nd AINSE Symposium on Neutron Scattering Powder Diffraction and Australian Neutron Beam Users Group Meeting Symposium Handbook*, (p. 24). Australia
- [9] Newsome, R W, and E Y Andrei. "Relaxation Calorimetry Technique for Measuring Low Temperature Specific Heat." *Review of Scientific Instruments*, vol. 75, no. 104, 2004, doi:<https://doi.org/10.1063/1.1633989>.
- [10] M. O. Krause and J. H. Oliver. "Natural Widths of Atomic K and L Levels,  $K\alpha$  X-Ray Lines and Several KLL Auger Lines." *J. Phys. Chem. Red. Data*, Vol. 8, No. 2, 1979.
- [11] Akihiro Mitsuda. "What is origin of the first eu-based heavy fermion?" *JPSJ News and Comments*, 10:14, 2017/04/03 2013.
- [12] Paweł Maślankiewicz, Jacek Szade. "Valence instability of europium in  $\text{EuCo}_2\text{Si}_2$ ." *Journal of Alloys and Compounds*, Volume 423, Issues 1–2, 26 October 2006, Pages 69–73.
- [13] Ōnuki, Yoshichika, et al. "Mass Enhancement of Nearly Trivalent Compound  $\text{EuCo}_2\text{Si}_2$ : Studied by the De Haas-Van Alphen Experiments and Energy Band Calculations." *Journal of Physics: Conference Series*, vol. 592, no. 1, 2015, doi:10.1088/1742-6596/592/1/012049.
- [14] K. S. Nemkovski *et al.* "Europium mixed-valence, long-range magnetic order, and dynamic magnetic response in  $\text{EuCu}_2(\text{Si}_x\text{Ge}_{1-x})_2$ ," *Physical Review B*, vol. 94, no. 19, Nov. 2016, p. 195101.

- [15] Danzenbächer, S, et al. “Hybridization Phenomena in Nearly-Half-Filled f -Shell Electron Systems: Photoemission Study of EuNi<sub>2</sub>P<sub>2</sub>.” *Physical Review Letters*, vol. 102, no. 026403, 14 Jan. 2009, doi:10.1103/PhysRevLett.102.026403.
- [16] N. Kurita *et al.* “Phase diagram of pressure-induced superconductivity in EuFe<sub>2</sub>As<sub>2</sub> probed by high-pressure resistivity up to 3.2 GPa,” *Physical Review B*, vol. 83, no. 21, Jun. 2011, p. 214513.
- [17] D. H. Ryan, R. Rejali, J. M. Cadogan, R. Flacau, and C. D. Boyer. “Europium and Manganese Magnetic Ordering in EuMn<sub>2</sub>Ge<sub>2</sub>.” *Journal of Physics: Condensed Matter*, vol. 28, no. 16, 2016, p. 166003.
- [18] Hrubciak, R, et al. “The Laser Micro-Machining System for Diamond Anvil Cell Experiments and General Precision Machining Applications at the High Pressure Collaborative Access Team.” *Review of Scientific Instruments*, vol. 86, no. 072202, July 2015, doi:10.1063/1.4926889.
- [19] Ashcroft, Neil W, and N David Mermin. *Solid State Physics*. Saunders College Publishing, 1976.
- [20] Diamond Anvil Cells, High Pressure Science and Engineering Center, University of Nevada, Las Vegas, November 2014, <https://hipsecweb.files.wordpress.com/2014/11/mao-type-symmetric-dac-232x166.jpg>.

- [21] Jayaraman, A. “Diamond Anvil Cell and High-Pressure Physical Investigations.” *Reviews of Modern Physics*, vol. 55, no. 1, Jan. 1983, doi:<https://doi.org/10.1103/RevModPhys.55.65>.
- [22] Rivers, M, et al. “The COMPRES/GSECARS Gas-Loading System for Diamond Anvil Cells at the Advanced Photon Source.” *High Pressure Research*, vol. 28, no. 3, 2008, doi:[10.1080/08957950802333593](https://doi.org/10.1080/08957950802333593).
- [23] H.K. Mao, J. Xu, P.M. Bell. “Calibration of the Ruby Pressure Gauge to 800 kbar Under Quasi-Hydrostatic Conditions.” *JGR Solid Earth*, vol. 91, no. B5, April 1986, doi:[10.1029/JB091iB05p04673](https://doi.org/10.1029/JB091iB05p04673)
- [24] A. D. Chijioke, W. J. Nellis, A. Soldatov, and I. F. Silvera. “The ruby pressure standard to 150 GPa.” *Journal of Applied Physics*. vol. 98, no. 114905, 2005, doi:[10.1063/1.2135877](https://doi.org/10.1063/1.2135877)
- [25] V. K. Pecharsky and P. Y. Zavalij, *Fundamentals of Powder Diffraction and Structural Characterization of Materials*, 2nd ed., Springer, 2009
- [26] A. Kotani, “Resonant inelastic X-ray scattering in d and f electron systems.” *European Physical Journal B*. vol. 47, no. 1, pp. 3–27, 2005
- [27] David Goodstein and Andrew R. Chatto, “A dynamic new look at the lambda transition.” *American Journal of Physics*. vol. 71, no. 9, pp. 850-858, doi:[10.1119/1.1586263](https://doi.org/10.1119/1.1586263)
- [28] Sevan Chanakian, Umut Aydemir, Alex Zevalkink, Zachary M. Gibbs, Jean-Pierre Fleurial, Sabah Buxb and G. Jeffrey Snyder. “High temperature thermoelectric



- properties of Zn-doped  $\text{Eu}_5\text{In}_2\text{Sb}_6$ .” *Journal of Materials Chemistry C*, vol. 3 no. 10518, 2015, doi:10.1039/C5TC01645B
- [29] Hans Siethoff, and Karl Ahlborn, “Debye-temperature–elastic-constants relationship for materials with hexagonal and tetragonal symmetry.” *Journal of Applied Physics*. vol. 79, no. 2968, 1996, doi: 10.1063/1.361293
- [30] Kondo, Jun (1964). “Resistance Minimum in Dilute Magnetic Alloys.” *Progress of Theoretical Physics*. vol. 32 no. 1 pp. 37-49, doi: 10.1143/PTP.32.37
- [31] de Haas, W. J., de Boer J., van den Berg, G. J. “The electrical resistance of gold, copper and lead at low temperatures.” *Physica*, vol. 1, no. 7, pp. 1115-1124, 1934, doi: 10.1016/S0031-8914(34)80310-2
- [32] Method J. F. Cochran, C. A. Shiffman, and J. E. “Specific Heat Measurements in 1–10°K Range Using Continuous Warming.” *Review of Scientific Instruments*. vol. 37, no. 4, doi: 10.1063/1.1720226
- [33] Pecharsky V. K. and P. Y. Zavalij, *Fundamentals of Powder Diffraction and Structural Characterization of Materials*, 2nd ed., Springer, 2009
- [34] Luuk J. P. Ament, et al. “Resonant Inelastic X-ray Scattering on Elementary Excitations”, *Review of Modern Physics*. vol. 83, no. 705, June 2011, doi: 10.1103/RevModPhys.83.705
- [35] Sevan Chanakian, et al., “High temperature thermoelectric properties of Zn-doped  $\text{Eu}_5\text{In}_2\text{Sb}_6$ ”, *Journal of Materials Chemistry C*, vol. 3, no. 40, pp. 10518-10524, doi: 10.1039/C5TC01645B

- [36] Nocera, A, et al. “Computing Resonant Inelastic X-Ray Scattering Spectra Using The Density Matrix Renormalization Group Method.” *Scientific Reports*, vol. 8, no. 11080, 23 July 2018, doi:10.1038/s41598-018-29218-8.
- [37] Mackenzie, A P, and S A Grigera. “A Quantum Critical Route to Field-Induced Superconductivity.” *Science*, vol. 309, no. 5739, 26 Aug. 2005, pp. 1330–1331., doi:10.1126/science.1117436.
- [38] Steglich, F, et al. “Magnetism, f-Electron Localization and Superconductivity in 122-Type Heavy-Fermion Metals.” *Journal of Physics: Condensed Matter*, vol. 24, no. 29, 6 July 2012, doi:10.1088/0953-8984/24/29/294201.

## Curriculum Vitae

# Brian E. Light

brianlight42@yahoo.com

---

Accomplished scientific researcher with demonstrated success developing and conducting studies and laboratory experiments with recent focus on condensed matter physics and the exploration of new materials. Skilled in multiple technologies, methodologies, and programming languages. Proven talent for applying complex mathematical models to real-world physical problems. Excellent oral and written communicator able to translate information clearly and concisely.

---

## Education and Credentials

**Ph.D. Physics** – University of Nevada, Las Vegas, Anticipated May 2019

*Dissertation:* Effect of Pressure on Valence and Structural Properties  $\text{EuMn}_2\text{Si}_2$  and  $\text{Eu}_5\text{In}_2\text{Sb}_6$

**Master of Science in Physics** – University of Nevada, Las Vegas

*Thesis:* Ce and Rh site substitution in the antiferromagnetic superconductor  $\text{CeRhIn}_5$ .

**Bachelor of Science in Mathematics** – University of Nevada, Las Vegas

---

## Research Experience

University of Nevada, Las Vegas – Physics Department

**Malcolm F. Nicol Graduate Scholar**, 2014-Present

**Completed rigorous Ph.D. program to earn Post-Doc gaining expertise in multiple scientific and technical areas. Designed, developed, and executed novel research studies alongside colleagues at the UNLV High Pressure Science and Engineering Center.**

- **Conducted experiments at the Advanced Photon Source at Argonne National Laboratory, utilizing High Pressure X-ray diffraction, X-ray resonance emission spectroscopy, and X-ray absorption spectroscopy.**
- **Composed and published multiple studies in scientific journals; currently writing two additional publications based on dissertation findings.**
- **Successfully managed group of undergraduate students in conducting experiments at the Argonne National Laboratory.**
- **Spearheaded multiple projects to build skills and knowledge that either did not incur publishable findings or could not be completed; projects included,**
  - a dynamic compression study at LLNL for the NIF Laser,

- **developing a plastic high-pressure diamond anvil cell for magnetic measurements, and**
- **chemical vapor deposition of wires on diamond for electron transport measurements.**

University of Nevada, Las Vegas – Physics Department

**Teaching and Research Assistant, 1999-2007**

**Educated undergraduate physics students in laboratory environment, creating engaging and relevant lessons to advance their understanding of complex methodologies and concepts. Reviewed and assessed laboratory assignments; provided timely feedback on all submissions.**

- **Developed computational models of condensed matter systems.**
- **Conceptualized and conducted experimental research on superconducting and magnetic materials.**
- **Completed and published Master's thesis titled, Ce and Rh site substitution in the antiferromagnetic superconductor CeRhIn<sub>5</sub>, publication has been cited multiple times by other researchers.**

Desert Research Institute

**Laboratory Technician**

**Led geochemistry and ground water analysis of metal concentrations. Maintained quality laboratory environment for precise measurements.**

## **Additional Experience**

Self-Employed

**Application Developer, 2007-Present**

**Designed, coded, and released multiple mobile applications for IOS devices. Developed software to analyze X-ray resonance emission spectroscopy data. Applied modern machine learning algorithms to solve real world problems. Expertise in multiple programming languages including, Java, C, C++, C#, Objective C, Fortran, and Python. Proven ability to learn and apply new programming languages in short time frames.**

United States Army

**Combat Engineer**

**Served the U.S. military performing construction and demolition tasks with a focus on explosives.**

---

## Publications

**Heat capacity studies of Ce and Rh site substitution in the heavy-fermion antiferromagnet CeRhIn<sub>5</sub>: Shortrange magnetic interactions and non-Fermi-liquid behavior**, B. E. Light, Ravhi S. Kumar, A. L. Cornelius, P.G. Pagliuso, J. L. Sarrao, Physical Review B 01/2004; 69(2)

**Disturbing the spin liquid state in Tb<sub>2</sub>Ti<sub>2</sub>O<sub>7</sub>: Heat capacity measurements on rare earth titanates**, A. L. Cornelius, B. E. Light, Ravhi S. Kumar, M. Eichenfield, T. Dutton, R. Pepin, J. S. Gardner, Physica B Condensed Matter 04/2005; 359:1243-1245

**The crystal structure of CeRhIn<sub>5</sub> under pressure**, R. S. Kumar, H. Kohlmann, B. E. Light, A. L. Cornelius, V. Raghavan, T. W. Darling, J. L. Sarrao, Physica B Condensed Matter 04/2005; 359:407-409.

**Evolution of the Magnetic Ground State in the Electron-Doped Antiferromagnet CaMnO<sub>3</sub>**, Andrew Cornelius, Brian Light, John Neumeier, Physical Review B 07/2003; 68(1).

**Observation of Multiple Spin Relaxation Processes in Dysprosium Titanate**, Andrew Cornelius, Brian Yulga, Brian Light, Jason Gardner, American Physical Society, Annual APS March Meeting 2003, March 3-7, 2003, abstract #G31.005

**Uranium (and Cerium) Compounds At High Pressures and Magnetic Fields**, Andrew L. Cornelius, Ravhi S. Kumar, Brian E. Light, MRS Online Proceeding Library 12/2002; 802

**Anisotropic elastic properties of CeRhIn<sub>5</sub>**, Ravhi S. Kumar, H. Kohlmann, B. E. Light, A. L. Cornelius, V. Raghavan, T. W. Darling, J. L. Sarrao, Physical Review B 09/2002; 69(1)

**Ce-site dilution studies in the antiferromagnetic heavy fermions Ce<sub>m</sub>Rh<sub>n</sub>In<sub>3m+2n</sub> (m= 1, 2; n= 0, 1)**, P. G. Pagliuso, N. O. Moreno, N. J. Curro, J. D. Thompson, M. F. Hundley, J. L. Sarrao, and Z. Fisk, A. D. Christianson, A. H. Lacerda, B. E. Light, A. L. Cornelius, Phys. Rev. B. 01/2002; 66(5)

---

## Conferences

Stewardship Science Academic Programs (SSAP) Symposium, 2017, Poster session presentation: High Pressure Studies of Europium Mixed Valence Compounds

Gordon Research Conference, Research at High Pressure, Emergent Properties at High Material Densities, July 17-22, 2016.

APS March Meeting 2004, Paper presented: "Heat capacity studies of Ce and Rh site substitution in the heavy fermion antiferromagnet CeRhIn<sub>5</sub>: Short-range magnetic interactions and non-Fermi-liquid behavior.", Session A20. DMP: Heavy Fermion Metals & Magnets.

Società Italiana di Fisica, International School of Physics "Enrico Fermi", Varenna, Como Lake, CXLVII - edited by R. J. Hemley, G.L. Chiarotti, M. Bernasconi and L. Ulivi (2001), High Pressure Phenomena.